



N° d'ordre NNT: 2016LYSEI067

# THÈSE de DOCTORAT DE L'UNIVERSITÉ DE LYON

préparée au sein de  
l'Institut National des Sciences Appliquées de Lyon

École Doctorale 162  
Mécanique, Énergétique, Génie civil, Acoustique

Spécialité de doctorat  
MÉCANIQUE – GÉNIE MÉCANIQUE – GÉNIE CIVIL

Soutenue publiquement le Juillet 11, 2016, par:

**Biao LIANG**

---

## **Experimental and numerical study of the bending behaviour of textile reinforcements and thermoplastic prepregs** **(Etude expérimentale et numérique du comportement en flexion des renforts textiles et préimprégnés thermoplastiques)**

---

Devant le jury composé de:

C.RICHARD	Professeur (École polytechnique de l'Université de Tours)	Examineur
C.BINETRUY	Professeur (École Centrale de Nantes)	Rapporteur
C.HOCHARD	Professeur (Université Aix marseille)	Rapporteur
P.BOISSE	Professeur (INSA de Lyon)	Directeur de thèse
J.COLMARS	Maitre de Conférences (INSA de Lyon)	Examineur
N.GODIN	Maitre de Conférences-HDR (INSA de Lyon)	Examineur
O.POLIT	Professeur (l'Université Paris 10-Nanterre)	Examineur

LaMCoS - UMR CNRS 5514 - INSA de Lyon  
20, avenue Albert Einstein, 69621 Villeurbanne Cedex (FRANCE)



## INSA Direction de la Recherche - Écoles Doctorales - Quinquennal 2011-2016

SIGLE	ÉCOLE DOCTORALE	NOM ET COORDONNÉES DU RESPONSABLE
<b>CHIMIE</b>	<b>CHIMIE DE LYON</b> <a href="http://www.edchimie-lyon.fr">http://www.edchimie-lyon.fr</a> Sec. : Renée EL MELHEM Bâtiment Blaise Pascal 3 <sup>ème</sup> étage 04.72.43.80.46 Insa : R. GOURDON <a href="mailto:secretariat@edchimie-lyon.fr">secretariat@edchimie-lyon.fr</a>	<b>M. Jean Marc LANCELIN</b> Université de Lyon - Collège Doctoral Bâtiment ESCPE 43 bd du 11 novembre 1918 69622 VILLEURBANNE Cedex Tél. : 04.72.43.13.95 <a href="mailto:directeur@edchimie-lyon.fr">directeur@edchimie-lyon.fr</a>
<b>E.E.A.</b>	<b>ÉLECTRONIQUE, ÉLECTROTECHNIQUE, AUTOMATIQUE</b> <a href="http://eedea.ec-lyon.fr">http://eedea.ec-lyon.fr</a>  Sec. : M.C. HAVGOUDOUKIAN <a href="mailto:eea@ec-lyon.fr">eea@ec-lyon.fr</a>	<b>M. Gérard SCORLETTI</b> École Centrale de Lyon 36 avenue Guy de Collongue 69134 ECULLY Tél. : 04.72.18 60.97 Fax : 04.78.43.37.17 <a href="mailto:Gerard.scorletti@ec-lyon.fr">Gerard.scorletti@ec-lyon.fr</a>
<b>E2M2</b>	<b>EVOLUTION, ECOSYSTEME, MICROBIOLOGIE, MODÉLISATION</b> <a href="http://e2m2.universite-lyon.fr">http://e2m2.universite-lyon.fr</a> Sec. : Safia AIT CHALAL Bâtiment Atrium- UCB Lyon 1 Tél. : 04.72.44.83.62 Insa : S. REVERCHON <a href="mailto:Safia.ait-chalal@univ-lyon1.fr">Safia.ait-chalal@univ-lyon1.fr</a>	<b>Mme Gudrun BORNETTE</b> CNRS UMR 5023 LEHNA Université Claude Bernard Lyon 1 Bâtiment Forel 43 bd du 11 novembre 1918 69622 VILLEURBANNE Cedex Tél : 06.07.53.89.13 <a href="mailto:e2m2@univ-lyon1.fr">e2m2@univ-lyon1.fr</a>
<b>EDISS</b>	<b>INTERDISCIPLINAIRE SCIENCES-SANTE</b> <a href="http://www.ediss-lyon.fr">http://www.ediss-lyon.fr</a> Sec. : Safia AIT CHALAL Bâtiment Atrium - UCB Lyon 1 Tél. : 04.72.44.83.62 Insa : <a href="mailto:Safia.ait-chalal@univ-lyon1.fr">Safia.ait-chalal@univ-lyon1.fr</a>	<b>Mme Emmanuelle CANET-SOULAS</b>  INSERM U1060, CarMeN lab, Univ. Lyon 1 Bâtiment IMBL 11 avenue Jean Capelle INSA de Lyon 69621 VILLEURBANNE Tél. : 04.72.68.49.09 Fax : 04.72.68.49.16 <a href="mailto:Emmanuelle.canet@univ-lyon1.fr">Emmanuelle.canet@univ-lyon1.fr</a>
<b>INFOMATHS</b>	<b>INFORMATIQUE ET MATHÉMATIQUES</b> <a href="http://infomaths.univ-lyon1.fr">http://infomaths.univ-lyon1.fr</a> Sec. : Renée EL MELHEM Bâtiment Blaise Pascal 3 <sup>ème</sup> étage <a href="mailto:infomaths@univ-lyon1.fr">infomaths@univ-lyon1.fr</a>	<b>Mme Sylvie CALABRETTO</b> LIRIS - INSA de Lyon Bat Blaise Pascal 7 avenue Jean Capelle 69622 VILLEURBANNE Cedex Tél. : 04.72.43.80.46 Fax : 04.72.43.16.87 <a href="mailto:Sylvie.calabretto@insa-lyon.fr">Sylvie.calabretto@insa-lyon.fr</a>
<b>Matériaux</b>	<b>MATÉRIAUX DE LYON</b> <a href="http://ed34.universite-lyon.fr">http://ed34.universite-lyon.fr</a>  Sec. : M. LABOUNE PM : 71.70 Fax : 87.12 Bâtiment Saint-Exupéry <a href="mailto:Ed.materiaux@insa-lyon.fr">Ed.materiaux@insa-lyon.fr</a>	<b>M. Jean-Yves BUFFIERE</b> INSA de Lyon MATEIS Bâtiment Saint-Exupéry 7 avenue Jean Capelle 69621 VILLEURBANNE Cedex Tél. : 04.72.43.71.70 Fax : 04.72.43.85.28 <a href="mailto:Ed.materiaux@insa-lyon.fr">Ed.materiaux@insa-lyon.fr</a>
<b>MEGA</b>	<b>MÉCANIQUE, ÉNERGÉTIQUE, GÉNIE CIVIL, ACOUSTIQUE</b> <a href="http://edmega.universite-lyon.fr/">http://edmega.universite-lyon.fr/</a>  Sec. : M. LABOUNE PM : 71.70 Fax : 87.12 Bâtiment Saint-Exupéry <a href="mailto:mega@insa-lyon.fr">mega@insa-lyon.fr</a>	<b>M. Philippe BOISSE</b> INSA de Lyon Laboratoire LAMCOS Bâtiment Jacquard 25 bis avenue Jean Capelle 69621 VILLEURBANNE Cedex Tél. : 04.72.43.71.70 Fax : 04.72.43.72.37 <a href="mailto:Philippe.boisse@insa-lyon.fr">Philippe.boisse@insa-lyon.fr</a>
<b>ScSo</b>	<b>ScSo*</b> <a href="http://recherche.univ-lyon2.fr/scso/">http://recherche.univ-lyon2.fr/scso/</a> Sec. : Viviane POLSINELLI Sec. : Brigitte DUBOIS Insa : J.Y. TOUSSAINT <a href="mailto:viviane.polsinelli@univ-lyon2.fr">viviane.polsinelli@univ-lyon2.fr</a>	<b>Mme Isabelle VON BUELTZINGLOEWEN</b> Université Lyon 2 86 rue Pasteur 69365 LYON Cedex 07 Tél. : 04.78.77.23.86 Fax : 04.37.28.04.48 <a href="mailto:isavonb@gmail.com">isavonb@gmail.com</a>



# Acknowledgment

I wish to appreciate a number of people for their help during my PhD thesis.

First and foremost, I would like to express my appreciation to Professor Philippe Boisse for his supervision and guidance through this work. His consistent concern, creative advice and countless encouragement have helped me to complete my PhD thesis. His enthusiasm and meticulousness on scientific research impress me deeply, which sets me a model to follow in my future research work.

I'm also grateful to Dr.Nahiene Hamila, Dr.Julien Colmars and Professor Emmanuelle Vidal-Salle for their assistance and advice on my PhD work.

Appreciation should be also going to Philippe Chaudet, Mickael Peillon and Paul Valverde for their help on my experiment.

I also thank the support and help from my colleagues, they are Eduardo Guzman, Naim Naouar, Ismael Azehaf, Dawei Wang, Hu Xiong, Jie Wang. I have spent joyful days with them.

I acknowledge the financial support provided by China Scholarship Council (CSC) in pursuing my PhD study in France. I'm indebted to my research laboratory, LaMCoS, INSA-Lyon, for its financial and technical support.

Finally, I'm very grateful to my loving parents for their patience and support throughout my life. Last but not the least, I heartily appreciate my wife, Sasa Gao, for her encouragement, help and accompaniment in Lyon (France) during the period my PhD studies.



# Abstract

This thesis is devoted to study the bending behaviour of textile reinforcements and thermoplastic preregs by the experimental and numerical methods. At the high temperature, since the resin is melted, fibers would have the slippage between them, resulting the bending stiffness of thermoplastic prepreg is not directly related to its in-plane tensile modulus as the conventional continuous materials. Consequently, it's necessary to measure its value by the experimental method. A bending stiffness test approach was proposed for thermoplastic prepreg at elevated temperature. It was operated in an environmental chamber and a CCD camera was used to acquire the bending deflection shape. Bending moment and curvature were calculated along the midline of bending deflection shape. The slope of moment-curvature curve is the bending stiffness. With this method, bending tests were conducted for several types of thermoplastic preregs at a range of high temperatures. In order to simulate the bending deformation of thick fibrous materials, a specific shell element was developed. This element was made of continuous fiber segments. Both the tensile and bending stiffnesses of fibers were taken into account. Local curve was constructed for any fiber segment and its two neighbors, which was used to characterize the tensile and bending deformations of fiber segment. Several bending simulation tests were performed with this specific shell element and were compared with the experimental results to show its efficiency. The results show this specific shell element has good capability to simulate the bending deformation of thick fibrous materials.

**KEYWORDS:** Bending stiffness, Thermoplastic preregs, Fibrous materials, Specific shell element



# Résumé

Cette thèse est consacrée à l'étude du comportement en flexion des renforts textiles et préimprégnés thermoplastiques par des méthodes expérimentales et numériques. Pour préimprégnés thermoplastique, aux températures élevées, la résine est à l'état fondu, et un glissement entre les fibres est possible. En conséquence la rigidité de flexion n'est pas directement liée au module de rigidité de traction dans le plan comme c'est le cas pour les matériaux continus classiques. Par conséquent, il est nécessaire de mesurer sa valeur par l'expérience. Un procédé de test de la rigidité à la flexion a été proposée pour les préimprégnés thermoplastiques. Il est réalisé dans une enceinte thermique. Une caméra CCD a été utilisé pour acquérir le profil de la déformation de flexion à différentes températures élevées en particulier au voisinage du point de fusion. Le moment de flexion et la courbure ont été calculés le long de la ligne médiane de la profil de la déformation. La pente de la courbe moment-courbure est la rigidité à la flexion. Avec cette méthode, des essais de flexion ont été effectués sur plusieurs préimprégnés thermoplastiques. Pour simuler la déformation de flexion de matériaux fibreux épais, un élément de coque spécifique a été développée. Cet élément est constitué de segments de fibres continues. La rigidité de traction et de flexion de la fibre ont été prise en compte de dans l'énergie de déformation de cet élément. La forme curviligne locale a été construit pour tout segment de fibre a partir des voisins. Il a été utilisé pour caractériser les déformations de traction et de flexion pour le segment de la fibre. Plusieurs tests de simulation de flexion ont été réalisées avec cet élément de coque spécifique et ont été comparés avec les résultats expérimentaux pour montrer l'efficacité de cet élément proposé. Les résultats montrent cet élément de coque spécifique a une bonne capacité à simuler la déformation en flexion des matériaux fibreux épais.

**MOTS CLÉS :** Rigidité à la flexion, Préimprégnés thermoplastiques, Matières fibreuses, Élément de coque spécifique



# Contents

<b>Contents</b>	<b>i</b>
<b>List of Figures</b>	<b>v</b>
<b>List of Tables</b>	<b>xi</b>
<b>Notations</b>	<b>xiii</b>
<b>1 Introduction</b>	<b>1</b>
1.1 Introduction to composite materials . . . . .	2
1.1.1 Definition of composite materials . . . . .	2
1.1.2 Types of reinforcement . . . . .	2
1.1.3 Types of matrix material . . . . .	4
1.1.4 Prepregs (Pre-impregnated composites) . . . . .	5
1.2 Processing techniques for polymer composites . . . . .	6
1.2.1 Resin transfer molding (RTM) . . . . .	6
1.2.2 Thermo-forming process . . . . .	7
1.2.3 Autoclave forming process . . . . .	8
1.3 Deformation mechanisms of polymer composites . . . . .	8
1.3.1 Microscopic scale: Fibers . . . . .	8
1.3.2 Mesoscopic scale: Yarns . . . . .	9
1.3.3 Macroscopic scale: Reinforcements or composites . . . . .	12
1.4 Simulation models in the forming . . . . .	19
1.4.1 Simulation models at microscopic scale . . . . .	19
1.4.2 Simulation models at the mesoscopic scale . . . . .	20
1.4.3 Simulation models at the macroscopic scale . . . . .	22
1.5 Motivation and objectives . . . . .	24
1.6 Thesis summary . . . . .	25
<b>2 Bending stiffness characterization for thermoplastic prepregs at the manufacturing temperature</b>	<b>27</b>
2.1 Introduction . . . . .	27
2.2 Review of the related works . . . . .	28
2.2.1 Bending stiffness characterization for dry reinforcement . . . . .	28

2.2.2	Bending stiffness characterization for thermoplastic composites . . . . .	32
2.3	An improved cantilever bending test approach for thermoplastic prepregs . . . . .	34
2.3.1	Basic ideas of the bending test approach . . . . .	34
2.3.2	Set-up description and general test procedure . . . . .	35
2.3.3	Temperature analysis in the bending test . . . . .	37
2.3.4	Image processing of the bending deflection shape . . . . .	38
2.3.5	Curvature calculation . . . . .	39
2.3.6	Bending moment computation . . . . .	46
2.4	Bending experimental test campaign . . . . .	47
2.4.1	Interested materials . . . . .	47
2.4.2	Bending test for PPS-Carbon satin prepreg and PEEK-Carbon satin prepreg . . . . .	47
2.4.3	Bending test for PA66-Glass satin prepreg . . . . .	52
2.5	Forming simulations: influence of the bending stiffness on wrinkling de- velopment . . . . .	54
2.5.1	Wrinkling in compression . . . . .	55
2.5.2	Influence of bending stiffness on wrinkling during forming . . . . .	55
2.6	Conclusions of chapter 2 . . . . .	60
<b>3</b>	<b>Specific plane shell element for simulating the bending deformation of thick fibrous materials</b> . . . . .	<b>61</b>
3.1	Introduction . . . . .	61
3.2	The highlight of the specific bending behaviour of thick fibrous materials . . . . .	62
3.3	Specific plane shell element made of continuous fiber segments . . . . .	64
3.3.1	Assumptions . . . . .	64
3.3.2	Internal virtual work . . . . .	65
3.3.3	Explicit dynamic approach . . . . .	65
3.3.4	Geometry and kinematics of the specific plane shell element . . . . .	66
3.3.5	Strategies to characterize tensile and bending deformations for fiber segments in the element . . . . .	69
3.3.6	Construction of the local curve . . . . .	70
3.3.7	Elementary tensile nodal loads . . . . .	75
3.3.8	Fiber segment tension force update . . . . .	78
3.3.9	Elementary bending nodal loads . . . . .	78
3.3.10	Fiber segment bending moment update . . . . .	78
3.3.11	Imposition of the boundary conditions . . . . .	79
3.4	Numerical simulation and experimental comparisons . . . . .	80
3.4.1	Simulations of book bending tests . . . . .	80
3.4.2	Simulations of laminated reinforcement bending tests . . . . .	90
3.4.3	Three points bending tests for layer to layer angle interlock . . . . .	97
3.4.4	Simulation of L-flange bending deformation . . . . .	102
3.4.5	The emphasis of the Mindlin shell element is unable to simulate the bending deformation of thick fibrous materials . . . . .	103

3.5 Conclusions of chapter 3 . . . . .	106
<b>Conclusions and perspectives</b>	<b>109</b>
<b>Appendices</b>	<b>111</b>
<b>A</b>	<b>113</b>
A.1 The calculation of system stiffness matrix for the uniform quartic B-spline curve . . . . .	113
A.2 Incremental relative angle calculation . . . . .	114
<b>Bibliography</b>	<b>117</b>



# List of Figures

1.1	Application of composites in the Boeing 787 aircraft [BOE 13]. . . . .	1
1.2	Images of different internal structures for reinforcement [SHE 07]. . . . .	3
1.3	Internal weaving structure forms of angle interlock. . . . .	4
1.4	Definition of Prepregs and their types. . . . .	5
1.5	RTM process. (a) Dry reinforcement forming. (b) Resin injection. (c) Final composite part. . . . .	6
1.6	Schematic of thermo-stamping process [HTT 14]. . . . .	7
1.7	Configuration of autoclave. . . . .	8
1.8	Three research scales for textile composites. . . . .	9
1.9	Yarn's tensile behaviour [DUM 03]. . . . .	9
1.10	Yarn's tensile behaviour test device proposed by C.Florimond. (a) Configuration of test device. (b) Yarn's tensile test result [FLO 13]. . . . .	10
1.11	Fibers distribution in a yarn: (a) Unloaded. (b) Subjected to biaxial tension [BAD 08]. . . . .	11
1.12	Two modes of yarn's shearing: (a) Transverse shearing. (b) Longitudinal shearing [FLO 13]. . . . .	12
1.13	Picture frame test device and the shape of sample. . . . .	13
1.14	In-plane shear curve of the plain weave fabric [ZOU 06]. . . . .	13
1.15	Schematic of an idealized sample used in BE tests. (a) Un-sheared sample. (b) Sheared sample [WAN 08]. . . . .	15
1.16	Bias extension test set-up for thermoplastic composites [WAN 14]. . . . .	15
1.17	Schematic of biaxial phenomenon [BOI 04]. . . . .	16
1.18	Biaxial tension test device and measuring results [BUE 01]. . . . .	17
1.19	Transverse compaction device and measuring results [NGU 13]. . . . .	17
1.20	Longitudinal and transverse shearing test device for interlock reinforcement [CHA 12]. . . . .	18
1.21	Forming of an unbalanced textile reinforcement. (a) Tensile stiffness only. (b) Tensile + in-plane shearing stiffnesses. (c) Tensile + in-plane shearing + Bending stiffnesses. (d) Experimental forming [BOI 11] . . . . .	19
1.22	Simulation of in-plane shear at the scale of fibers [DUR 10]. . . . .	20
1.23	Two types of RUCs for a plain weave fabric and their deformed shapes [BAD 07b]. . . . .	21
1.24	Validation of no sliding assumption between yarns in the forming [BOI 95].	22

1.25	A representative cell of the meso-mechanical model for NCF [CRE 06]. . . . .	23
1.26	Schematic of semi-discrete elements and their forming simulations. (a) Shell element [HAM 08]. (b) Solid element [LUY 09]. . . . .	24
2.1	Schematic representation of Peirce’s cantilever bending test [PEI 30]. . . . .	29
2.2	Standard cantilever bending tester. (a) Schematics. (b) Configuration [STA 04]. . . . .	30
2.3	KES-FB2 bending tester [DEB 10]. (a) The Configuration. (b) Bending test results. . . . .	31
2.4	The configuration of flexometer proposed by De Bilbao [DEB 10]. . . . .	31
2.5	Bending test results of reinforcement with different bending length from flexmeter [DEB 10]. . . . .	32
2.6	Vertical cantilever test for the evaluation of bending stiffness [SOT 11]. . . . .	33
2.7	Buckling bending test proposed by Wang [WAN 08]. (a) Layout of a buckling test. (b) Photograph of experimental setup. . . . .	33
2.8	Experimental bending test device proposed by U. Sachs [SAC 14]. . . . .	34
2.9	Schemataic of proposed bending test approach. . . . .	35
2.10	Bending test set-up configuration. . . . .	36
2.11	Optical measure and lighting with two LED lamps. . . . .	36
2.12	(a) Positions of thermocouples. (b) Temperature measurements at different instructions. . . . .	37
2.13	The effect of thresholding. (a) Original image. (b) Too high thresholding. (c) Proper thresholding. (d) Too low thresholding. . . . .	38
2.14	Shape smoothing. (a) Noisy shape. (b) Noisy shape after shape smoothing. . . . .	39
2.15	Skeletonization and midline plotting. . . . .	40
2.16	Example of uniform quartic B-spline curve. . . . .	41
2.17	Influence of the number of segments of uniform quartic B-spline on the fitting error and fairness of curvature plot. Left: sample data points and fitting curve. Right: curvature plot. (a) 1 segment: fitting error 5.71. (b) 3 segments: fitting error 3.31. (c) 4 segments: fitting error 3.1. . . . .	45
2.18	Moment calculating. (a) Stress resultants ( $N$ , $T$ , $M$ ) on the cross-section for the curvilinear abscissa $s$ . (b) Frenet’s coordinates. . . . .	46
2.19	Interested materials. (a) PEEK-Carbon satin prepreg. (b) PPS-Carbon satin prepreg. (c) PA66-Glass satin prepreg. . . . .	47
2.20	The definition of mean deflection curve. . . . .	48
2.21	PEEK-Carbon satin prepreg bending experiment (orientation $0^\circ$ ). (a) Deflections for different temperatures. (b) Bending moment versus curvature. . . . .	49
2.22	PEEK-Carbon satin prepreg bending experiment (orientation $90^\circ$ ). (a) Deflections for different temperatures. (b) Bending moment versus curvature. . . . .	49
2.23	PPS-Carbon satin prepreg bending experiment (orientation $0^\circ$ ). Deflections for different temperatures. (b) Bending moment versus curvature. . . . .	50

2.24	PPS-Carbon satin prepreg bending experiment (orientation $90^\circ$ ). Deflections for different temperatures. (b) Bending moment versus curvature. . . . .	51
2.25	Reproducibility tests of PEEK-Carbon satin prepreg: (a) $200^\circ\text{C}$ . (b) $380^\circ\text{C}$ . . . . .	51
2.26	Bending tests with an added lump mass. . . . .	52
2.27	Bending tests with an added mass: moment versus curvature and comparison with tests without mass. (a) PEEK prepreg. (b) PPS prepreg. . . . .	53
2.28	Delamination was observed in the bending test for PA66-Glass satin prepreg. . . . .	53
2.29	Bending profile for PA66-Glass prepreg. (a) At room temperature ( $25^\circ\text{C}$ ). (b) At high temperature ( $260^\circ\text{C}$ ). . . . .	54
2.30	PA66-glass prepreg bending (orientation $0^\circ$ ). (a) Deflections for different temperatures. (b) Bending moment versus curvature. . . . .	55
2.31	Simulation of compression of a prepreg strip. (a) $150^\circ\text{C}$ . (b) $320^\circ\text{C}$ . (c) $380^\circ\text{C}$ . . . . .	56
2.32	Forming with a cylindrical punch. . . . .	56
2.33	Forming simulations with prepreg properties at $275^\circ\text{C}$ and $300^\circ\text{C}$ . . . . .	57
2.34	Simulation of a thermoforming at $275^\circ\text{C}$ . (a) With in-plane shear and bending stiffnesses. (b) With in-plane shear stiffness and without bending stiffness. . . . .	58
2.35	Sensitivity analysis on the bending stiffness. . . . .	59
3.1	Bending deformation experiments. (a) Book made of 130 pages. (b) Layer to layer angle interlock [MAT 15]. (c) Laminated reinforcement (all plies are orientated in the same direction). . . . .	63
3.2	Specific plane shell element made of continuous fiber segments. . . . .	64
3.3	Geometry of the specific plane shell element at time $t$ . . . . .	67
3.4	Definition of local orthogonal frame $(i\mathbf{V}_1^k, i\mathbf{V}_2^k, i\mathbf{V}_3^k)$ . . . . .	68
3.5	Thickness modelling for the junction node of two elements. . . . .	69
3.6	The local curve represented by the endpoints of three adjacent fiber segments. . . . .	70
3.7	The interpolation of the local curve represented by the endpoints of three adjacent fiber segments. . . . .	71
3.8	Cantilever bending: (a) Book. (b) Single page paper. (c) Comparison of their midlines. . . . .	81
3.9	Moment-curvature curve of single page paper. . . . .	82
3.10	Geometry parameters of book cantilever bending. . . . .	82
3.11	Book cantilever bending deformation: (a) Experiment. (b) Simulation (with midline plotting). . . . .	83
3.12	Comparison of the midline between experiment and simulation for book cantilever bending . . . . .	83
3.13	Comparison of experiment and simulation for book cantilever bending: the angle between the material director and the horizontal direction . . . . .	84
3.14	Comparison of the thickness in the material director direction between experiment and simulation for book cantilever bending . . . . .	84

## List of Figures

---

3.15	Boundary conditions of book bending test 2. . . . .	85
3.16	Deformation shape of book bending test 2: (a) Experiment. (b) Simulation (with midline plotting). . . . .	85
3.17	Comparison of the midline between experiment and simulation for book bending test 2. . . . .	86
3.18	Comparison of experiment and simulation for book bending test 2: the angle between the material director and the horizontal direction . . . . .	86
3.19	Comparison of the thickness in the material director direction between experiment and simulation for book bending test 2. . . . .	87
3.20	Boundary conditions of book bending test 3. . . . .	87
3.21	Deformation shape of book bending test 3: (a) Experiment. (b) Simulation (with midline plotting). . . . .	88
3.22	Comparison of the midline between experiment and simulation for book bending test 3. . . . .	89
3.23	Comparison of experiment and simulation for book bending test 3: the angle between the material director and the horizontal direction. . . . .	89
3.24	Comparison of the thickness in the material director vector direction between experiment and simulation for book bending test 3. . . . .	90
3.25	Cantilever bending test: (a) Laminated reinforcement. (b) Single ply. . . . .	91
3.26	Moment-curvature curve of laminated reinforcement's single ply . . . . .	92
3.27	Moment-curvature curve from bending test of laminated reinforcement and from summation of individual ply. . . . .	92
3.28	Deformation shape of laminated reinforcement in the cantilever bendings: (a) Test A: bending length 118 mm. Left: experiment, Right: simulation. (b) Test B: bending length 132 mm. Left: experiment, Right: simulation. . . . .	93
3.29	Comparison of the midline between experiment and simulation for laminated reinforcement in the cantilever bending. . . . .	94
3.30	Boundary conditions of complex bending test 1 for laminated reinforcement. . . . .	95
3.31	Deformation shape of laminated reinforcement in complex bending test 1: (a) Experiment. (b) Simulation (with midline plotting). . . . .	95
3.32	Comparison of the midline between experiment and simulation for laminated reinforcement in complex bending test 1. . . . .	96
3.33	Comparison of experiment and simulation for laminated reinforcement in complex bending test 1: the angle between the material director and the horizontal direction. . . . .	96
3.34	Comparison of the thickness in the material director direction between experiment and simulation for laminated reinforcement in complex bending test 1. . . . .	97
3.35	Deformation shape of laminated reinforcement in complex bending test 2: (a) Experiment. (b) Simulation (with midline plotting). . . . .	98
3.36	Comparison of the midline between experiment and simulation for laminated reinforcement in complex bending test 2. . . . .	98

---

3.37	Comparison of experiment and simulation for laminated reinforcement in complex bending test 2: the angle between the material director and the horizontal direction. . . . .	99
3.38	Comparison of the thickness in the material director direction between experiment and simulation for laminated reinforcement in complex bending test 2. . . . .	99
3.39	Three points bending test of interlock: (a) 20 mm displacement, left: experiment, right: simulation. (b) 40 mm displacement, left: experiment, right: simulation. (b) 60 mm displacement, left: experiment, right: simulation. . . . .	100
3.40	Comparison of the midline between experiment and simulation for interlock three points bending test. . . . .	101
3.41	Comparison of experiment and simulation for interlock three points bending with 40 mm displacement: the angle between the material director and the horizontal direction. . . . .	101
3.42	Comparison of experiment and simulation for interlock three points bending with 60 mm displacement: the angle between the material director and the horizontal direction. . . . .	102
3.43	L-flange bending deformation: (a) Experiment [LEU 16]. (b) Simulation with the specific plane shell element (with midline plotting). (c) Simulation with classical shell element for each ply in PAM-FORM [LEU 16] . .	103
3.44	(a):Book cantilever bending under gravity (Bending length 120 mm). Top: experiment, middle: simulation with Mindlin shell element, bottom: simulation with the specific plane shell element. (b): Laminated reinforcement cantilever bending under gravity (Bending length 118 mm). Top: experiment, middle: simulation with Mindlin shell element, bottom: simulation with the specific plane shell element. . . . .	104
3.45	Comparison of bending deformation shape between simulation with the Mindlin shell element S4R provided by ABAQUS and experiment . . . .	105
3.46	Comparison of the midline between experiment and simulation with the Mindlin shell element S4R provided by ABAQUS. . . . .	106
A.1	The schematic of the motion of geometry straight segments. . . . .	114

## List of Figures

---

# List of Tables

2.1	Properties of interested materials . . . . .	47
3.1	Mechanical properties of single page paper . . . . .	80
3.2	Mechanical properties of laminated reinforcement's single ply with taking into account the influence of friction on the bending stiffness . . . . .	93



# Notations

All notations are defined in the text when used first. The following is only a list of the most important symbols. In this thesis, the symbol's left superscript denotes the time of the configuration in which the quantity is measured.

## Chapter 2

$\mathbf{B}_j$	Control points
$M_{k,4}$	Basis functions of quartic B-spline
$t$	Global parameter value along the uniform quartic B-spline curve
$N_{h,4}(t)$	Basis functions of uniform quartic B-spline curve
$\mathbf{C}(t)$	Position vector of a point on the uniform quartic B-spline curve
$\chi$	Curvature
$M$	Bending moment

## Chapter 3

$\zeta^1, \zeta^2$	Element natural coordinates
$\mathbf{g}_1, \mathbf{g}_2$	Covariant vectors with respect to natural coordinates $\zeta^1, \zeta^2$
$p$	Index number of fiber segment
$T^{11}$	Fiber's tension force
$M^{11}$	Fiber's bending moment
$\epsilon_{11}$	Fiber's tensile strain
$\chi_{11}$	Fiber's curvature
$i$	Index number of time step
$t^i$	Time at time step $i$
${}^i\mathbf{F}_{\text{ext}}$	Single column matrix of external nodal loads at time $t^i$
${}^i\mathbf{F}_{\text{int}}$	Single column matrix of internal nodal loads at time $t^i$
${}^i\mathbf{F}_{\text{Tens-int}}^e$	Elementary tensile nodal loads at time $t^i$

${}^i\mathbf{F}_{Bend-int}^e$	Elementary bending nodal loads at time ${}^i t$
${}^i\mathbf{u}_N$	Single column matrix of nodal displacements from the initial configuration at time ${}^0 t$ to the configuration at time ${}^i t$
$\mathbf{e}_1, \mathbf{e}_2, \mathbf{e}_3$	Global cartesian unit base vectors
$N_k$	Interpolation function of node $k$
${}^i\mathbf{V}_m^k$	Material director of node $k$ at time ${}^i t$
${}^i\mathbf{n}_e$	Unit normal vector to the mid-surface of element $e$ at time ${}^i t$
${}^i\bar{\mathbf{n}}_s$	Unit normal vector to the geometry straight segment $s$ composed by the two endpoints of fiber segment at time ${}^i t$
${}^i h_k$	Element thickness along the material director ${}^i\mathbf{V}_m^k$ at time ${}^i t$
${}^i\mathbf{x}_k$	The position vector of node $k$ at time ${}^i t$
${}^i\mathbf{u}_k$	The displacement vector of node $k$ from the initial configuration at time ${}^0 t$ to the configuration at time ${}^i t$
$\Delta\mathbf{u}_k$	Incremental displacement vector of node $k$ from time ${}^i t$ to ${}^{i+1} t$ , $\Delta\mathbf{u}_k = {}^{i+1}\mathbf{u}_k - {}^i\mathbf{u}_k$
${}^i\mathbf{V}_1^k, {}^i\mathbf{V}_2^k, {}^i\mathbf{V}_3^k$	Local orthonormal frame defined for node $k$ at time ${}^i t$
$\alpha_k$	Rotation angle of material director ${}^i\mathbf{V}_m^k$ around ${}^i\mathbf{V}_1^k$ from the configuration at time ${}^i t$ to the configuration at time ${}^{i+1} t$
${}^i w$	Local curve constructed from the endpoints of any three adjacent fiber segments at time ${}^i t$
${}^i\varphi_j$	Relative angle of fiber endpoint $j$ at time ${}^i t$
$\Delta\varphi_j$	Incremental relative angle of fiber endpoint $j$ from time ${}^i t$ to ${}^{i+1} t$ , $\Delta\varphi_j = {}^{i+1}\varphi_j - {}^i\varphi_j$
${}^i\theta_j$	Rotation angle of fiber endpoint $j$ at time ${}^i t$
$\Delta\theta_j$	Incremental rotation angle of fiber endpoint $j$ from time ${}^i t$ to ${}^{i+1} t$ , $\Delta\theta_j = {}^{i+1}\theta_j - {}^i\theta_j$
$\Delta\mathbf{u}^f$	Single column matrix of incremental displacements of fiber endpoints
$\Delta\mathbf{u}^n$	Single column matrix of incremental nodal displacements and rotations of three adjacent elements
$\mathbf{Q}$	Transformation matrix between incremental relative angles of fiber endpoints and incremental nodal displacements and rotations
$\mathbf{T}$	Transformation matrix between incremental rotation angles of fiber endpoints and incremental nodal displacements and rotations
${}^i\mathbf{B}^{Ten}$	Strain-displacement matrix for tension at time ${}^i t$
${}^i\mathbf{B}^{Bend}$	Strain-displacement matrix for bending at time ${}^i t$

**Operators**

$\delta$	Variation operator
$\underline{\nabla}$	Gradient operator
$\dot{A}, \ddot{A}, \overset{\cdot\cdot}{A}$	The first, second and third derivative of quantity A



# Chapter 1

## Introduction

In the last few decades, there has been an increased trend to use composite materials as a better choice over the traditional metallic materials. Their advantages over other materials for high performance and lightweight applications have attracted many industries such as aerospace and automobile to explore and increase their usage. Both Airbus and Boeing, the two leading aircraft manufacturers, have made their efforts to reduce the structural weight and greatly increase the use of fiber reinforced composite materials in their new aircraft. This development can be seen by the new Boeing 787 Dreamliner which is the first commercial aircraft with both composite wings and fuselage, in which the total weight of the composite parts takes up 50% of the total structural weight [GRI 05]. In the automobile industry, due to the high manufacturing cost, composite materials are mostly confined

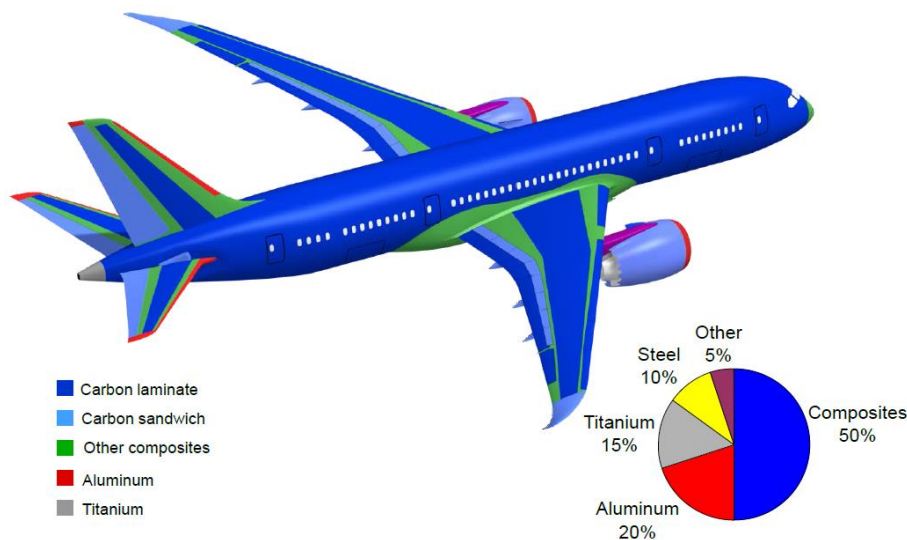


**Figure 1.1** – Application of composites in the Boeing 787 aircraft [BOE 13].

in race cars and high-end cars to make structure parts, such as bumper and door panels. Fortunately, some progresses have been made in reducing the production cycle time and raw material cost in the past few years. The BMW i3 is the first volume production vehicle

on market featuring a passenger cabin made of continuous fiber reinforced composites. In the near future, composite materials would be more extensively used in the ordinary passenger cars as increasingly fuel economy and tough carbon emission requirements.

# 1.1 Introduction to composite materials

## 1.1.1 Definition of composite materials

Composite materials (or composites for short) are very common in our daily lives, such as wood, bone, concrete and so on. There is no universally accepted definition for composite materials. The most widely used definition is composite materials are a combination of at least two different materials which results in better properties than when the individual component is used alone. The constituents of composite materials remain separate and distinct at the micro scale while forming into a single component. There are two categories of constituent materials: matrix and reinforcement. Matrix is to hold the reinforcement in the proper position and to transfer the loads. It also provides composites with toughness, damage tolerance and abrasion resistance. Reinforcement is usually much stiffer and stronger than matrix, its function is to carry structural loads and to provide stiffness and strength to composites. Composites can be classified into different categories based on the type of reinforcement and matrix [CAM 03].

## 1.1.2 Types of reinforcement

Generally, reinforcement in the composites can be present in three forms: particulate, short fiber and continuous fiber. Particulates are nearly equi-dimensional materials, which don't provide a substantial improvement on the mechanical properties of composites. Short fibers, such as chopped and milled fibres, have a variety of lengths, ranging from a few millimetres to a few centimetres. Composites reinforced with short fibers are generally isotropic for their mechanical properties. Continuous fibers are reinforcements with one dimension significantly larger than others. Among these three types of reinforcements, continuous fibers provide the best mechanical properties, especially when loaded parallel to the fiber direction.

Continuous fiber reinforcement (or called textile reinforcement) can be classified into woven, braided, weft knit and non-crimp according to its internal geometry structure (Figure 1.2). Woven fabrics are the most common reinforcements due to their good drapeability and availability. They are available as 2D and 3D forms. 2D woven fabrics consist of two orthogonal series of yarns, referred to as warp and weft yarn (yarn is a term used to call a bundle of fibers). The warp yarn direction is parallel to the length of roll, while the weft yarn direction is perpendicular to the warp yarn. There are many weaving patterns for 2D woven fabrics, such as plain weave, satin weave, twill weave and so on [CAM 03]. The weaving pattern is called balanced if the amount of warp and weft fibers on each side of the weave per unit area is the same. The weaving pattern is called regular if the

amount of warp and weft fibers per unit width is equal. Plain weaves are both balanced and regular for most applications. Satin weaves can be regular but never balanced, either more warp or weft fibers are on a side of the weave.

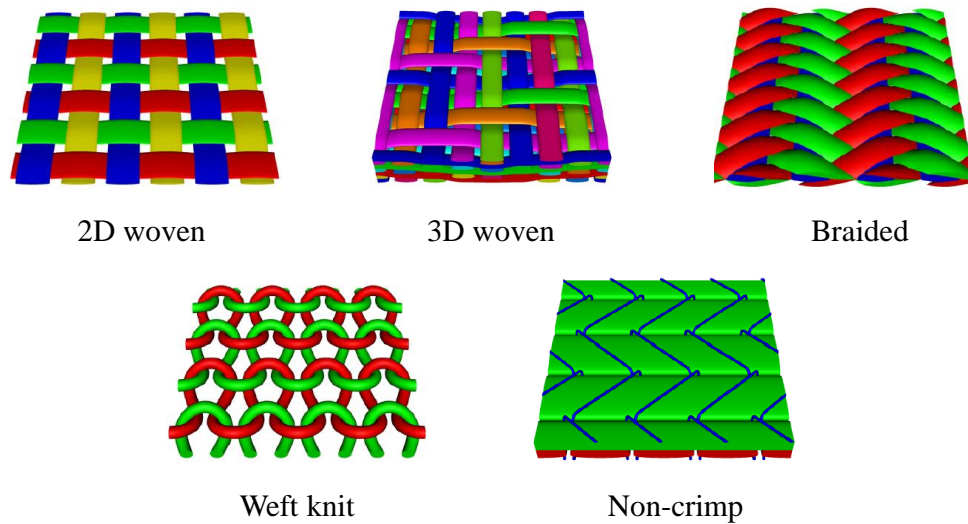


**Figure 1.2** – Images of different internal structures for reinforcement [SHE 07].

3D woven fabric is developed in the 1970's, and characterized by yarns interlaced not only in plane, but also in through thickness direction (or Z direction) resulting in higher through thickness strength and stiffness of final composites [STI 12]. There are three types of 3D woven fabrics according to their weaving structure patterns: multi-layer, orthogonal and angle interlock. Multilayer woven fabrics consist of multiple layers, each of which has its own sets of warp and weft yarns. The connection of layers is done by self-stitching or central stitching. Orthogonal woven fabrics consist of three sets of yarns that are perpendicular to each other. One particular weaving structure form for orthogonal woven fabric is Z direction yarns interconnect all individual warp and weft yarns and thus solidify the fabric. In angle interlock, there are at least two sets of yarns such as warp and weft. In some cases, in order to increase fiber volume fraction and in-plane strength, stuffer yarns can also be added. Angle interlock is divided into two groups: through thickness angle interlock and layer to layer angle interlock (Figure 1.3). In through thickness angle interlock, warp yarn travels from one surface of the 3D fabric to the other holding all the layers together, where as in layer to layer angle interlock, warp yarn travels from one layer to the adjacent layer and back. A set of warp weaves together hold all the layers of the weave structure. Composites with 3D fabrics have advantages of enhanced delamination resistance, fracture resistance, damage tolerance and dimensional stability compared with 2D fabrics [BAD 07a].

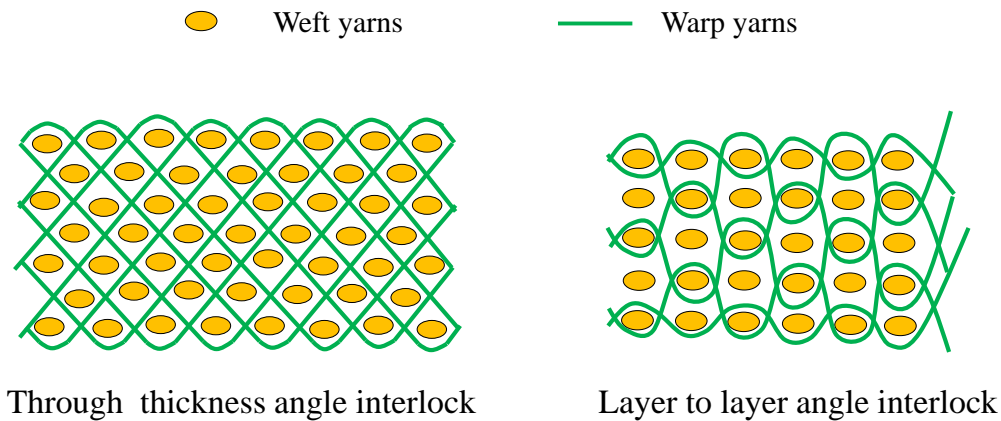


**Figure 1.3** – Internal weaving structure forms of angle interlock.

### 1.1.3 Types of matrix material

There are three types of matrix materials, they are polymer, metal and ceramic. Consequently, composites can be classified into polymer matrix composites, metal matrix composites and ceramic matrix composites. Polymer is the dominant matrix in most composites applications. It can be classified as either thermoset or thermoplastic resin (resin is a generic term given to call polymer matrix).

Thermosetting resins are low molecular weight and low viscosity monomers that are converted during the curing process into three dimensional cross-linked structures. Cross-linking results from chemical reactions that are driven by heat which is generated either by chemical reactions themselves or by externally supplied heat. Thermosetting resins mainly include polyesters, epoxies and polyamides. Polyesters are commonly used in fiber reinforced plastics, and epoxies make up most of the market for advanced composites resins [CON 88]. Thermosetting resins, because of their three-dimensional cross-linked structure, tend to have high dimensional stability, high-temperature resistance and good resistance to solvents.

Thermoplastic resins, sometimes called engineering plastics, include polyetherimide (PEI), polyphenylene sulfide (PPS), polyetheretherketone (PEEK) and so on. They consist of long, discrete molecules that melt to a viscous liquid at the processing temperature (generally close to resin's melting temperature), and after forming, are cooled to an amorphous, semi-crystalline or crystalline solid. The degree of crystallinity has a strong effect on the final matrix properties. Unlike the curing process of thermosetting resins, the processing of thermoplastics is reversible, by simply re-heating to the processing temperature, the resin can be formed into another shape if desired. Thermoplastic resins offer great promise for the future from a manufacturing point of view, since it is easier and faster to heat and cool a material than to cure it. This makes thermoplastic resin very attractive for high volume industries, such as the automobile industry.

### 1.1.4 Prepregs (Pre-impregnated composites)

Prepregs are composite materials in which fiber reinforcements have been pre-impregnated with thermoplastic or thermoset resin in a certain ratio. They have very high fiber content (up to 65% by volume). Prepregs are commercially available in a number of different intermediate material forms and there are several types (Figure 1.4). They can be categorized by their fiber type, reinforcement architecture and matrix distribution. Thus, reinforcement architecture can be a textile form or fully aligned (UD), while matrix distribution can be consolidated, commingled and powder impregnated. To reduce the aging or advancing process of thermoset resin, thermoset prepregs should be kept at a low temperature. Thermoplastic prepregs usually have no limit to shelf life due to their resin's chemical stability, so they can be heated and formed repeatedly. Processing speed and recyclable are the primary advantages of thermoplastic prepregs over thermosetting prepregs.

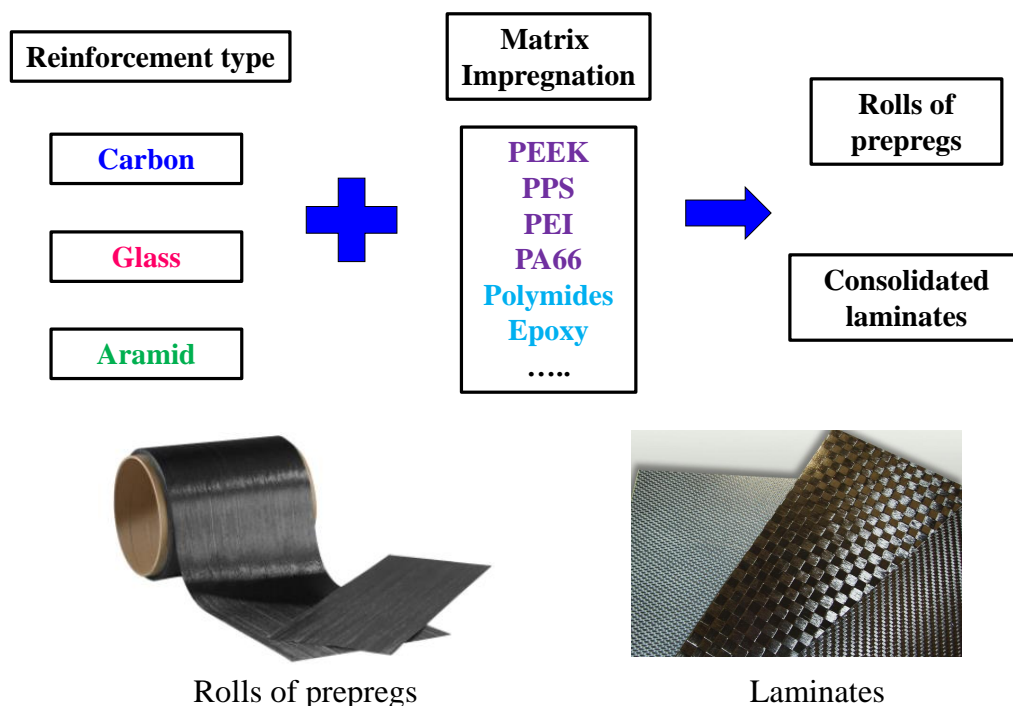


**Figure 1.4** – Definition of Prepregs and their types.

Prepregs are popular due to a number of advantages, such as very precisely controlled fibre/resin ratios and good mechanical performance. Prepregs can be applied to many processes ranging from hand lay-up to highly automated placement processes such as automated tape laying (ATL). Prepregs are used in applications ranging from leisure to aerospace.

## 1.2 Processing techniques for polymer composites

There are variety of processing methods available to manufacture polymer composite part. Depending on the quality, quantity and cost of the part, a suitable processing method can be selected. Here, a brief introduction about resin transfer molding (RTM) , thermo-forming and autoclave forming would be given since these three manufacturing processes are extensively used for mass production.

### 1.2.1 Resin transfer molding (RTM)

Resin transfer molding (RTM), the most widely used of liquid molding processes, is a closed mold process which is well suited to fabricate very complex shape and dimensionally accurate parts [BAL 13]. Generally, this process is used to manufacture a composite part from dry reinforcement. It's composed of mainly two steps: dry reinforcement forming and resin injection (Figure 1.5). Dry reinforcement forming aims to press the reinforcement into shape of final part by the external force. Subsequently, the preform is placed within a mold cavity and a low-viscosity resin (often with hardener) are injected

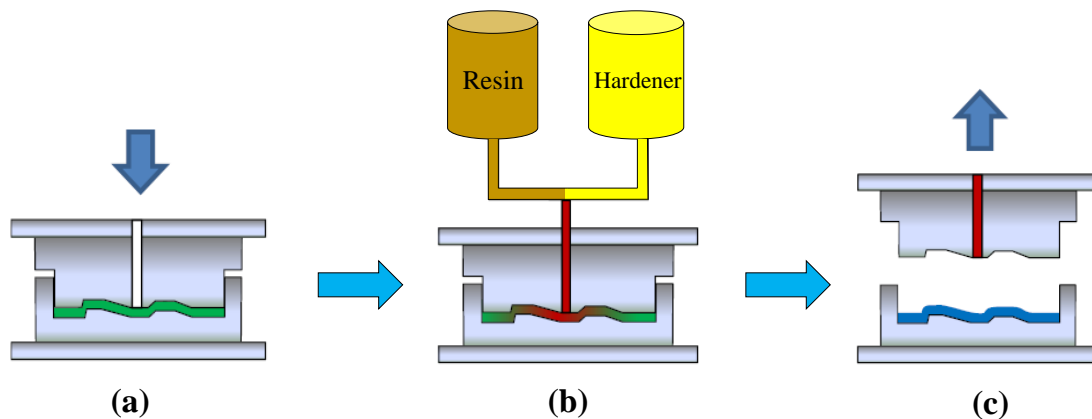


**Figure 1.5** – RTM process. (a) Dry reinforcement forming. (b) Resin injection. (c) Final composite part.

under pressure to fill the closed mold. Polyester and epoxy resins are commonly used since their short cure time. The pressure must be sufficient for the flow of resin into the entire space within the mold cavity, but the pressure should not be too high to cause fiber wash. When the resin is reconsolidated, the final composite part can be obtained. Over the years, some improvements have been made in RTM process. Two of the improved versions are vacuum-assisted resin transfer molding (VARTM) and Seemann composite resin infusion molding (SCRIMP). These two processes have a better resin impregnation on the reinforcement and facilitate the removal of entrapped air to reduce the possible voids in the final composite part.

## 1.2.2 Thermo-forming process

Thermo-forming process is used to manufacture thermoplastic composites part from thermoplastic prepregs. It mainly contains three stages: heating, forming and consolidation. There are three types of thermoforming processes based on the method to force the prepregs into the shape of mold in the forming stage, which are thermo-vacuum forming, thermo-compression forming and thermo-stamping. Thermo-vacuum forming shapes the prepreg by means of the vacuum produced in the mold cavity space, thermo-compression forming by means of high pressure and thermo-stamping by means of external mechanical force. Figure 1.6 shows the schematic of thermo-stamping process. The thermoplastic

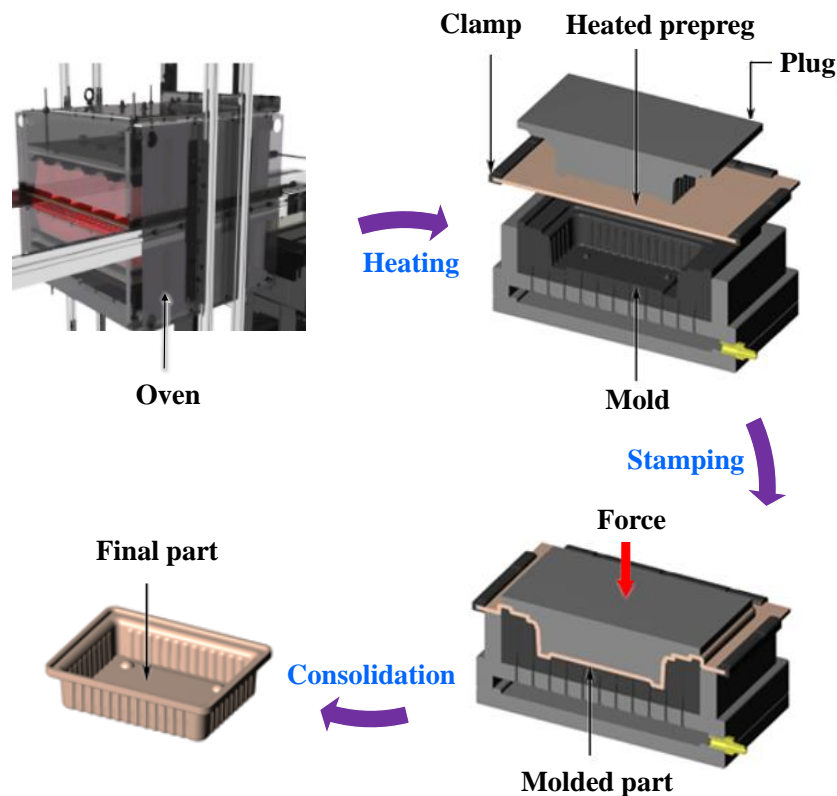


**Figure 1.6** – Schematic of thermo-stamping process [HTT 14].

prepreg is clamped with a holding device and heated in an oven using either convection or radiant heat until it is softened (generally close or above resin's melting temperature). The prepreg is then held horizontally over a mold and pressed into the mold with the plug. The softened prepreg conforms to the shape of the mold and is held in place while it cools. The excess material can be trimmed away and the final composite part is obtained. The cycle time of thermo-stamping process is very short, so it has a very high production efficiency.

### 1.2.3 Autoclave forming process

Autoclave is a closed and heated pressure vessel, which can be applied to moulding processes where high pressure and temperature are required (usually for thermoset preregs, Figure 1.7). Autoclave forming can be applied to the manufacturing of high quality structural component with high fibre volume fraction, but it requires high cost due to the expensive equipment and long cure cycle time. During autoclave forming of composites, the autoclave temperature is raised to the required value, and then the pressure is increased to impose the forming deformation, finally the component is cooled under certain consolidation pressure. Long cure cycles are usually required as the autoclave mass is large and takes a long time to heat up and cool down [WAN 08].

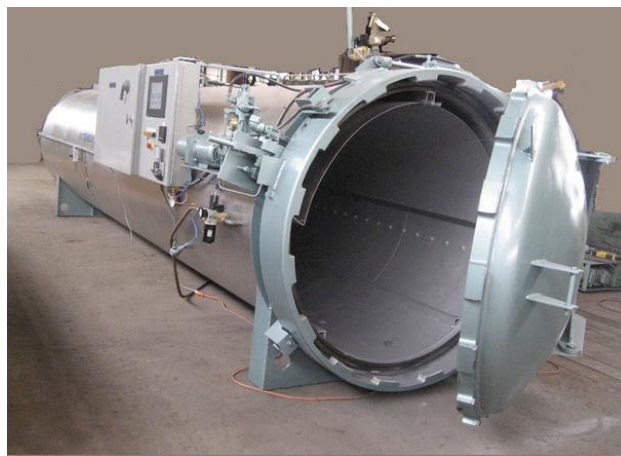


**Figure 1.7** – Configuration of autoclave.

## 1.3 Deformation mechanisms of polymer composites

To investigate the deformation behaviours in the forming process, three different scales have been proposed: macroscopic, mesoscopic and microscopic (Figure 1.8). Macroscopic scale refers to the full scale of reinforcement or composites. At this scale, the reinforcement or composites is generally taken as an equivalent continuous media with specific constitutive behaviour. Mesoscopic scale refers to see the reinforcement or composites as interlaced yarns. The interaction between yarns and the geometry of yarns are needed to explicitly define and describe. Microscopic scale refers to take the reinforcement or composites as composed of large number of continuous fibers. A detailed description of fiber's geometry and interaction between fibers are required.

### 1.3.1 Microscopic scale: Fibers

The microscopic scale is the smallest scale designated for textile reinforcements or composites. Fibers are the most basic constituents at this scale and the geometry shape of fiber

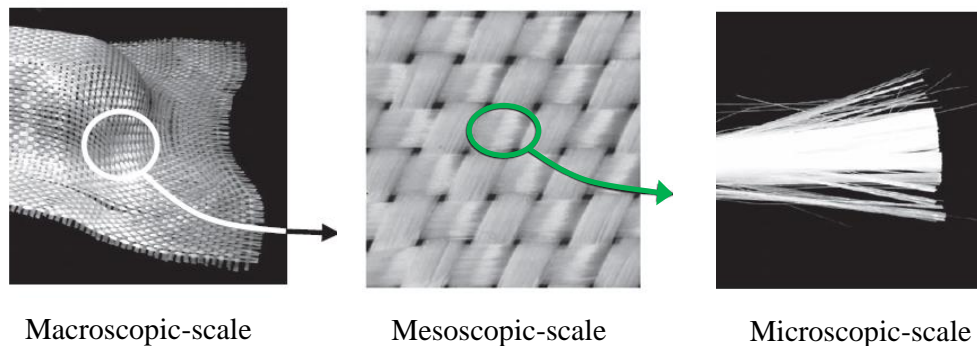


**Figure 1.8** – Three research scales for textile composites.

is required to be explicitly defined. Fibers are mainly subjected to tensile and bending deformations. Although fiber is a continuous material, due to its very small dimension, it's very difficult to characterize its mechanical behaviour using the conventional testing device. Some devices specifically for testing fiber's tensile properties were proposed in [KAN 13]. Fiber's bending property can be derived from its tensile modulus since it's a continuous material.

### 1.3.2 Mesoscopic scale: Yarns

At the mesoscopic scale, the main interested aspects are yarn's deformation behaviours. They not only depend on single fiber, but also the interactions between them. X-ray tomography is a non-destructive optical measuring method and is widely used to observe yarn's shape and fibers distribution. With the help of tomography, an accurate description of yarn's shape before and after deformation can be constructed.

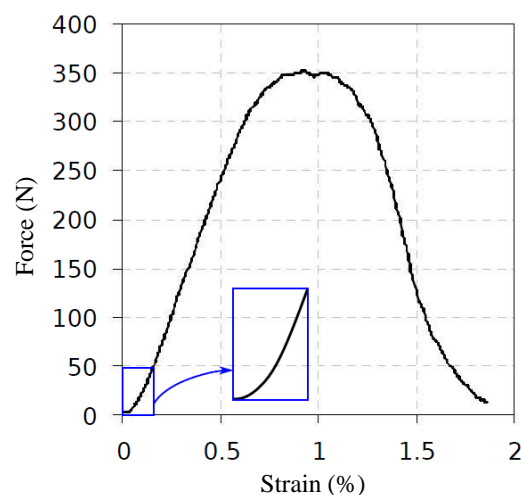


**Figure 1.9** – Yarn's tensile behaviour [DUM 03].

### 1.3.2.1 Yarn's tensile deformation

Yarn is made of fibers, when a yarn is stretched, not all fibers inside it would be stretched simultaneously. This results in a non-linear tensile behaviour at the beginning of the loading. This non-linear behaviour depends on the type of fiber and fabrication process of yarn. Figure 1.9 presents a typical tensile test result for a single yarn that made of glass fibers, the non-linear tensile behaviour can be observed at the beginning of loading.

The tension test of yarn has been standardized (using the ASTM D4018-81) [HIG 90]. The sample is required be composed of at least 10000 fibers and impregnated with resin to make all fibers in a yarn as straight as possible. C.Florimond [FLO 13] proposed a tensile test device for yarn made of less than 2000 fibers (Figure 1.10a). Two round metal bars were installed on the top clamp and bottom clamp respectively. The yarn twined around these metal bars, when it was subjected to tension, it equals two yarns under tension. The testing results indicate it can capture the non-linear tensile phenomenon of yarn (Figure 1.10b).

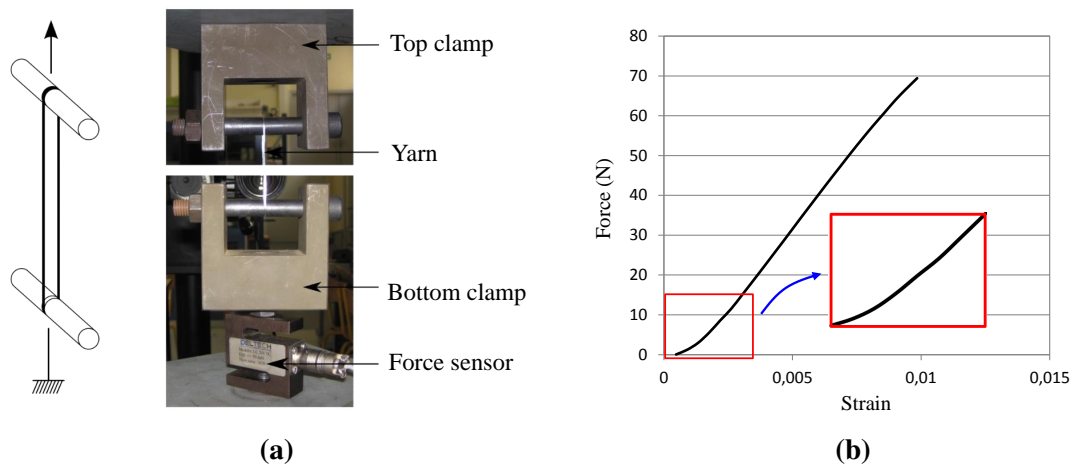


**Figure 1.10** – Yarn's tensile behaviour test device proposed by C.Florimond. (a) Configuration of test device. (b) Yarn's tensile test result [FLO 13].

### 1.3.2.2 Yarn's transverse compaction

Yarn's transverse compaction is defined as the area variation of yarn's transverse cross-section when compressed. The rigidity in yarn's transverse cross-section is much smaller than rigidity in its longitudinal direction, which makes compression the main deformation mode. Yarn's compression directly affects fiber's distribution, which would ultimately influence the permeability of resin. When a yarn is compressed, the space between fibers would reduce. Initially, there is little or no resistance to the compression. As compression continues, more and more fibers would come into contact, resulting in a great increase in compression rigidity. This whole process can be seen in Figure 1.11 where the yarn is

subjected to the compression introduced by the biaxial loading. The experimental characterization of single yarn's transverse compaction is very difficult to implement, primarily due to its small dimension. It's often conducting the compaction test at the macroscopic scale and using the inverse method to identify single yarn's transverse compaction behaviour [GAS 00].

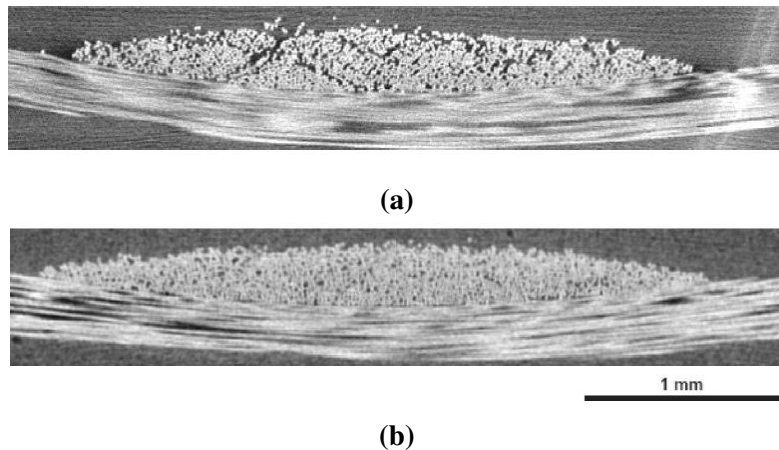


**Figure 1.11** – Fibers distribution in a yarn: (a) Unloaded. (b) Subjected to biaxial tension [BAD 08].

### 1.3.2.3 Yarn's shearing deformation

There are two modes of shearing for yarn: transverse shearing and longitudinal shearing (Figure 1.12). Yarn's transverse shearing is defined as the shape change of transverse cross-section of yarn, in which fibers are redistributed. The main resistance of yarn's transverse shearing comes from fibers inter-friction force, which is strongly influenced by yarn's compression. This is also true for longitudinal shearing of yarn, in which friction provides the main rigidity. The coupling between the shearing and compaction makes it very difficult to directly characterize yarn's shearing by experiment, the inverse method is usually employed to identify yarn's shearing behaviour [FLO 13].

### 1.3.2.4 Yarn's bending deformation

There are few studies about yarn's bending behaviour, partly because the bending stiffness is very small, it's neglected. Another important reason is its complexities. When a yarn is bent, there could exist relative sliding between fibers. This makes yarn's bending stiffness not directly related to its in-plane tensile modulus as the classical continuum materials. Yarn's bending stiffness not only depends on the fibers, but also their inter-friction force. Some mechanical models have been proposed to calculate yarn's bending stiffness from fibers [GRO 66, POP 66, GRO 80]. However, these models are based on many assumptions, they can only be applied to some simple cases. On the experimental aspect, B.

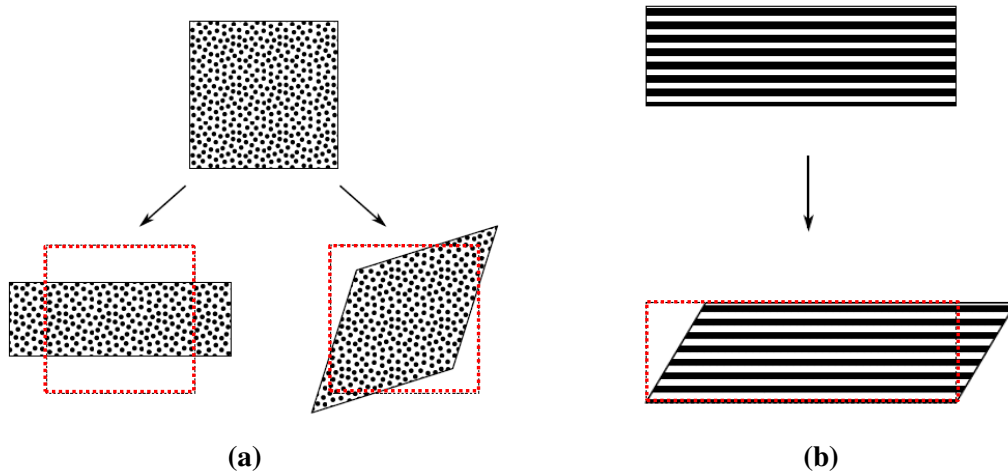


**Figure 1.12** – Two modes of yarn’s shearing: (a) Transverse shearing. (b) Longitudinal shearing [FLO 13].

cornelissen et al [COR 09] conducted a cantilever bending test to identify yarn’s bending stiffness as the slope of moment-curvature curve. It’s the most direct way to characterize yarn’s bending stiffness.

### 1.3.3 Macroscopic scale: Reinforcements or composites

At the macroscopic scale, some well-known deformation mechanisms are detailed as followings.

#### 1.3.3.1 In-plane shear deformation

In-plane shear is the most dominant deformation mode for reinforcement and prepreg in the forming, involving yarn rotation around the weaving cross-over point. The main resistance of in-plane shear comes from the friction between yarns and fibers. In-plane shear occurs when there is a change in angle between two yarn directions. The in-plane shear of prepreg is temperature dependent due to the presence of resin. The in-plane shear characterization for woven reinforcements and prepregs reinforced with woven reinforcements can be carried out by two standard tests: picture frame and bias extension tests.

**Picture frame test** has been widely used to characterize the in-plane shear behaviour of woven textile reinforcements and thermoplastic prepregs. The picture frame is made of four bars of equal length (Figure 1.13). Four bars are hinged at each corner so that the initially square frame becomes a rhombus when loaded by a tensile machine. Tensile force data is recorded during the test. Typical non-linear shear data is shown in Figure 1.14. It shows for the small rotation angles, the relative displacement field inside a yarn is a rotation field. Strains in the yarn are negligible. The shear load is mainly due to friction between the warp and weft yarns. The locking angle corresponds to the angle from which

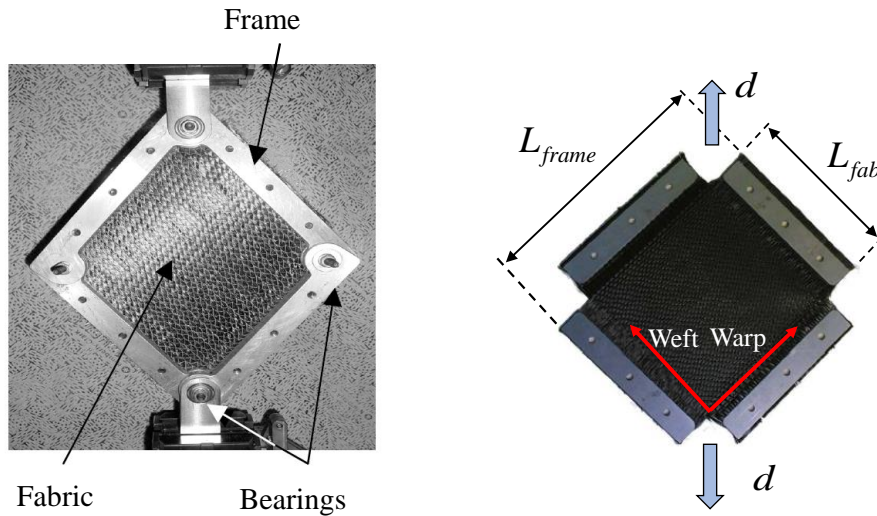


**Figure 1.13** – Picture frame test device and the shape of sample.

the geometry of the weaving does not allow this rotation any more, and consequently, yarns are subjected to contact with other yarns. The relative displacement field inside a yarn shows that the yarn is in lateral compression. This compression is more important as the shear increases and finally it can cause the appearance of wrinkles.

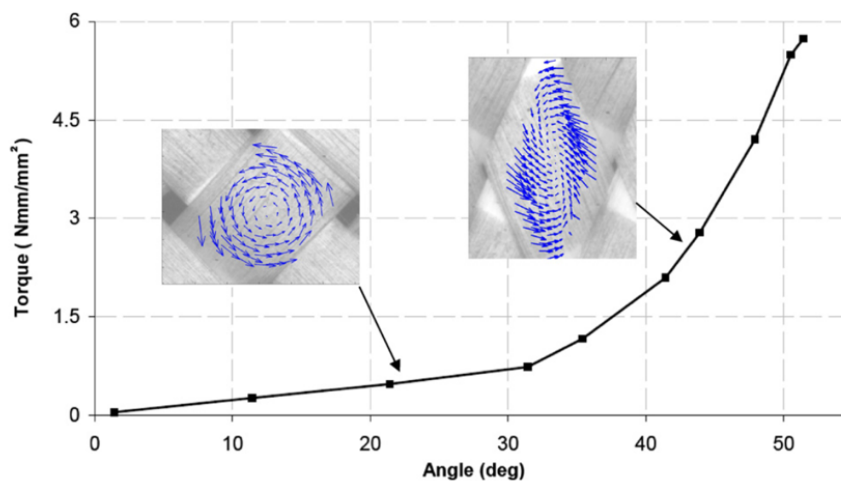


**Figure 1.14** – In-plane shear curve of the plain weave fabric [ZOU 06].

In the picture-frame test, testing of complete square sample is possible, depending on the design of the picture frame equipment. However, the corners of each fabric specimen are commonly removed to permit free rotation of frame bearings and prevent premature fabric wrinkling due to local over compaction (Figure 1.13). In picture-frame test, careful fabric handling and alignment is required in the clamping. A consequence of incorrect clamping the specimen is the possibility of introducing tensile fiber strains. If fibers are

misaligned with picture frame edge, only small deviations would cause large errors in the measured force due to the high fiber tensile stiffness.

The load recorded by the load cell of the tensile machine is generally recalculated into shear force or shear moment (per unit area fabric) using equivalence of the mechanical work and normalization method. When processing the results, two assumptions concerning the deformation of the fabric sample are made: the first is the shear deformation in the sample is homogenous, the second is the shear angle of the fabric is the same as the shear angle of the frame. Geometrically, the shear angle (radians) of the deformed picture frame with a vertical displacement of “d” is calculated as:

$$\gamma = \frac{\pi}{2} - \theta = \frac{\pi}{2} - 2 \cdot \cos^{-1} \left( \frac{\sqrt{2}}{2} + \frac{d}{2L_{frame}} \right) \quad (1.1)$$

**Bias extension test** (BE test) is commonly preferred to characterize in-plane shear for woven fabrics and preregs due to the simplicity of test procedure and minimal equipment requirement [HAR 04]. It's performed on a sample in which the warp and weft yarn directions initially are orientated at 45° to the load direction. Unlike picture frame test, BE test is less sensitive to misalignment due to its free boundary conditions. Specimens were cut into the shape shown in Figure 1.15a, which comprises regions A, B, C and clamp area. In region C, both warp and weft yarns have a clamped end and there is no shearing deformation. In region A, both warp and weft yarns have the free ends, if there is no sliding at the crossovers, the stretching of sample leads to a pure in-plane shear deformation. In region B, one yarn direction is clamped at its end, the other direction is free, the stretching leads to a shear strain of a half value of region A. The trapezium shape of the clamp area is to hold the yarns at the border of regions C and B so as to eliminate any yarn slip in region C. The aspect ratio ( $L$  to  $W$ ) must be at least 2 in order for all three regions to exist. The shear angle (radian) in the pure shear region A, when imposed the end displacement  $U$ , can be calculated as:

$$\gamma = \frac{\pi}{2} - 2 \cdot \cos^{-1} \left( \frac{L+U}{\sqrt{2}L} \right) \quad (1.2)$$

In the BE test for thermoplastics, such as prepreg, an environmental chamber is needed to heat sample to the elevated temperature. Wang [WAN 14] and Guzman [GUZ 15] have conducted the BE test for thermoplastics at various high temperatures, respectively. They used the same testing device as shown in Figure 1.16. To prevent the slippage of the sample when resin is melted in their tests, a specific spring system is employed to assist the clamps to clamp the sample (Figure 1.16).

### 1.3.3.2 Biaxial tensile deformation

Unidirectional fiber materials will typically exhibit a linear force-displacement response when loaded parallel to the fiber axis. This is not the case for textile materials. The textile reinforcements, for example woven fabrics, have yarn undulations because of woven architecture. When a woven fabric is subjected to a tension, the undulated yarns tend to

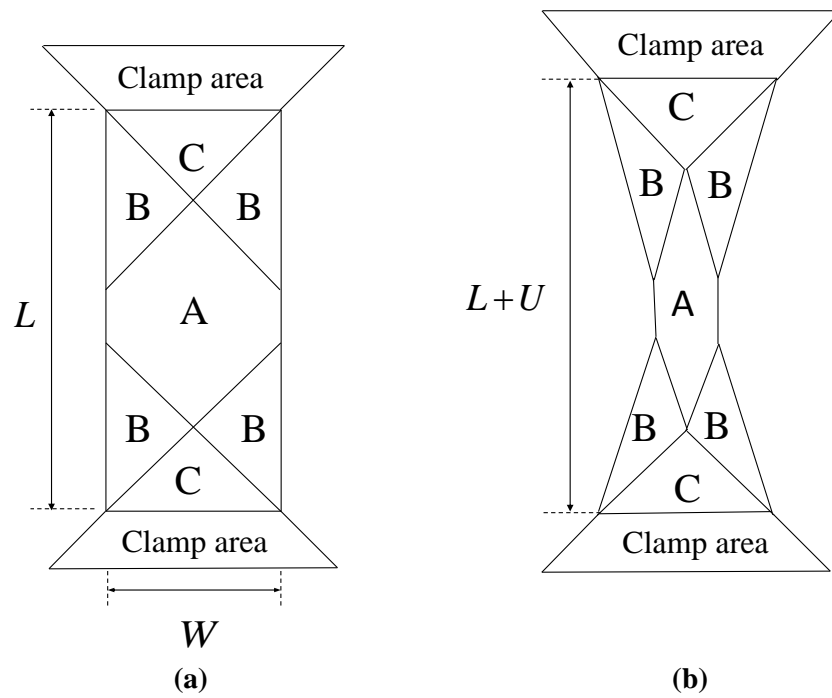


**Figure 1.15** – Schematic of an idealized sample used in BE tests. (a) Un-sheared sample. (b) Sheared sample [WAN 08].

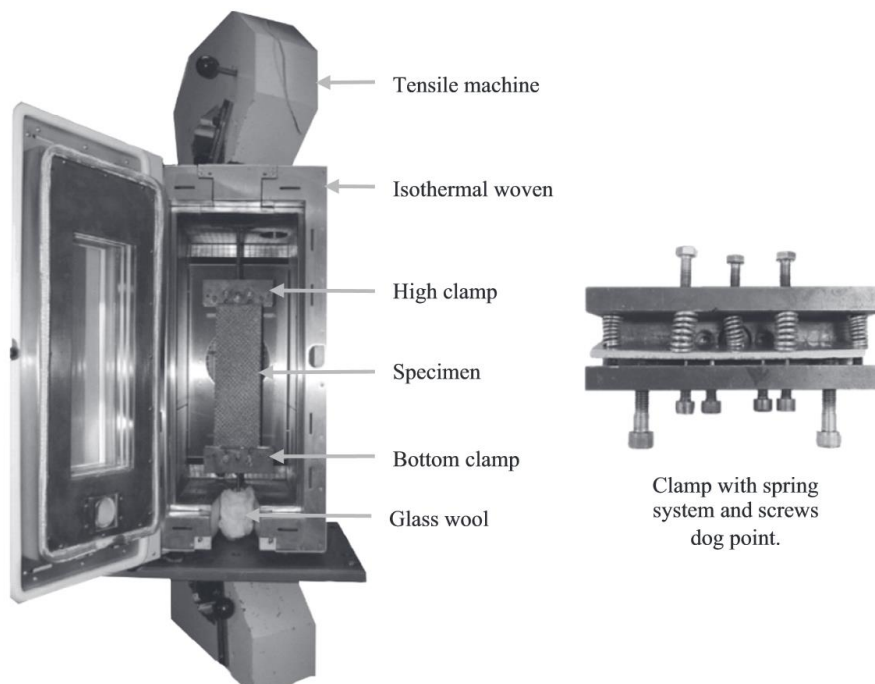


**Figure 1.16** – Bias extension test set-up for thermoplastic composites [WAN 14].

become straight. That leads to a non-linear tensile behaviour at the beginning of the load-

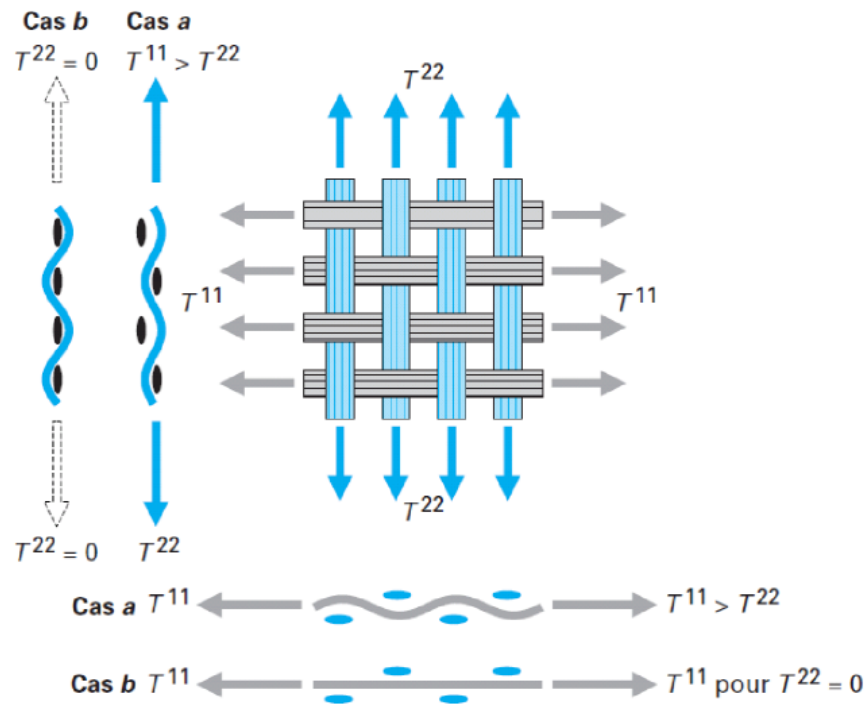
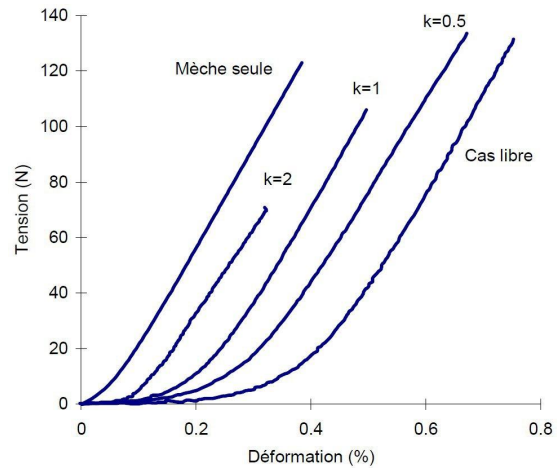
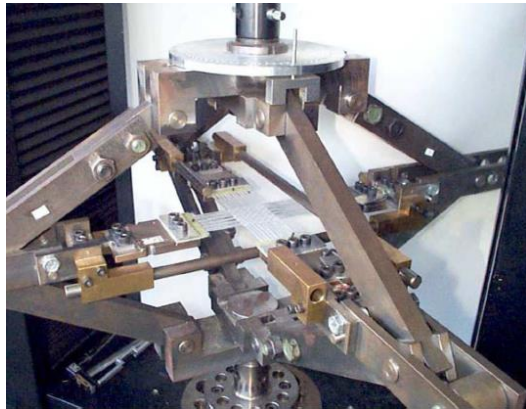


Figure 1.17 – Schematic of biaxial phenomenon [BOI 04].

ing. Because the yarns are woven and undulated in both warp and weft directions, when one of the yarn directions is pulled, it tends to reduce its waviness and becomes straight if the other direction is left un-stretched. The un-stretched yarns become more undulating and consequently the fabric is under equilibrium. This phenomenon is called biaxial (Figure 1.17). This is very analogous to the conception Poisson ratio in the continuum mechanics: when one direction is deformed, it would have influence on other directions. By using biaxial tensile device it's possible to impose a range of coupled deformations or different ratios of deformations along the two yarn directions. This biaxial effect with different strain ratios  $k$  along two yarn directions is shown in Figure 1.18 for a woven fabric.

### 1.3.3.3 Transverse compaction/consolidation

Transverse compaction is a non-linear phenomenon. At the end of forming, the material must be compacted to increase the fiber volume fraction and to eliminate the voids for preregs. For structural applications, it is important to obtain acceptable void content, typically <1% for aerospace applications. An understanding of compressibility, typically in terms of compaction pressure versus fiber volume fraction, allowing the required pressure to be determined for the desired fiber content [LON 14]. For multi-layer preforms, the compressibility of each material type is likely to be different so that each layer attains a different fiber volume fraction under the imposed compaction pressure. Robitaille et



**Figure 1.18** – Biaxial tension test device and measuring results [BUE 01].

al [ROB 98] published an extensive review of both experimental methods and modelling approaches for dry reinforcement compaction. Q.T.Nguyen et al [NGU 13] investigated the compaction behaviour for multi-layer textile reinforcements and analysed the compressive behaviour at the mesoscopic scale (Figure 1.19). Compaction testing procedures are relatively simple, with material compacted between two parallel platens by a tensile machine as shown in Figure 1.19.

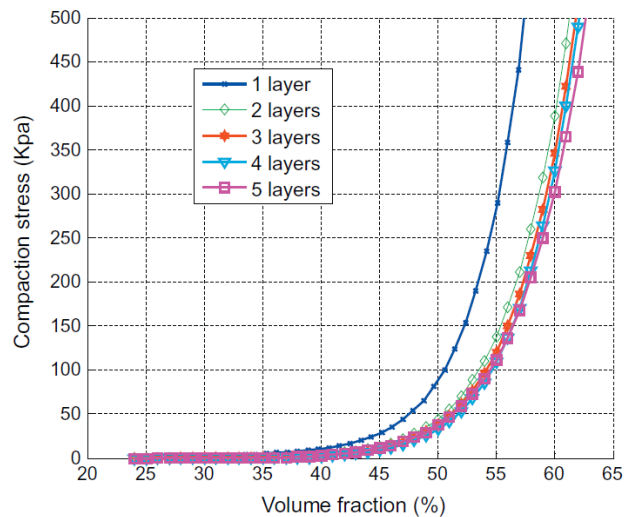


**Figure 1.19** – Transverse compaction device and measuring results [NGU 13].

The majority of thermoset and thermoplastic prepregs would undergo limited thickness reduction during consolidation (typically <20%). This is due to these materials being usually in semi-finished form and already being relatively well consolidated. As these materials have no clear paths for entrapped voids to escape, very high pressure is required to achieve the desired degree of consolidation. Hence, reasonably high-pressure

autoclaves are usually employed to consolidate these materials [LON 14]. Many authors have conducted consolidation experiments for both thermoset and thermoplastic materials [VAN 91, WIL 99, BER 01], in which all used a similar approach as described above for dry fabrics. As it would be expected, this behaviour is highly dependent on temperature and loading rate, with increasing time at pressure resulting in a reduction in void content to a limiting value.

### 1.3.3.4 Longitudinal and transverse shearing deformation

Longitudinal and transverse shearings are used to describe the angle variation of cross-section in the longitudinal and transverse direction of composites structure, such as for laminated composites or interlock reinforcement. Overviews of their characterization have been given by many authors [HAR 05, CHA 12, HAA 14a]. Several set-ups are able to characterize both the longitudinal and transverse shearings [ORL 12, HAA 14a]. Figure 1.20 presents one set-up for interlock reinforcement to characterize its transverse shearing. Experimental results are presented either by using the linear visco-elasticity theory, or with models that neglect viscous contributions and only consider the elastic part of the response.

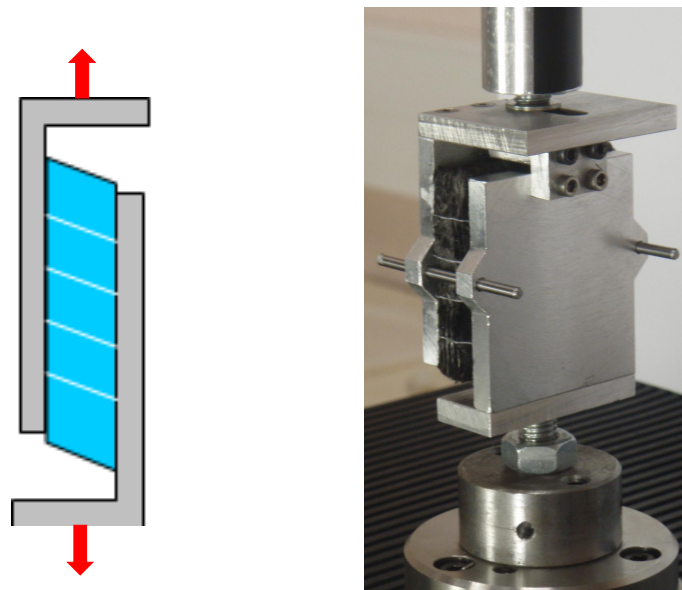


**Figure 1.20** – Longitudinal and transverse shearing test device for interlock reinforcement [CHA 12].

### 1.3.3.5 Bending deformation

The ability of reinforcement or prepreg to bend out of plane is very critical for forming of curved composite part. It is a little surprising that this topic has received relatively

little attention, at least for fabric reinforcements and prepregs. One main possible reason is that most simulation models are based on the membrane assumption, bending stiffness is neglected. However, many recent studies have shown that bending stiffness plays a very important role in the forming simulation, especially to the development of wrinkles [HAM 07, BOI 11] (Figure 1.21). It's very necessary to take into account the bending stiffness. Unlike the conventional continuous materials, the bending stiffness of fibrous material is not directly related to its in-plane tensile modulus. Therefore, it needs to measure the bending stiffness through the experiment. One objective of this thesis is to propose a bending stiffness test method for thermoplastic prepregs at high temperature. The detailed information about this approach would be given in chapter 2.

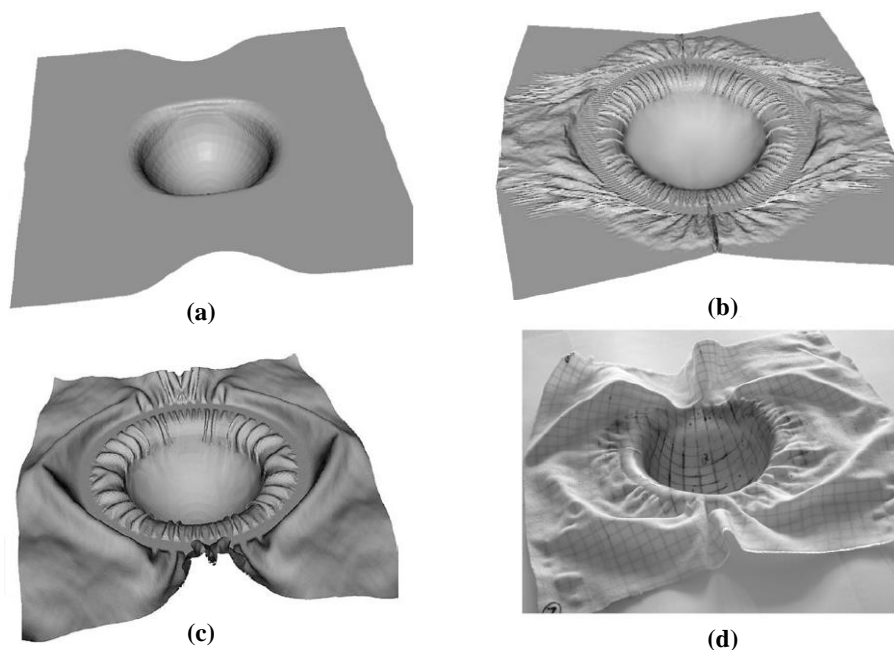


**Figure 1.21** – Forming of an unbalanced textile reinforcement. (a) Tensile stiffness only. (b) Tensile + in-plane shearing stiffnesses. (c) Tensile + in-plane shearing + Bending stiffnesses. (d) Experimental forming [BOI 11]

## 1.4 Simulation models in the forming

### 1.4.1 Simulation models at microscopic scale

In the microscopic scale simulation models, fibers are generally modeled as beam elements. There are many studies at this scale, but the main challenges are too many contacts between fibers and the computation cost is huge. Figure 1.22 shows in-plane shear simulation for a plain weave based on the models proposed by Damien [DUR 10], in which

each fiber is simulated with 3D beam element and contact-friction interactions between fibers have been accounted.

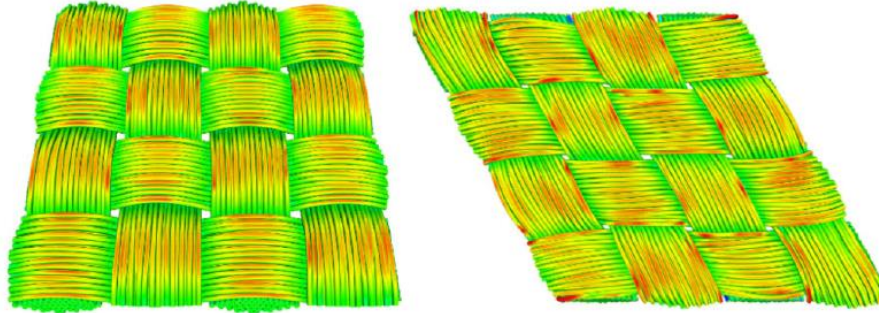


**Figure 1.22** – Simulation of in-plane shear at the scale of fibers [DUR 10].

### 1.4.2 Simulation models at the mesoscopic scale

The mesoscopic scale simulation models are generally used to simulate the deformation within a representative unit cell (RUC) which is made of yarns. At the mesoscopic scale, it allows to get the knowledge of geometry and stress-strain state for yarn after deformation. There are three principal works needed to be done in the mesoscopic scale simulation models: (1) Construction and meshing of geometrical structure of reinforcement internal geometry within a representative unit cell (RUC). (2) Application of homogenization to calculate local properties of yarns or impregnated yarns, accounting for local fiber volume fraction and fiber orientation. (3) Definition of periodic boundary conditions on RUC [LOM 08].

Several models have been proposed to construct the geometrical structure for yarns. Kawabatta model is well known due to its simplicity and efficient [KAW 73, BUL 00]. Yarns were seen as a composition of hinged bars, but this model is not 3D consistent. If the 3D model of each yarn is constructed through the sweeping of yarn's cross-section along the trajectory that is composed of the Kawabatta 2D bars, there would have interpenetration between yarns. S.Lomov et al [LOM 00] proposed a mesoscopic model for 2D and 3D fabrics. Some techniques were applied in his model to avoid the interpenetration, but the cross-section of yarn in his model was considered as circular and kept constant along the trajectory, which was a little far from the reality. Latter, he proposed an improved model that the shape of yarn's cross-section can be more complex, such as the lenticular and elliptical shape [LOM 07]. However, the cross-section was still assumed to be constant along the trajectory. Hivet et al [HIV 05] developed a 3D geometrical model for yarns, in which yarn's cross-section shape came from the experiment observation. This model is able to accurately describe yarn's cross-section variation along the trajectory without interpenetration. Naouar et al [NAO 14] proposed a method to construct the yarn geometry from X-ray tomography for 2D and 3D fabrics and some simulations were performed based on this model.

Solid elements are usually used to mesh the yarns in these mesoscopic scale simulation models in order to simulate yarn's cross-section shape change during deformation. The main problem lies in the large computation cost. Recently, Gao et al [GAO 15] have proposed a new 3D beam element to simulate yarn at the mesoscopic scale. The cross-section of this beam element can change in the deformation, therefore, it can greatly reduce the number of elements to discretize yarn and improve the calculation efficiency.

Representative unit cell (RUC) is the smallest periodic structure for a periodic medium. For a periodic medium, the selection of the RUC is not unique and would affect the boundary condition imposing. Figure 1.23 shows two RUC patterns for the same fabric. In the case of RUC (a), despite the geometric boundary of the RUC is square, only a fraction of this boundary corresponds to the material points of yarns. Kinematic boundary conditions can be only applied on the material boundary. This would lead to the difficulty to impose the periodic boundary conditions. For RUC (b), the geometric boundary is also the material boundary, this permits to directly impose the periodic boundary condition on this boundary. Consequently, if RUC (b) is possible, it is suggested to choose it.

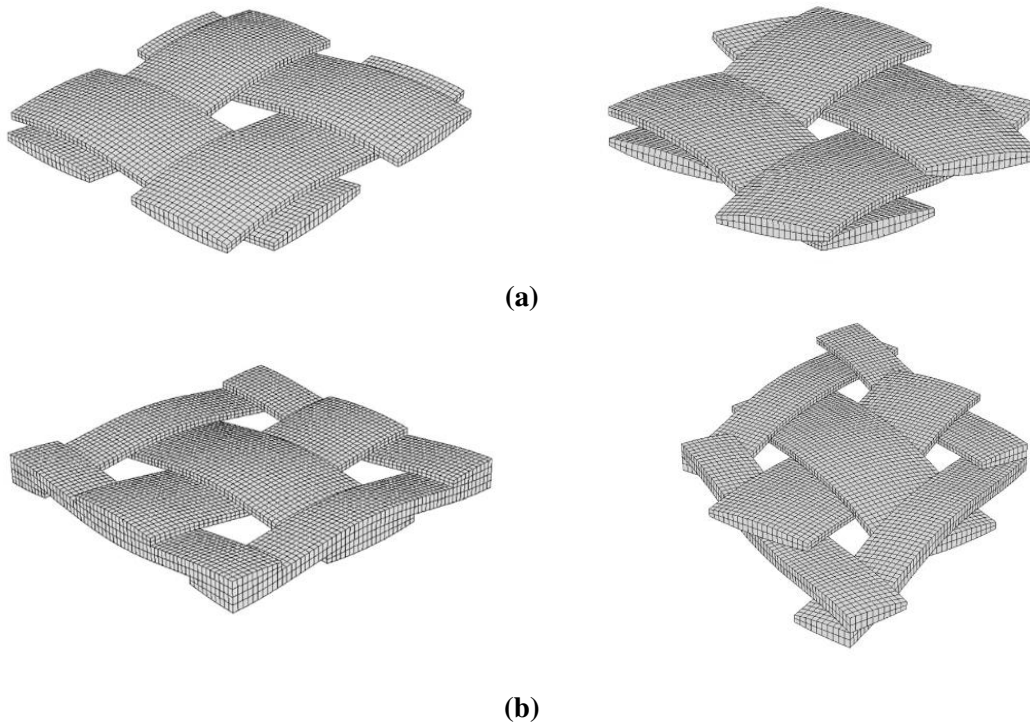


**Figure 1.23** – Two types of RUCs for a plain weave fabric and their deformed shapes [BAD 07b].

### 1.4.3 Simulation models at the macroscopic scale

#### 1.4.3.1 Continuous approaches

The continuous approach considers the fibrous reinforcement or prepreg as a continuum. As seen in the preceding sections, the reinforcement is not continuous at lower scales, but a continuous material can be supposed to superimpose on the fibrous material. This needs the assumption that there is no significant sliding between fibers and yarns in the deformation. Several experiments have already proved this assumption. For instance, Boisse et al [BOI 95] have done a forming experiment for woven fabric on a hemispherical (Figure 1.24). A set of lines following the warp and weft yarn directions were drawn on the fabric before forming. These lines became curved after forming but remained continuous, which implies that, due to the weaving, there was no large sliding between warp and weft yarns. The advantage of the continuous approach is that it can be implemented in commercial FE codes, although the constitutive model of the continuum will have to include the very specific mechanical behaviour of the fibrous reinforcement, especially this behaviour is mainly depending on the fiber directions that are changing during forming. Most of the proposed continuous approaches for FE forming simulations are based on hypo-elastic and hyper-elastic approaches. This permits to develop the models in user subroutine such as VUMAT in ABAQUS/Explicit.

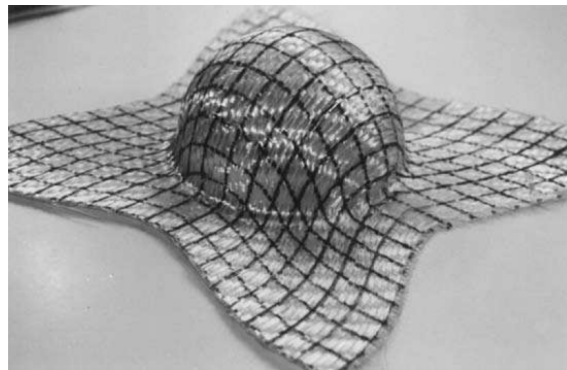


**Figure 1.24** – Validation of no sliding assumption between yarns in the forming [BOI 95].

In hypo-elastic approach, a rotation is used to define an objective derivative for the hypo-elastic constitutive law and to update the orthotropic frame. The rotations used in Green-Naghdi and Jaumann derivatives are the average rotations of the material. Consequently, these approaches can't be used for fibrous materials under large strains because the update of material direction must follow the fiber direction accurately. To overcome this problem, the non-orthogonal constitutive models were proposed by Yu et al [YU 02] and Peng et al [PEN 05]. In the non-orthogonal constitutive models, the stress and strain were related using the constitutive relation in a non-orthogonal frame defined by the fiber orientations. The fiber direction was updated from the deformation gradient tensor which makes sure to follow the correct material directions. The non-orthogonal constitutive models can be used to simulate large strains for fibrous materials.

Another type of continuous approach is called hyper-elastic approach. The starting point is an elastic potential (internal energy) given as a function of right Cauchy-Green deformation tensor. For 2D fabrics, the hyper-elastic potential is constructed by three terms (supposedly decoupled): two tension energies in two yarn directions and one in-plane shear energy [HOL 00, AIM 08, PEN 13]. The tension and in-plane shear tests on woven reinforcements are used to identify the various terms of proposed potential function. For 3D interlock fabrics, the hyper-elastic potential energy is assumed to be composed of six parts: two tension energies in two yarn directions, one in-plane shearing energy, one transverse compression energy in thickness direction and two transverse shearing energies in two yarn's directions [CHA 12].

#### 1.4.3.2 Discrete approaches

The discrete approach considers and models the components of fibrous reinforcement at lower scale. These components can be yarns or representative unit cells. Since these components are usually at the mesoscopic scale, this approach is also known as meso-mechanical modelling. In the discrete approach, the discrete models of fabrics are based on modelling yarns usually by elements such as beam or solid elements. A meso-mechanical modelling of the biaxial NCF that is composed of two separate ply layers has

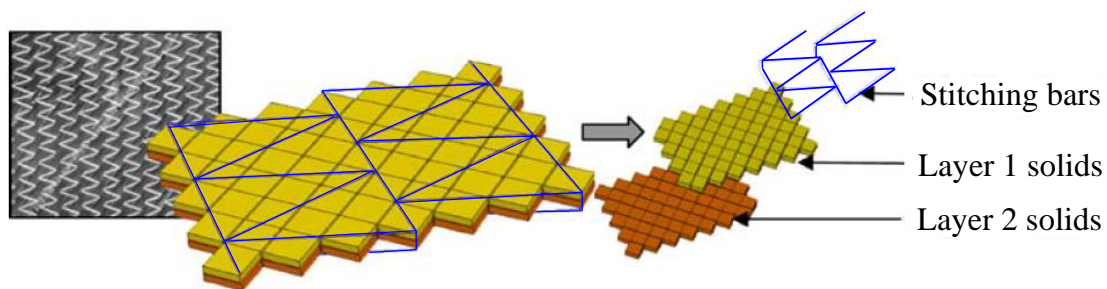


**Figure 1.25** – A representative cell of the meso-mechanical model for NCF [CRE 06].

been proposed by Creech et Pickett [CRE 06]. 3D solid elements were used to discretize the yarns and interconnecting bar elements were used to approximate the stitching (Figure 1.25). Contact and frictional sliding between yarns and stitches were treated using an appropriate contact algorithm and additional stitch-to-yarn connection elements. Although the complete model needs very cost computational time, a forming process was simulated in this way. It shows this modeling method can capture the main mesoscopic fabric deformation mechanisms.

#### 1.4.3.3 Semi-discrete approaches

The semi-discrete approach is a compromise between the continuous and discrete approaches. Specific finite elements are constructed, which are made of a discrete number of yarns or woven representative unit cells. Hamila and Boisse [HAM 09] proposed a

semi-discrete triangular shell finite element which was composed of unit cells. These unit cells were subjected to tension, in-plane shearing and bending. The deformations of the representative unit cell were calculated from element interpolation. A semi-discrete solid element made of yarn segments for simulating 3D interlock was proposed by De Luycker [LUY 09]. The yarns were only accounting for the tension energy of fabric, other parts of energy were considered in the solid element. The forming simulation results with the above two types of elements are shown in Figure 1.26.

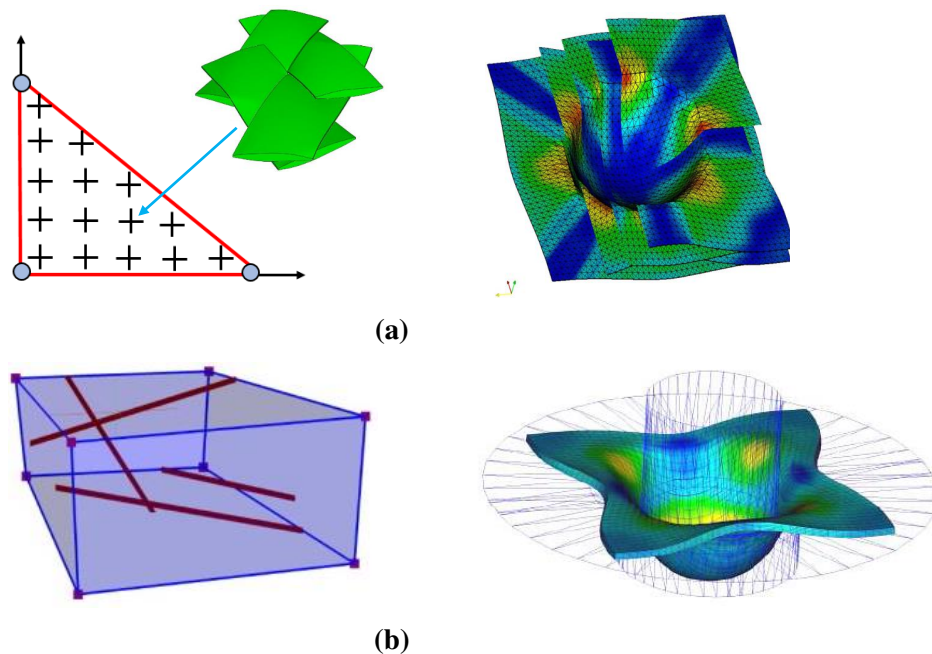


**Figure 1.26** – Schematic of semi-discrete elements and their forming simulations. (a) Shell element [HAM 08]. (b) Solid element [LUY 09].

## 1.5 Motivation and objectives

This thesis aims to investigate the bending deformation behaviour of textile reinforcements and thermoplastic prepregs by the experimental and numerical methods, the primary objectives can be divided into two aspects:

- To develop an experimental method to measure the bending stiffness for thermoplastic prepregs at elevated temperatures (of course it can be applied for dry textile reinforcement).
- To develop a specific shell element that can be capable of simulating the bending deformation of thick fibrous materials, such as laminated reinforcement and interlock.

## 1.6 Thesis summary

The following summaries the contents of this thesis:

Chapter 2 : Bending behaviour characterization for thermoplastic preregs at the manufacturing temperature

*This chapter describes an improved cantilever bending test method for thermoplastic preregs. Descriptions of the principle of this bending test method and its set-up are presented. A sets of bending tests are carried out for three types of interested thermoplastic preregs at various high temperatures. To investigate the influence of bending stiffness on the forming simulation results, particularly to the wrinkles, simulations have been done with the measured bending stiffness.*

Chapter 3 : Specific plane shell finite element for simulating the bending deformation of thick fibrous materials

*This chapter first presents the specialties of the bending deformation behaviors of thick fibrous materials, then a specific plane shell finite element that is able to simulate the bending deformation of thick fibrous materials is presented. Following this, several bending deformation simulations have been performed for different thick fibrous materials and are compared with corresponding experimental results to validate the efficiency of the proposed element.*

Chapter 4 : Conclusions and perspectives

*This chapter presents the key outcomes of this work and major conclusions, and several recommendations for the future work are made.*



## Chapter 2

# Bending stiffness characterization for thermoplastic prepregs at the manufacturing temperature

### 2.1 Introduction

Continuous fiber reinforced thermoplastics (CFRTP) are widely used in aerospace and automobile industries because of their low density but high stiffness and strength. In the purpose of high volume production, many thermoforming techniques such as compression forming, vacuum forming and resin transfer molding have been developed for thermoplastic composites in the last two decades. Among them, thermo-stamping has drawn much attention since it offers an automated and rapid option for mass production of composite part with complex geometry. Unlike thermosets, which undergo a chemical curing reaction for geometry stabilization during forming, the forming process for CFRTP is relatively simple and involves only physical changes to the material. Essentially, the matrix is melted by heating, the part shape is formed and finally, the geometry is obtained by cooling [CAM 03, HUS 06, BAL 13].

CFRTP components are typically thin-walled and made primarily by forming layered pre-consolidated laminate or powder impregnated prepregs through thermoforming. This process is very complex because many thermal and mechanical factors would affect the state of final composite part. Defects are very easy to appear. CFRTP tend to suffer from the wrinkling and fiber buckling due to the property mismatch between fibers and viscous resins in the forming. In the cooling stage, warp due to the buildup of the thermal residual stress may cause dimensional deviations of products from the desired shape. Therefore, to avoid the time and cost expensive trial-error approaches, numerical simulation of the forming process is very necessary and helps to optimize the process conditions. The modeling of each prepreg ply is usually made by a set of shell finite elements in frictional contact with its neighbor layers. These F.E. simulation codes require the knowledge of the prepreg ply mechanical behavior and of the tool-ply and ply-ply friction at the forming temperature [WAN 13, HAA 14b]. The recommended forming temperature is usually

slightly above the melting temperature of resin. Nevertheless it can vary within the composites because of heat transfers to and from the tools. These temperature variations are important because they can significantly modify the mechanical behavior of the prepreg ply and can even lead to defects. Therefore, the mechanical properties during forming must be known for a fairly wide range of temperatures. The in-plane shear behavior is the most important mechanical property during thermoforming on double curved shapes. The bias extension test and picture frame test are generally used to measure the in-plane shear properties [WAN 14, GUZ 15]. The tensile stiffness is large and mainly depends on fibers and therefore is little affected by the temperature. Bending properties are also required when using a F.E. approach based on shell elements. Bending stiffness conditions the geometry of the computed wrinkles [BOI 11, LIA 14, LIA 15]. Wrinkling phenomena is frequent due to the fibrous internal structure of reinforcements, in which fiber can easily slide to each other in the deformation. Bending stiffness must be taken into account in order to verify the wrinkles do not extend to the useful zones of the manufactured composite part in the forming simulation.

Moreover, it has been known that bending stiffness of prepreg is not directly related to its in-plane tensile modulus as the conventional continuous material structure due to the relative sliding between fibers and is also temperature dependent, therefore, it's necessary to measure its value by the experimental method. Yu et al [YU 05] compared the bending behaviour of a woven preform through a cantilever experiment and simulation where the deflection was only due to gravity. The authors showed the discrepancy between the experimental and numerical results and concluded that bending rigidity derived from in-plane tensile properties gives an unrealistically high value compared to the experimental bending rigidity of the woven preform.

Based on above, one of the main objectives of this thesis is to propose an experimental method to measure the bending stiffness of thermoplastic prepregs. To this aim, an improved cantilever bending test at elevated temperature using optical measurements has been designed. The sample can be either single ply prepreg or laminate.

## 2.2 Review of the related works

Although some test methods originally developed at room temperature can be easily developed into use at high temperature with the help of environmental chamber, such as bias extension test. However, this is not true for the transformation of conventional bending set-ups used at room temperature to high temperature. An overview of the main test methods developed to measure bending properties of dry reinforcement and thermoplastic composites would be given in the following.

### 2.2.1 Bending stiffness characterization for dry reinforcement

Two standard tests are commonly used for evaluating fabric bending stiffness: the standard cantilever test [STA 04] and the Kawabata bending test (KES-FB2) [KAW 80]. The

first one is based on elastic linear bending behaviour and enables the determination of only one parameter: the bending rigidity. The second test was designed by Kawabata and enables one to record moment versus curvature during a bending load cycle.

Peirce was the first to present a macroscopic measurement of fabric bending behaviour [PEI 30]. In Peirce's bending model an elastic linear behaviour between bending moment  $M$  and curvature  $\chi$  of the strip was assumed:

$$M = B \cdot b \cdot \chi \quad (2.1)$$

Where  $B(\text{N} \cdot \text{m})$  is bending stiffness per unit width and  $b(\text{m})$  is the width of strip. Such model assumes small bending deflection and the fibrous material is a uniform elastic thin lamina at the macroscopic scale. Peirce defined the ratio  $S$  of the flexural stiffness to the weight per unit area of strip  $w(\text{N} \cdot \text{m}^{-2})$ :

$$S = \frac{B}{w} \quad (2.2)$$

With this relation, and conditions of equilibrium of forces and bending moments, and the linear relation between moment and curvature, Peirce obtained the expression for bending stiffness [SYE 12]:

$$B = S \cdot w = \frac{l^3 \cos(\phi/2)}{8 \tan \phi} \cdot w \quad (2.3)$$

Where  $l$  is the length of bent part the strip (or called bending length)(m), and  $\phi$  is the deflection angle between the chord and horizontal axis (see in Figure 2.1). The limitation of the model by Peirce is that it assumes small bending deflection and describes only linear elastic bending behavior.

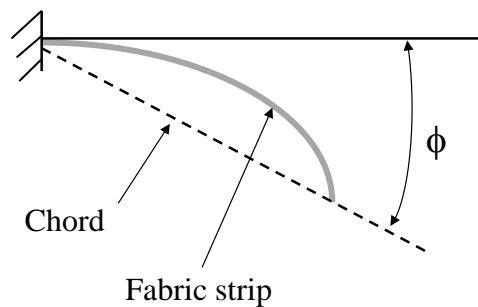


**Figure 2.1** – Schematic representation of Peirce's cantilever bending test [PEI 30].

Abbott et al [ABB 51] studied the influence of bending length of the strip and the deflection angle in equation (2.3) on the bending stiffness of fabric. It has found that a  $40^\circ \sim 50^\circ$  deflection angle would give a stable bending stiffness. This fact prompted the simplification of the procedure of Peirce's test so that deflection angle becomes fixed, what needs to determine is only the bending length. The standard commercial bending test devices (ASTM) in use today are based on the deflection angle equal to  $41.5^\circ$ . With this value, the equation (2.3) can be written in a more simple form:

## 2. Bending stiffness characterization for thermoplastic prepregs at the manufacturing temperature

$$B = \frac{l^3 \cos(41.5^\circ/2)}{8 \tan 41.5^\circ} \cdot w \approx \frac{l^3}{8} \cdot w \quad (2.4)$$

The standard cantilever bending test (ASTM) involves a rectangular strip of fabric on a horizontal board being pushed slowly forward until the tip of the strip touches a titled board with an inclined angle of  $41.5^\circ$  to the horizontal (Figure 2.2). Then the bending length is measured and the bending stiffness is calculated with equation (2.4). Performing a standard cantilever bending test is thus very easy but only the bending stiffness of the linear elastic bending model can be identified.

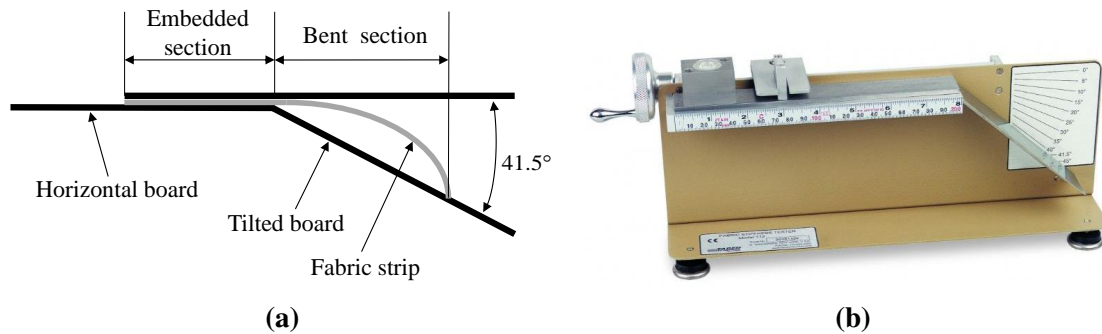


**Figure 2.2** – Standard cantilever bending tester. (a) Schematics. (b) Configuration [STA 04].

Kawabata's Evaluation System was originally designed to measure basic mechanical properties of fabrics [KAW 80]. It has become a set of tests commercially available for tensile, shear, compression, surface roughness and bending behaviour. KES-FB2 tester enables to record directly the evolution of bending moment versus curvature during a load-unload cycle. The sample is clamped between a fixed and movable clamp (Figure 2.3a). During the test, the movable clamp rotates around the fixed clamp to impose a pure bending on the sample. Figure 2.3b shows a typical result of the KES-FB2 bending test carried out on a 2.5D carbon fabric in the weft direction. The bending behaviour is not linear. The hysteresis phenomenon can be observed during loading/unloading. This is due to the dissipation of friction between fibers. Some macroscopic models taken into account the influence of friction were developed based on KES-FB2 bending test results, like the Grosberg model [GRO 66] and Dahl model [DAH 76]. Despite the KES-FB2 bending tester is able to test and show the non-linear and hysteresis bending behavior of fabrics, it has been originally designed for thin clothing textiles and is not well adapted for textile reinforcements, particularly for thick or multi-ply reinforcements. Furthermore, the working principles and set-up are relatively delicate and expensive, limiting its application and availability.

DeBilbao et al [DEB 10] developed a bending test device called flexometer based on the cantilever principle. It has been developed with the aim of characterizing the non-linear bending properties for stiff and multi-ply textile reinforcements. This device was made up of two parts: mechanical module and optical module (Figure 2.4). The mechanical

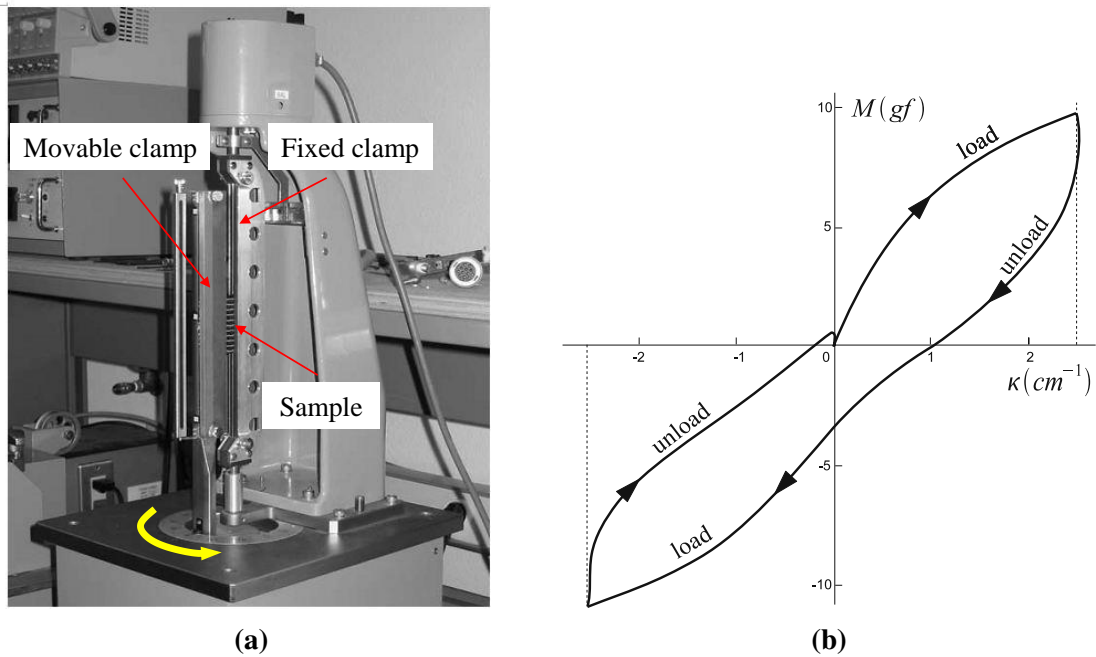


**Figure 2.3** – KES-FB2 bending tester [DEB 10]. (a) The Configuration. (b) Bending test results.

module enabled one to place the specimen in a cantilever configuration under its own weight. The optical module took the picture of the bent shape of sample. The bending

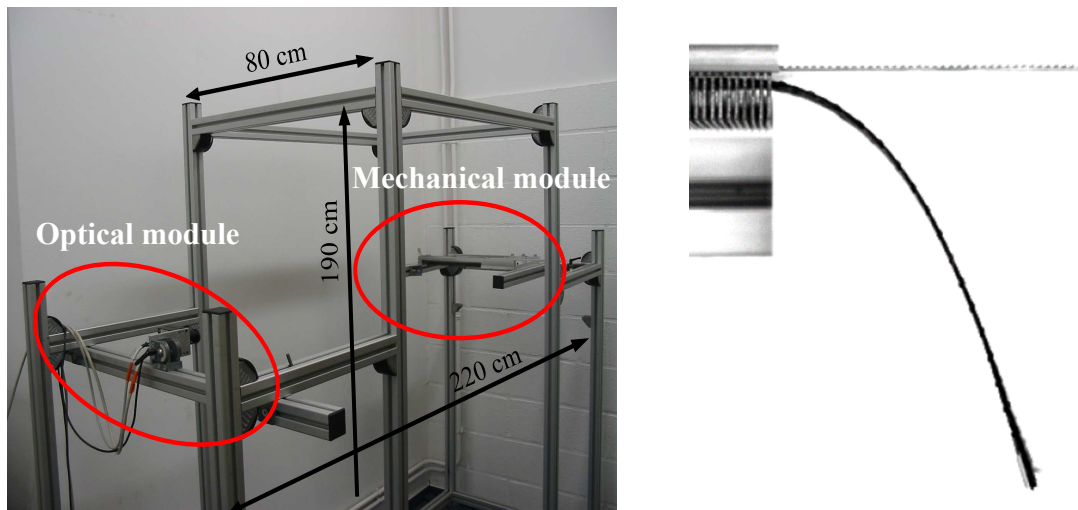


**Figure 2.4** – The configuration of flexometer proposed by De Bilbao [DEB 10].

moment and curvature can be computed along the midline of bent shape and moment-curvature graph can be drawn (Figure 2.5). However, from Figure 2.5, it can be observed there are many undulations for the moment-curvature curve and this undulation also exists

## 2. Bending stiffness characterization for thermoplastic prepregs at the manufacturing temperature

---

in his other bending test results. One possible reason is the fitting curve that the author used to fit the midline in the curvature calculation is not smooth enough.

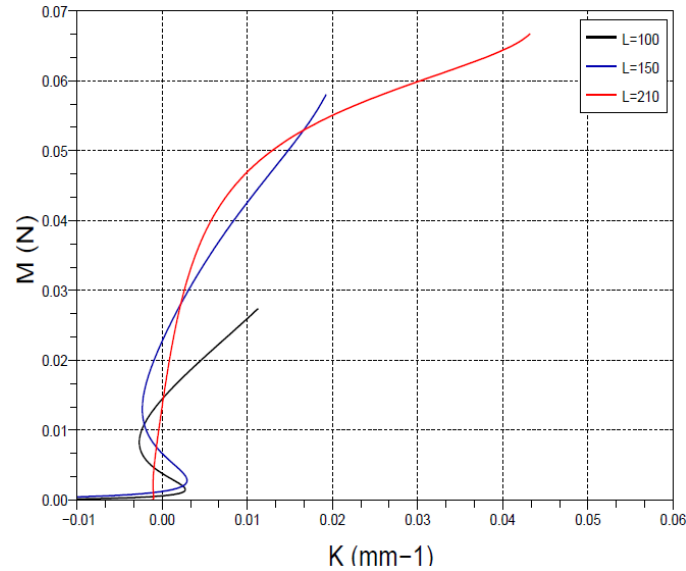


**Figure 2.5** – Bending test results of reinforcement with different bending length from flexmeter [DEB 10].

Soteropoulos et al [SOT 11] proposed vertical cantilever bending test method by rotating the horizontal cantilever experiment  $90^\circ$  to measure the bending behaviour of dry fabric (Figure 2.6). Using a pulley, mass was added to apply horizontal force to deform the sample. A picture was taken for the deformed profile. Bending moment and curvature were calculated from the bent profile as that done in [DEB 10], the slope of moment-curvature curve was the bending stiffness. The main advantage of vertical cantilever bending compared with horizontal cantilever bending is that it can control the rate of applied load, but the main disadvantage is it assumes the load imposed by the mass remains in the horizontal direction after deformation, which is only valid for small bending deflection. Consequently, this method can only be used to measure small bending deformation.

### 2.2.2 Bending stiffness characterization for thermoplastic composites

In characterizing the bending behaviour for thermoplastic composites, there are few studies. The bending behaviour of thermoplastic composites is temperature dependent, to have a knowledge about their bending stiffness, it needs to carry out tests at various temperatures.

Wang et al [WAN 08] proposed an experimental measurement on the bending of UD prepregs by means of a large displacement buckling test at various displacement rates and temperatures. In this test method, the bending behaviour was expressed as the axial force

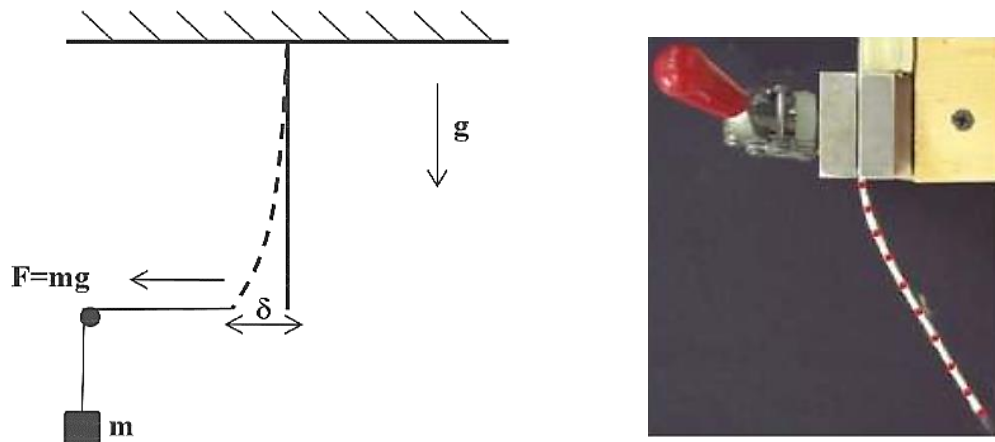


**Figure 2.6** – Vertical cantilever test for the evaluation of bending stiffness [SOT 11].

versus the displacement parallel to the applied force. Specimens were cut into a rectangular shape comprised of testing and clamped regions. The experimental setup is shown in Figure 2.7. The set-up consists of a specimen, upper and lower clamps. During testing, the lower clamp was fixed, while the upper clamp was attached to a load cell mounted on the crosshead. The upper clamp moved downwards until a prescribed displacement was reached. The main advantage of this method is the set-up's simplicity and it's relatively easy to investigate the rate and temperature dependence compared with the standard cantilever and KES-FB2, but the main challenges are the asymmetric bending shape and wrinkles would very easily occur in the compression, which can greatly influence the final experimental results. Furthermore, the interpretation of buckling curves is complicated.

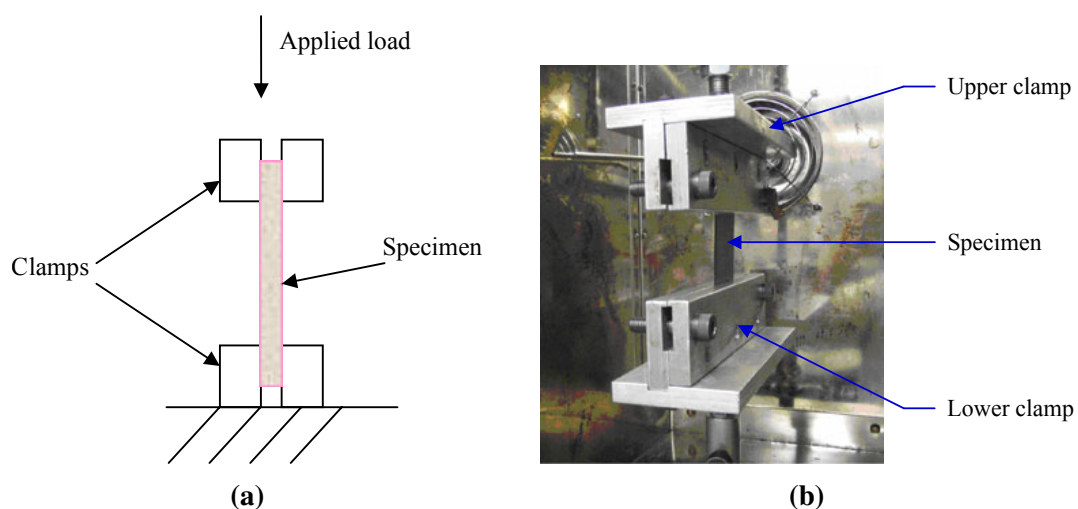


**Figure 2.7** – Buckling bending test proposed by Wang [WAN 08]. (a) Layout of a buckling test. (b) Photograph of experimental setup.

Another bending characterization set-up for thermoplastic composites was developed

## 2. Bending stiffness characterization for thermoplastic prepregs at the manufacturing temperature

---

by U. Sachs et al [SAC 14]. It was installed in a rheometer with thermal chamber (Figure 2.8). The rheometre was an oscillating rotational machine which offers a precise rotation angle and rotation velocity control. A thin rectangular specimen was bent by the rotation of the upper shaft. The applied moment was measured under each rotation angle. The principle of this set up is very analogous to the KES-FB2 bending tester. The main difficulty of this device is to ensure pure bending throughout the specimen. Consequently, the sample size should be as small as possible, but this would result in the required hypothesis of macroscopic characterization are not satisfied as the specimen dimension diminishes to the characteristic dimension of yarn. Besides, the testing results strongly depend on the boundary conditions set by the clamps that don't hold tight the specimen in the test, these aspects make it not very easy to operate and have good repeatability.

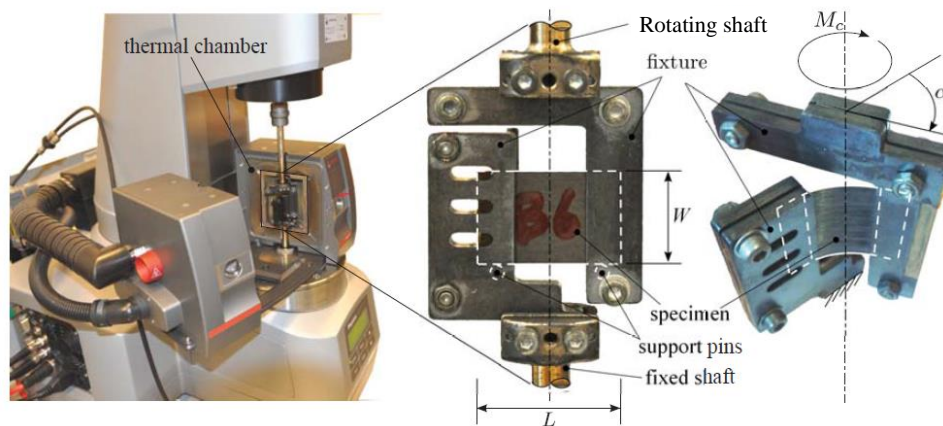


**Figure 2.8** – Experimental bending test device proposed by U. Sachs [SAC 14].

Recently, A. Margossian et al [MAR 15] have developed a bending test method to measure the bending stiffness for UD thermoplastic composites. A DMA (dynamic mechanical analysis) system was used in his work to implement three-points bending or cantilever bending. With the help of DMA machine, the influence of deformation rate on the bending stiffness can be investigated. However, in this method, bending stiffness of UD prepregs is seen as constant and its accuracy is greatly dependent on the measuring precision of sample's thickness, which raises a challenge to get a good repeatability for the test results.

## 2.3 An improved cantilever bending test approach for thermoplastic prepregs

### 2.3.1 Basic ideas of the bending test approach

In this thesis, one objective is to develop a method to measure the bending stiffness for thermoplastic prepregs at elevated temperature. The cantilever principle has been kept to

develop the bending test approach because of its simplicity and flexibility in the test. The schematic of the improved cantilever bending test approach is shown in Figure 2.9. In the test, image of the bending deflection shape is taken by a high resolution camera and is processed to extract its midline; then bending moment and curvature are calculated along the midline; finally a moment-curvature curve is obtained and the slope of the moment-curvature curve is the bending stiffness of sample. Compared with the available bending test methods, this bending test approach is easy to operate at high temperature and the set-up is simple. It allows to measure large enough bending deformation and to get a wide range of moment-curvature relation. Besides, the test results have a clear physical meaning and are easy to understand.

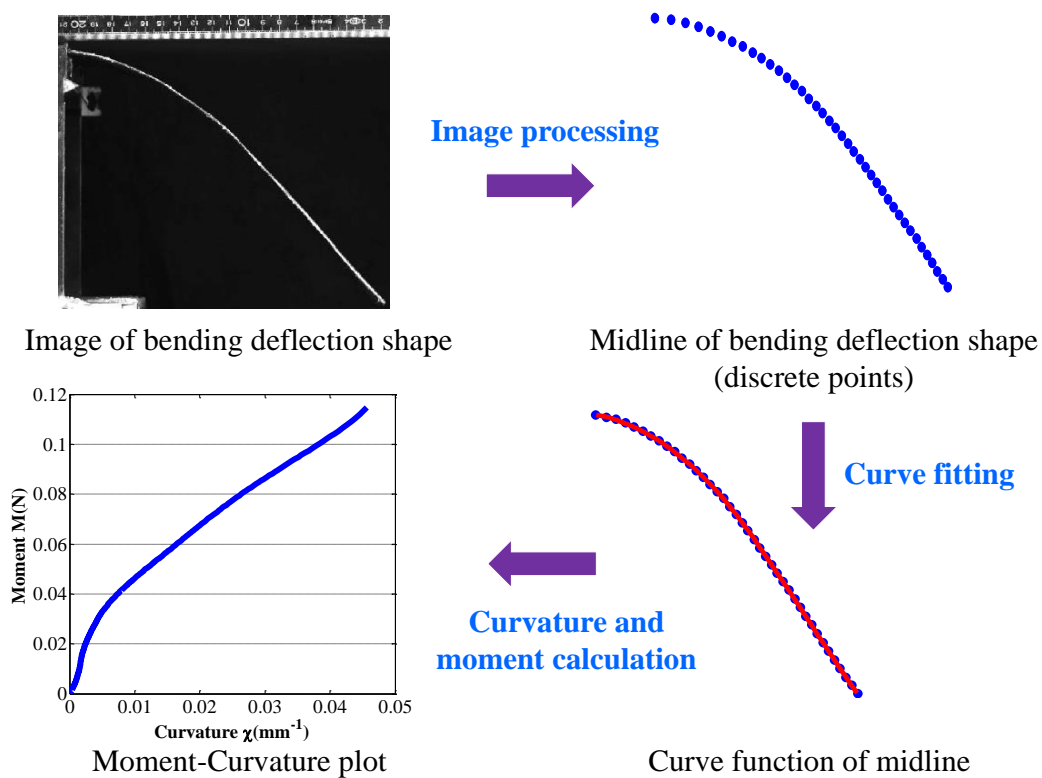


**Figure 2.9** – Schemtaic of proposed bending test approach.

### 2.3.2 Set-up description and general test procedure

A metallic support is used to clamp the specimen and make it deform in a cantilever form. Both the support and specimen are placed in a thermal environmental chamber (Figure 2.10). The temperature can be set from 20 to 600 °C. A CCD camera associated with acquisition software, takes the picture of the deformed specimen through the transparent door of chamber (Figure 2.11). The specimen is lit by two adjustable LED lamps. A ruler is put on the same plane as the leading edge of sample and latter would be used to compute the scaling factor in the image processing (Figure2.10). The sample's cross-section

## 2. Bending stiffness characterization for thermoplastic prepregs at the manufacturing temperature

is painted white with some dry white powders to increase contrast with background (background is black) to facilitate extracting the midline in the image processing (Figure 2.11).

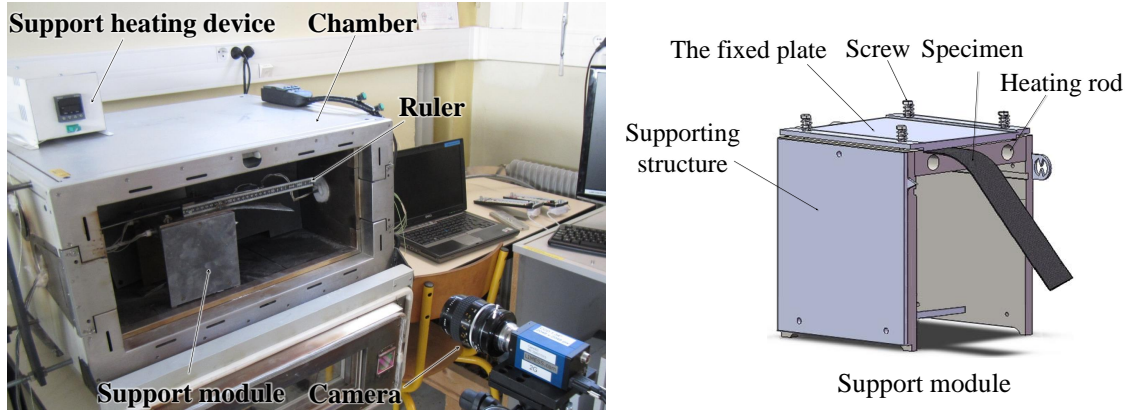


**Figure 2.10** – Bending test set-up configuration.

The specimen is placed on the support at room temperature, this gives the first deflection shape at room temperature ( $25^{\circ}\text{C}$ ). Then the specimen is heated to a higher temperature. When the desired high temperature is reached in a homogeneous state within the sample, it generally needs another 2 or 3 minutes to stabilize this isothermal state before taking pictures. The bending deflection shape is acquired by the CCD camera. This method is iterated to obtain deflection shapes corresponding to different higher temperatures. The deformation rate is slow and the measured bending properties are those of quasi-static tests. The influence of deformation rate on the bending stiffness is not considered in the present work. The influence of deformation rate has been shown to

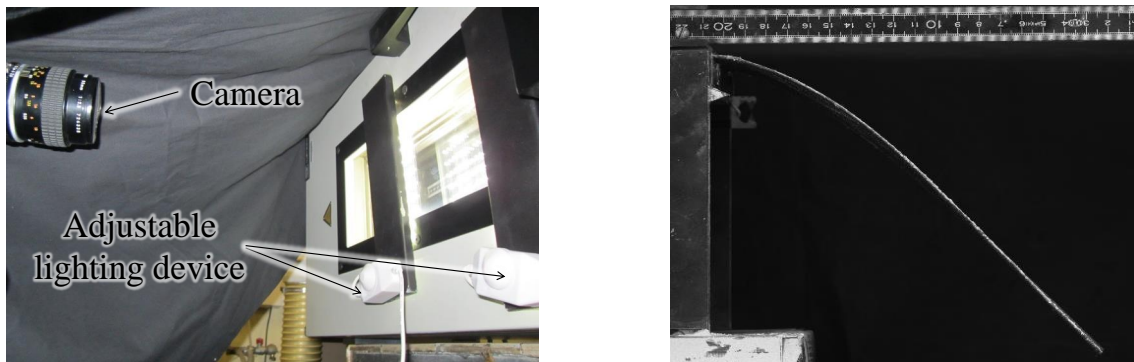


**Figure 2.11** – Optical measure and lighting with two LED lamps.

be much less important than the influence of temperature in-plane shear tests [WAN 14]. Nevertheless, the duration of the test must be controlled and limited because the matrix risks non-negligible oxidation if it is left too long in the chamber. This oxidation is more serious at higher temperatures. The oxidation issue could be solved by conducting tests in a nitrogen environment.

### 2.3.3 Temperature analysis in the bending test

The temperature distribution throughout the specimen should be as uniform as possible. In order to measure the temperature field, six thermocouples are placed at different positions near the prepreg strip. The thermocouples are marked with color circles as shown in Figure 2.12a. The orange thermocouple (TC1) is placed in the clamping zone of sample (more accurately it's in the interior of sample). Several modifications are necessary to obtain a homogeneous temperature field. Firstly, the support has a large thermal inertia and therefore temperature measured by the thermocouple TC1 was notably smaller than others. Consequently, adding a specific heating system to the support has proven indispensable (Figure 2.10). Secondly, a modification in the air flux of the chamber was needed. This chamber had been originally designed to be used vertically. This air flux modification enabled an improvement of the temperature field in the horizontal position. The temperatures measured with the modifications described above were correctly homogeneous ( $\pm 5^\circ\text{C}$ ) in the 20–600°C range (Figure 2.12b).

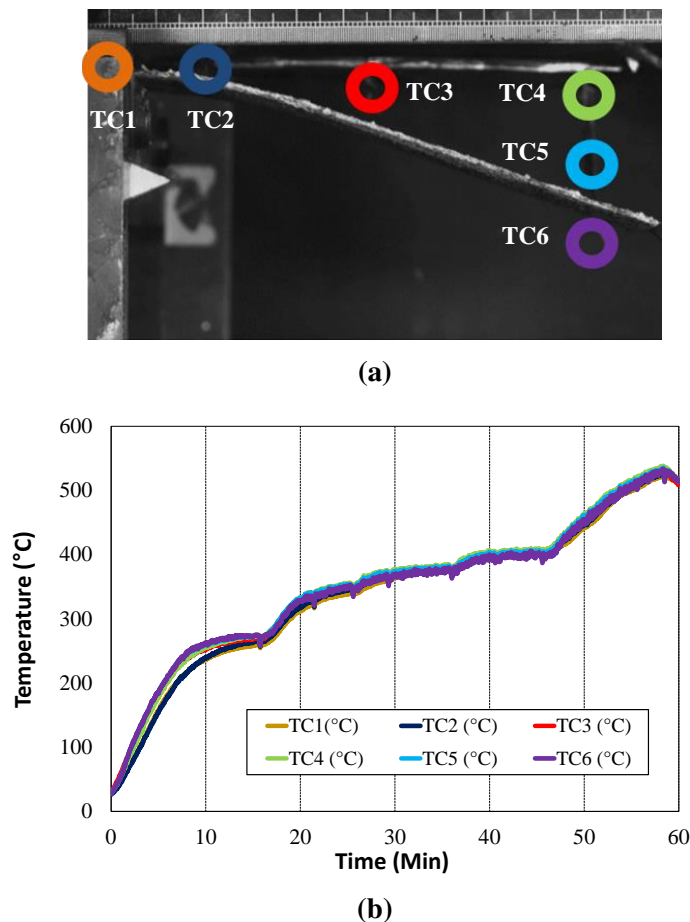


**Figure 2.12** – (a) Positions of thermocouples. (b) Temperature measurements at different instructions.

### 2.3.4 Image processing of the bending deflection shape

#### 2.3.4.1 Image pre-processing

Image of bending deflection shape should be pre-processed to remove noise and enhance its prominence prior to extract its midline. ImageJ can be used for that purpose, although any other image processing software would work just as well. The image pre-processing mainly contains four steps: smoothing, contrast enhancement, thresholding and shape smoothing. All these steps can be implemented in ImageJ. Smoothing reduces the noise levels in the image. It's particularly important for noisy images as it effectively averages out background noise to an enough low level. Gaussian blur filter has been chosen to work as smoothing the image. Contrast enhancement optimizes the signal-to-noise ratio and normalizes the signal for processing and visualization. Thresholding works by separating pixels which fall within a desired range of intensity values from those which do not (also known as 'segmentation'). By thresholding, it can group the regions that have a similar pixel value and separate them from each other. Care should be taken when adjusting threshold values to ensure that artificial gaps or branches are minimized (Figure 2.13).

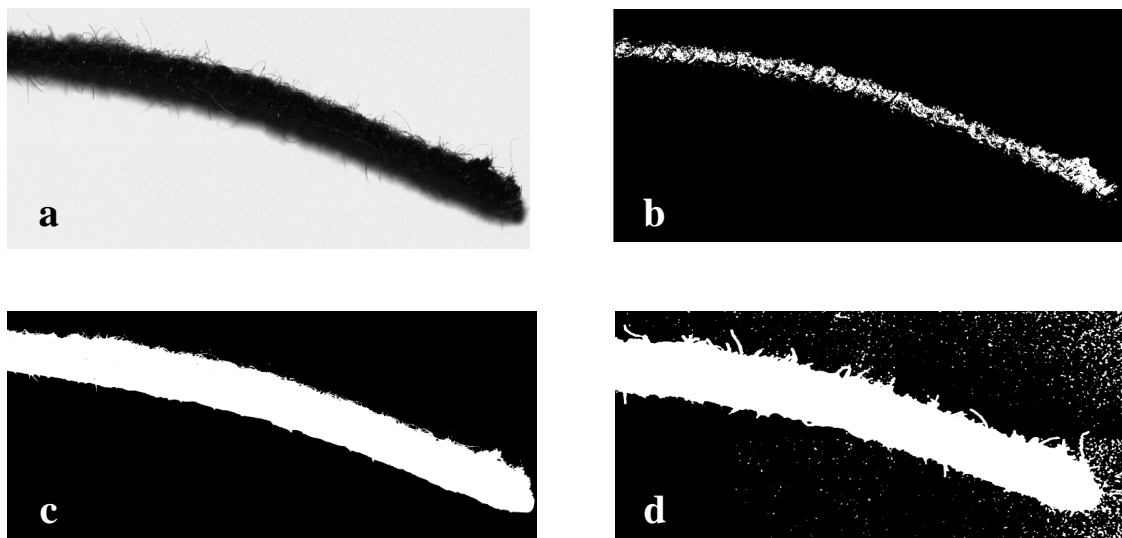


**Figure 2.13** – The effect of thresholding. (a) Original image. (b) Too high thresholding. (c) Proper thresholding. (d) Too low thresholding.

After the thresholding operation, the bending deflection shape of sample can be isolated from other parts. Unfortunately, the shape would inevitably still contain the noise. Shape smoothing needs to be carried out to make the deflection shape as smooth as possible. Figure 2.14 shows a comparison of noisy shape before and after shape smoothing. A notable improvement on the shape's smooth can be observed. Throughout pre-processing, it is important to compare the processed image with the original after each processing step, such crosschecking allows for immediate correction of processing artifacts that may arise.



**Figure 2.14** – Shape smoothing. (a) Noisy shape. (b) Noisy shape after shape smoothing.

### 2.3.4.2 Midline extraction

To extract the midline of bending deflection shape, skeletonization is adopted. The skeleton of a shape is a thin version of that shape which is equidistant to its boundaries. There are four requirements must be satisfied for the skeleton of an object [BOR 99]:

- **Centeredness satisfaction:** Skeleton is geometrically centered within the object boundary or as close as possible
- **Connectivity preservation:** The output skeleton should have the same connectivity as the original object and should not contain any background element
- **Topology must remain constant**
- **As thin as possible:** 1 pixel thin is the requirement for a 2D skeleton, and in 3D as thin as possible

There are two categories of skeletonization methods. One category is based on distance transforms and another is defined by thinning approaches. The plugin in ImageJ uses the thinning approaches to perform the skeletonization. Figure 2.15 presents one skeletonization example (red line is the skeleton of a shape). With skeletonization, a set of discrete points located on the center of bending deformation shape can be obtained. With the scaling factor, the pixel coordinates of these points can be transformed into real physical Cartesian coordinates. The curve that these discrete points represent is the midline of bending deflection shape. Alternatively, this midline is also called deflection curve.

### 2.3.5 Curvature calculation

Despite the midline information of sample comes from the high resolution camera, measurement errors are unavoidable. Furthermore, some errors can also be introduced in the image processing. These factors result in the midline (or deflection curve) contains some errors more or less. Consequently, to calculate midline's curvature, it's better to use a curve function to fit the midline and then calculate the curvature from the fitting curve to characterize midline's curvature. It is necessary to define what kind of curve function

## 2. Bending stiffness characterization for thermoplastic prepregs at the manufacturing temperature

---

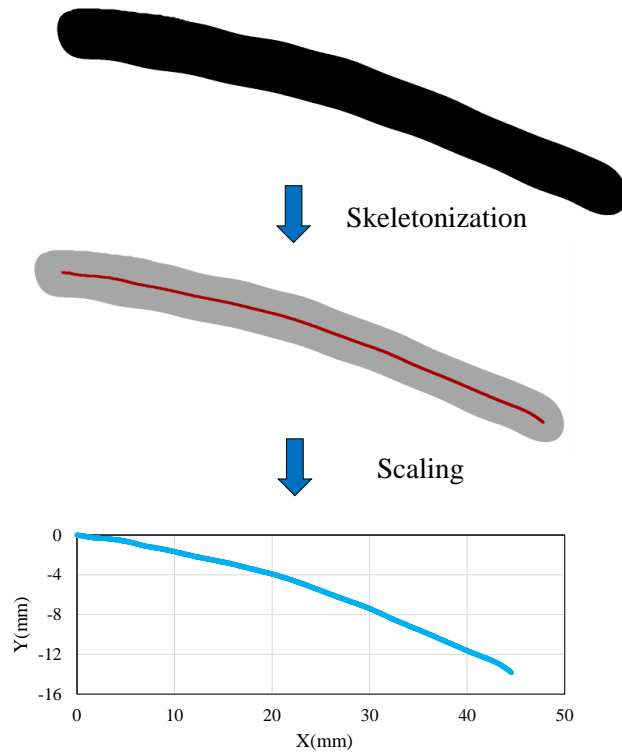


**Figure 2.15** – Skeletonization and midline plotting.

should be chosen to fit the midline. Single polynomial curve function can be used, but generally it needs to be very high order in order to have a good fitting accuracy, which is easy to cause some unnecessary oscillations. According to the experimental observation, it's found that the bending deflection shape of continuous fiber reinforcement is usually composed of more than one curve shape. This point is also verified in the literature [GRI 96]. Consequently, a piecewise curve function should be used. In this thesis, uniform quartic B-spline curve is chosen to fit the midline since it's a piecewise curve and it has a good fairness. Fairness is a term primarily related to the smoothness of geometry shape. According to the literature [FAR 89], one important fairness criteria for a curve is to check its slope discontinuity of curvature plot. For a given curve, we can plot its curvature versus its arc length and thus obtain the curvature plot of the curve. If there is no or very less slope discontinuity of curvature plot, it's said that the curve has good fairness.

### 2.3.5.1 Uniform quartic B-spline curve

Uniform quartic B-spline curve is a piecewise polynomial curve and composed of more than one segment and each segment is a quartic B-spline. Figure 2.16 is an example of uniform quartic B-spline curve. It's made up of  $m$  segments 1, 2  $\dots$   $m$ , with  $\mathbf{D}_{i-1}$  and  $\mathbf{D}_i$  being the start and end points of  $i$ th segment. The position vector of a point  $P$  lies on the  $i$ th segment can be written in terms of its local function form:

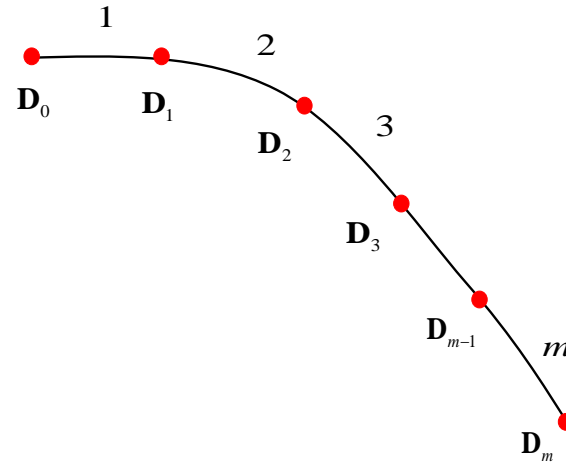


**Figure 2.16** – Example of uniform quartic B-spline curve.

$$\mathbf{C}_i(u^{(i)}) = (X(u^{(i)}), Y(u^{(i)})) = \sum_{k=0}^4 M_{k,4}(u^{(i)}) \mathbf{B}_{i+k-1} \quad (2.5)$$

Where  $X$  and  $Y$  are the cartesian coordinates,  $u^{(i)}$  is the local parameter value of point  $P$  varying from 0 to 1 along the  $i$ th segment,  $\mathbf{B}_{i+k-1}$  are the control points,  $M_{k,4}$  are the basis functions of quartic B-spline:

$$M_{k,4}(u^{(i)}) = \begin{cases} \frac{1}{24}(u^{(i)})^4 - \frac{1}{6}(u^{(i)})^3 + \frac{1}{4}(u^{(i)})^2 - \frac{1}{6}(u^{(i)}) + \frac{1}{24}; & k = 0 \\ -\frac{1}{6}(u^{(i)})^4 + \frac{1}{2}(u^{(i)})^3 - \frac{1}{4}(u^{(i)})^2 - \frac{1}{2}(u^{(i)}) + \frac{11}{24}; & k = 1 \\ \frac{1}{4}(u^{(i)})^4 - \frac{1}{2}(u^{(i)})^3 - \frac{1}{4}(u^{(i)})^2 + \frac{1}{2}(u^{(i)}) + \frac{11}{24}; & k = 2 \\ -\frac{1}{6}(u^{(i)})^4 + \frac{1}{6}(u^{(i)})^3 + \frac{1}{4}(u^{(i)})^2 + \frac{1}{6}(u^{(i)}) + \frac{1}{24}; & k = 3 \\ \frac{1}{24}(u^{(i)})^4; & k = 4 \end{cases} \quad (2.6)$$

A global function form can be written to express the position vector for point  $P$  based on its local function form that in Equation (2.5):

$$\mathbf{C}(t) = \mathbf{C}_i(u^{(i)}) = (X(t), Y(t)) = \sum_{h=0}^{m+3} N_{h,4}(t) \mathbf{B}_h \quad (2.7)$$

## 2. Bending stiffness characterization for thermoplastic prepregs at the manufacturing temperature

---

Where  $m$  is the total number of segments of the uniform quartic B-spline curve,  $t$  is the global parameter value of point  $P$  varying from 0 to 1 along the uniform quartic B-spline. The relation between local parameter value  $u^{(i)}$  and global parameter value  $t$  is as following:

$$u^{(i)} = mt - [mt] \quad (2.8)$$

Where  $[mt]$  denotes the nearest integer equal or less than the product of  $m$  and  $t$ .  $i$  is index number of the segment where point  $P$  lies on and can be determined from the global parameter value of point  $P$ :

$$i = [mt] + 1 \quad (2.9)$$

$N_{h,4}(t)$  are called basis functions of uniform quartic B-spline curve:

$$N_{h,4}(t) = \begin{cases} 0; & h < i - 1 \text{ or } h > i + 3 \\ M_{0,4}(u^{(i)}); & h = i - 1 \\ M_{1,4}(u^{(i)}); & h = i \\ M_{2,4}(u^{(i)}); & h = i + 1 \\ M_{3,4}(u^{(i)}); & h = i + 2 \\ M_{4,4}(u^{(i)}); & h = i + 3 \end{cases} \quad (2.10)$$

Uniform quartic B-spline curve has the following important properties:

- **Positional Continuity** (0 order): the end point of segment  $i$  is the same as the starting point of segment  $i + 1$
- **Tangential Continuity** (1st order): no abrupt change in slope occurs at the transition between segment  $i$  and segment  $i + 1$
- **Curvature Continuity** (2nd order): no curvature discontinuity at the transition between segment  $i$  and segment  $i + 1$
- **Continuity of the curvature slope** (3rd order): no discontinuity of the curvature plot at the transition between segment  $i$  and segment  $i + 1$

### 2.3.5.2 Curve fitting based on energy minimization

B-spline curve fitting is intensively studied by various researchers [ROG 89] [PIE 96] [PAR 96b]. The widely used approach is the least squares curve fitting, but many studies show this method would easily cause some unwanted wiggles. The shortcoming of least squares curve fitting method can be overcome by combining energy functional minimization with least-squares error minimization. The energy functional has been used as a fairing term to make curves and surfaces more smooth [CEL 91] [VAS 96]. In the present study, the fitting objective function form proposed by Fang and Gossad [FAN 95]

is adopted, in which both the curve fitting errors and curve energy functional are considered, the objective function form is as follows:

$$\begin{aligned}
 \min E(\tilde{\mathbf{X}}) &= \sum_{j=0}^n w_j \|\mathbf{C}(\bar{t}_j) - \mathbf{P}_j\|^2 + \int_t \left( \alpha \|\dot{\mathbf{C}}(t)\|^2 + \beta \|\ddot{\mathbf{C}}(t)\|^2 + \tau \|\dddot{\mathbf{C}}(t)\|^2 \right) dt \\
 &= (\mathbf{A}\tilde{\mathbf{X}} - \mathbf{P})^T \mathbf{W}(\mathbf{A}\tilde{\mathbf{X}} - \mathbf{P}) + \tilde{\mathbf{X}}^T \left( \int_t \left( \alpha \dot{\mathbf{N}}(\dot{\mathbf{N}})^T + \beta \ddot{\mathbf{N}}(\ddot{\mathbf{N}})^T + \tau \ddot{\mathbf{N}}(\ddot{\mathbf{N}})^T \right) dt \right) \tilde{\mathbf{X}} \\
 &= (\mathbf{A}\tilde{\mathbf{X}} - \mathbf{P})^T \mathbf{W}(\mathbf{A}\tilde{\mathbf{X}} - \mathbf{P}) + \tilde{\mathbf{X}}^T \mathbf{K}\tilde{\mathbf{X}}
 \end{aligned} \tag{2.11}$$

Where the first term in equation (2.11) is called fitting error term and the second term is called fairing term and its role is to smooth the fitting curve.  $n$  is the total number of sample points.  $w_j$ ,  $\alpha$ ,  $\beta$ ,  $\tau$  are the weighting factors.  $\mathbf{C}(t)$  is the position vector of a point on the uniform quartic B-spline with a global parameter value  $t$ .  $\bar{t}_j$  is the global parameter value of sample point  $\mathbf{P}_j$ , here the chord length method is adopted to calculate its value [PAR 96a].  $\tilde{\mathbf{X}} = [\mathbf{B}_0 \ \mathbf{B}_1 \ \cdots \ \mathbf{B}_{m+3}]^T$  is a vector storing control points of  $\mathbf{C}(t)$ .  $\mathbf{P} = [\mathbf{P}_0 \ \mathbf{P}_1 \ \cdots \ \mathbf{P}_n]^T$  is a vector storing the input sample points.  $\mathbf{A}$  is a  $(n+1) \times (m+4)$  matrix of scalars and  $\mathbf{W}$  is a  $(n+1) \times (n+1)$  matrix storing weighting factors  $w_j$ :

$$\mathbf{A} = \begin{bmatrix} N_{0,4}(\bar{t}_0) & \cdots & N_{m+3,4}(\bar{t}_0) \\ \vdots & \ddots & \vdots \\ N_{0,4}(\bar{t}_n) & \cdots & N_{m+3,4}(\bar{t}_n) \end{bmatrix} \tag{2.12}$$

$$\mathbf{W} = \begin{bmatrix} w_0 & \cdots & 0 \\ \vdots & \ddots & \vdots \\ 0 & \cdots & w_n \end{bmatrix} \tag{2.13}$$

Note that  $\dot{\mathbf{N}}$ ,  $\ddot{\mathbf{N}}$  and  $\ddot{\mathbf{N}}$  are the first, second and third derivative of  $\mathbf{N}$  with respect to global parameter  $t$ .  $\mathbf{N}$  is a vector storing the global basis functions and  $\mathbf{N} = [N_{0,4}(t) \cdots N_{m+3,4}(t)]^T$ .  $\mathbf{K} = \int_t \left( \alpha \dot{\mathbf{N}}(\dot{\mathbf{N}})^T + \beta \ddot{\mathbf{N}}(\ddot{\mathbf{N}})^T + \tau \ddot{\mathbf{N}}(\ddot{\mathbf{N}})^T \right) dt = \alpha \mathbf{K}_1 + \beta \mathbf{K}_2 + \tau \mathbf{K}_3$  is called system stiffness matrix owing to its analogy with material mechanics [PAR 00] (seen in Appendix A.1).

Some boundary conditions are imposed for the objective function. Here, the fitting curve is required to pass through the first sample point (first sample point refers to the clamped end of the deflection curve) and the curvature at the last sample point is zero (last sample point refers to the free end of the deflection curve), the corresponding mathematical constraint forms are as follows:

$$\mathbf{C}(0) = \frac{1}{24}(\mathbf{B}_0 + 11\mathbf{B}_1 + 11\mathbf{B}_2 + \mathbf{B}_3) = \mathbf{P}_0 \tag{2.14}$$

$$\ddot{\mathbf{C}}(1) = \frac{1}{2}(\mathbf{B}_m - \mathbf{B}_{m+1} - \mathbf{B}_{m+2} + \mathbf{B}_{m+3}) = \mathbf{0} \tag{2.15}$$

## 2. Bending stiffness characterization for thermoplastic prepregs at the manufacturing temperature

---

Now, the objective function with the boundary constraints can be written as:

$$G(\tilde{\mathbf{X}}, \boldsymbol{\psi}) = (\mathbf{A}\tilde{\mathbf{X}} - \mathbf{P})^T \mathbf{W}(\mathbf{A}\tilde{\mathbf{X}} - \mathbf{P}) + \tilde{\mathbf{X}}^T \mathbf{K}\tilde{\mathbf{X}} + 2(\mathbf{R}\tilde{\mathbf{X}} - \mathbf{D})^T \boldsymbol{\psi} \quad (2.16)$$

Where  $\mathbf{R}$  is a matrix satisfying  $\mathbf{R}\tilde{\mathbf{X}} = \mathbf{D}$ ,  $\mathbf{D} = [\mathbf{C}(0) \quad \ddot{\mathbf{C}}(1)]^T$ .  $\boldsymbol{\psi}$  is a vector storing Lagrange multipliers,  $\boldsymbol{\psi} = [\psi_1 \quad \psi_2]^T$ , others have the same meaning as in equations defined previously. By minimizing  $G(\tilde{\mathbf{X}}, \boldsymbol{\psi})$ :

$$\frac{\partial G(\tilde{\mathbf{X}}, \boldsymbol{\psi})}{\partial \tilde{\mathbf{X}}} = 0 \quad (2.17)$$

$$\frac{\partial G(\tilde{\mathbf{X}}, \boldsymbol{\psi})}{\partial \boldsymbol{\psi}} = 0 \quad (2.18)$$

Then the following equations can be obtained:

$$\begin{bmatrix} \mathbf{K} + \mathbf{A}^T \mathbf{W} \mathbf{A} & \mathbf{R}^T \\ \mathbf{R} & \mathbf{0} \end{bmatrix} \begin{bmatrix} \tilde{\mathbf{X}} \\ \boldsymbol{\psi} \end{bmatrix} = \begin{bmatrix} \mathbf{A}^T \mathbf{W} \mathbf{P} \\ \mathbf{D} \end{bmatrix} \quad (2.19)$$

After solving the equation (2.19), the curvature can be calculated for any point on the uniform quartic B-spline curve:

$$\chi(t) = \frac{\dot{\mathbf{X}}(t) \cdot \ddot{\mathbf{Y}}(t) - \ddot{\mathbf{X}}(t) \cdot \dot{\mathbf{Y}}(t)}{(\dot{\mathbf{X}}^2(t) + \dot{\mathbf{Y}}^2(t))^{\frac{3}{2}}} \quad (2.20)$$

Another problem needed to handle in the fitting is the choice of the number of segments for the uniform quartic B-spline curve. While using too few segments would fail to represent the characteristics of the curve that these sample points represent, using too many would make the fitting curve follow the noise and possess many unwanted undulations [FAN 95]. Figure 2.17 gives an example to show the influence of the number of segments of uniform quartic B-spline on the fitting error and fairness of curvature plot. It shows raising the number of segments would reduce the fitting error between sample points and fitting curve, but the fairness of curvature plot along the fitting curve deteriorates, a balance between the fitting accuracy and curvature fairness should be made to achieve a better solution (in the current example, 3 segments are the best choice). One thing we can state here is that we would prefer using as few segments as possible to fit the sample data points as long as the fitting error is within certain tolerance and meantime the curvature plot has a good fairness. In the present work, the number of segments starts from one. If the fitting error doesn't satisfy the tolerance requirement, the number of segments increases into two. This process is repeated until the tolerance requirement is satisfied and simultaneously keeps an adequate fairness curvature plot. In fibrous reinforcement bending test, most of the time, three segments are enough. In this process, when the curvature plot starts to have the undulation, although the tolerance requirement is not satisfied, it is necessary to stop increasing the number of segments. Its previous

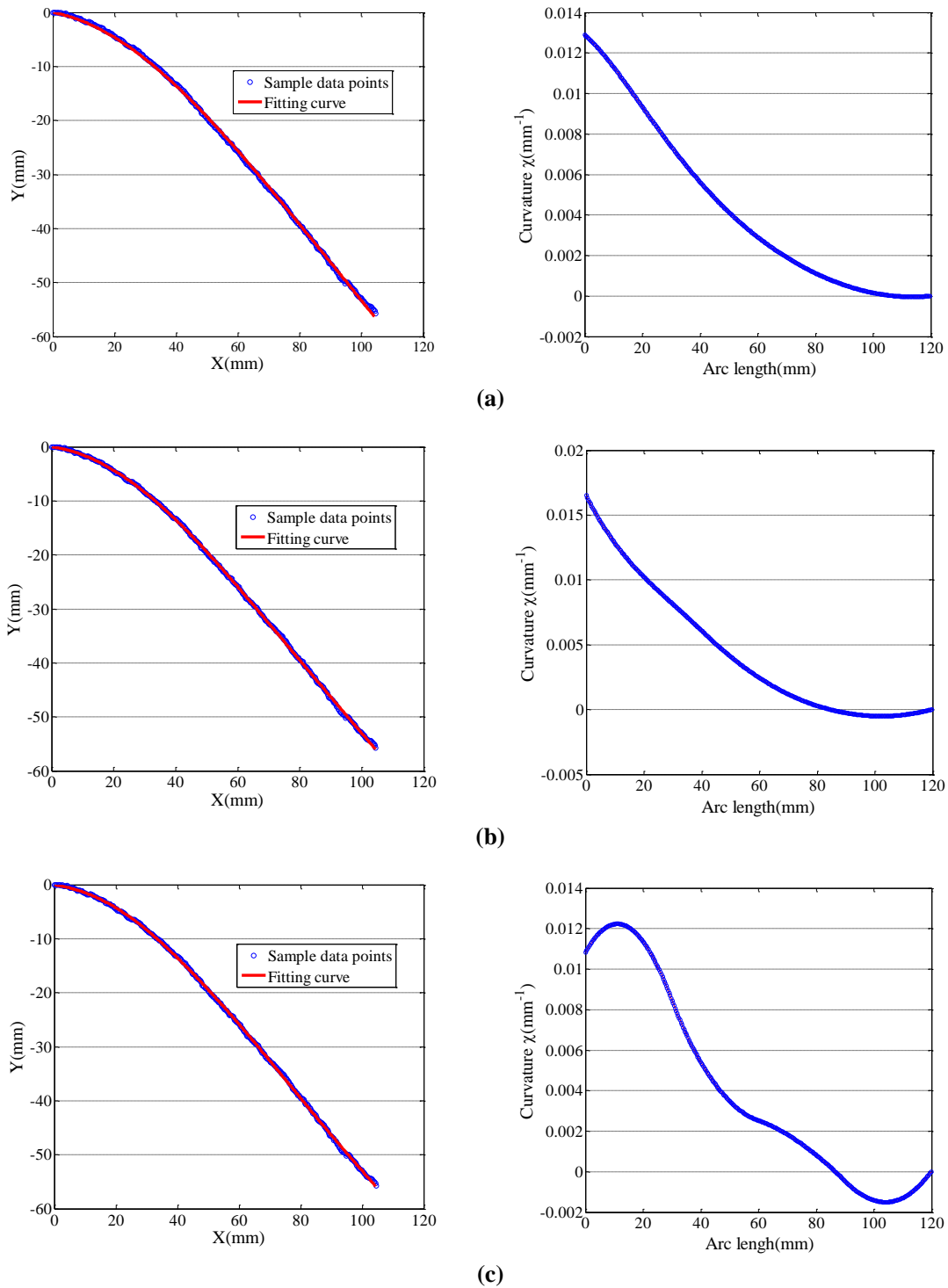


**Figure 2.17** – Influence of the number of segments of uniform quartic B-spline on the fitting error and fairness of curvature plot. Left: sample data points and fitting curve. Right: curvature plot. (a) 1 segment: fitting error 5.71. (b) 3 segments: fitting error 3.31. (c) 4 segments: fitting error 3.1.

## 2. Bending stiffness characterization for thermoplastic prepregs at the manufacturing temperature

value should be ultimately used for the uniform quartic B-spline to fit the sample data points and calculate curvature.

### 2.3.6 Bending moment computation

The stress resultants (normal load  $N$ , shear load  $T$ , bending moment  $M$ ) on the cross-section for the curvilinear abscissa  $s$  are shown in Figure 2.18. The bending moment for any point A along the midline of bending profile under gravity can be calculated as follows:

$$M(s) = \left\| \int_s^L \vec{AB} \wedge q \vec{e} du \right\| \approx \int_s^L q(u-s) \cos(\phi(u)) du \quad (2.21)$$

Where  $s$  is the curvilinear abscissa of point A along the midline,  $q$  is the weight per unit length of sample (N/mm),  $\vec{e}$  is the unit vector in the gravity direction,  $L$  is total length of the bending profile,  $u$  and  $\phi$  are the Frenet's coordinates of point B moving along the profile from A to F and  $du$  is the differential of  $u$ . In equation (2.21), the right part is an approximation form to calculate the bending moment [DEB 10]. When the bending deformation is not very large, the difference between the left and right part can be neglected, but when the bending deformation is large, it's suggested to use the left part of equation (2.21) to more accurately calculate the bending moment.

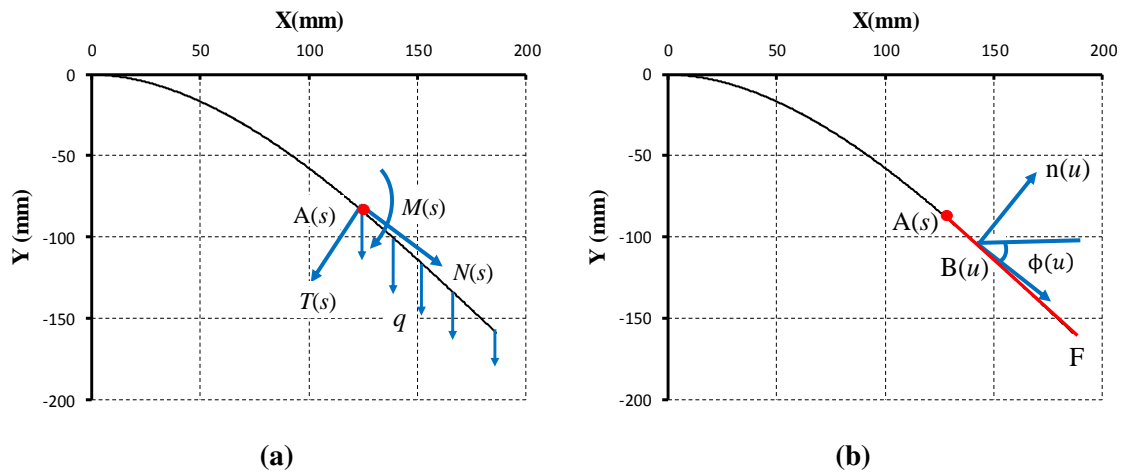


**Figure 2.18** – Moment calculating. (a) Stress resultants ( $N$ ,  $T$ ,  $M$ ) on the cross-section for the curvilinear abscissa  $s$ . (b) Frenet's coordinates.

## 2.4 Bending experimental test campaign

### 2.4.1 Interested materials

Three types of thermoplastic prepregs are investigated in this thesis for their bending behaviour. They are PPS-Carbon satin prepreg, PEEK-Carbon satin prepreg and PA66-Glass satin prepreg (Figure 2.19). PPS-Carbon satin prepreg and PEEK-Carbon satin prepreg are powder impregnated prepregs, they are made of single ply, while PA66-Glass satin prepreg is a pre-consolidated laminate made of five plies. Their properties are shown in Table 2.1. In the test, PPS-Carbon satin prepreg and PEEK-Carbon satin prepreg are tested directly with the testing procedure mentioned previously, but for PA66-Glass satin prepreg, there is a little difference for the testing procedure due to its multi-ply feature and would be introduced in a separated section.

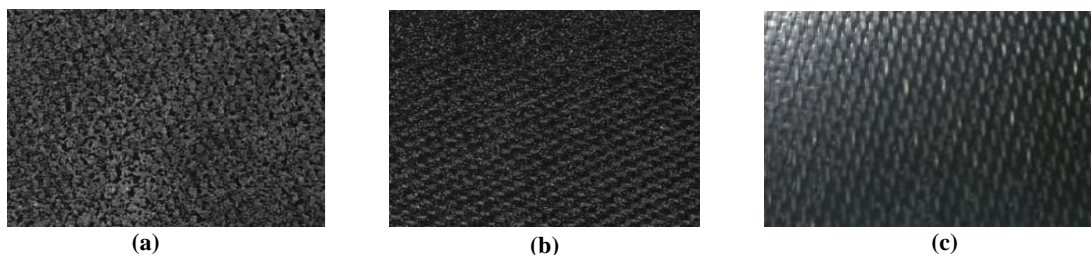


**Figure 2.19** – Interested materials. (a) PEEK-Carbon satin prepreg. (b) PPS-Carbon satin prepreg. (c) PA66-Glass satin prepreg.

**Table 2.1** – Properties of interested materials

Prepreg type	PPS/Carbon satin	PEEK/Carbon satin	PA66/Glass
Areal density	497g/m <sup>2</sup>	477g/m <sup>2</sup>	3610g/m <sup>2</sup>
Thickness	0.319 mm	0.310 mm	2 mm
Reinforcement	5-harness satin	5-harness satin	8-harness satin
Fibers	Carbon	Carbon	Glass
Matrix type	PPS	PEEK	PA66
Volume fraction	50%	50%	50%

### 2.4.2 Bending test for PPS-Carbon satin prepreg and PEEK-Carbon satin prepreg

The length and width of sample are 200 mm x 50 mm. One principle of determining the value of sample's width in the bending test is it should allow to have no or less twist. It's suggested the ratio of bending length to the width of sample is larger than 2. In practice it has found if this ratio is too small, it's more likely to have twist in the bending. The

## 2. Bending stiffness characterization for thermoplastic prepregs at the manufacturing temperature

---

value of sample's length only determines the maximum bending deformation it can reach. The bending length in the present study is 120 mm. Tests are carried out in the warp yarn direction ( $0^\circ$ ) and weft yarn direction ( $90^\circ$ ) respectively, other directions are neglected due to their weak bending stiffness. In the test, it has found both of the two types of prepregs are not symmetrical about the middle surface in the bending (satin weave is unbalanced). Consequently, the bending tests were performed both with the upper face on top and the bottom face on top, then the mean deflection curve from those two tests is used as the deflection curve to characterize the bending behaviour (Figure 2.20). This process would be iterated at least three times in each bending direction. For visual clarity, the following results are the average of these tests without standard deviations.

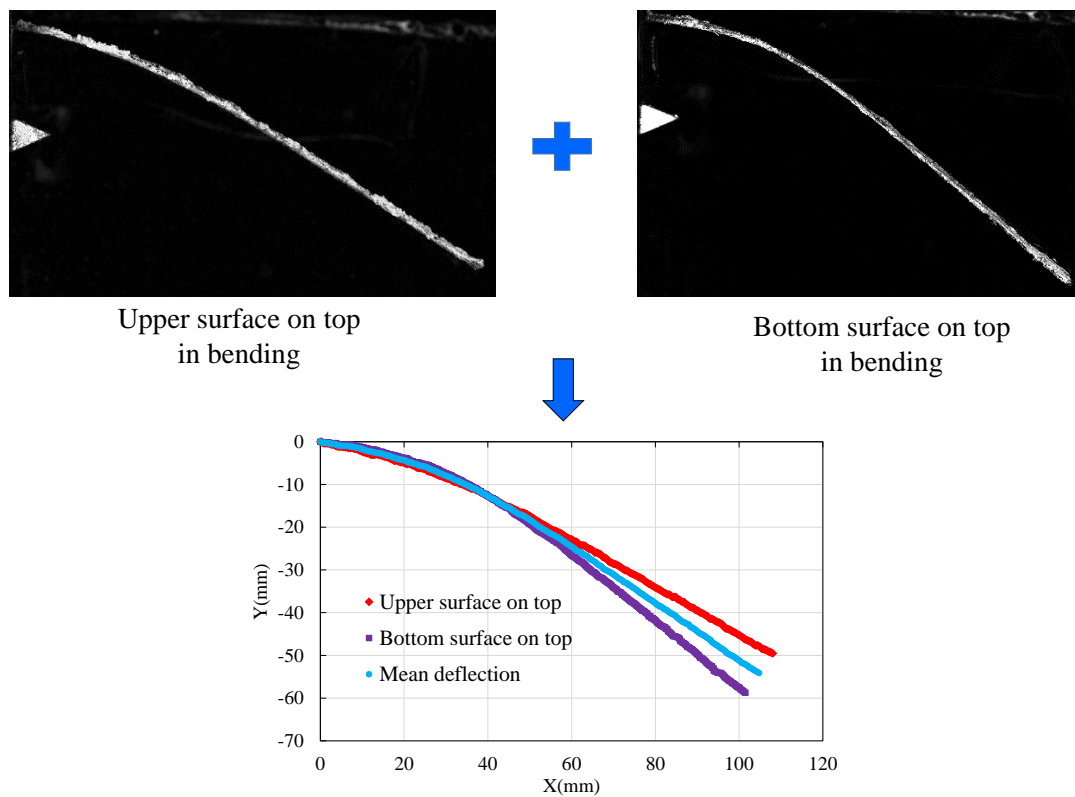
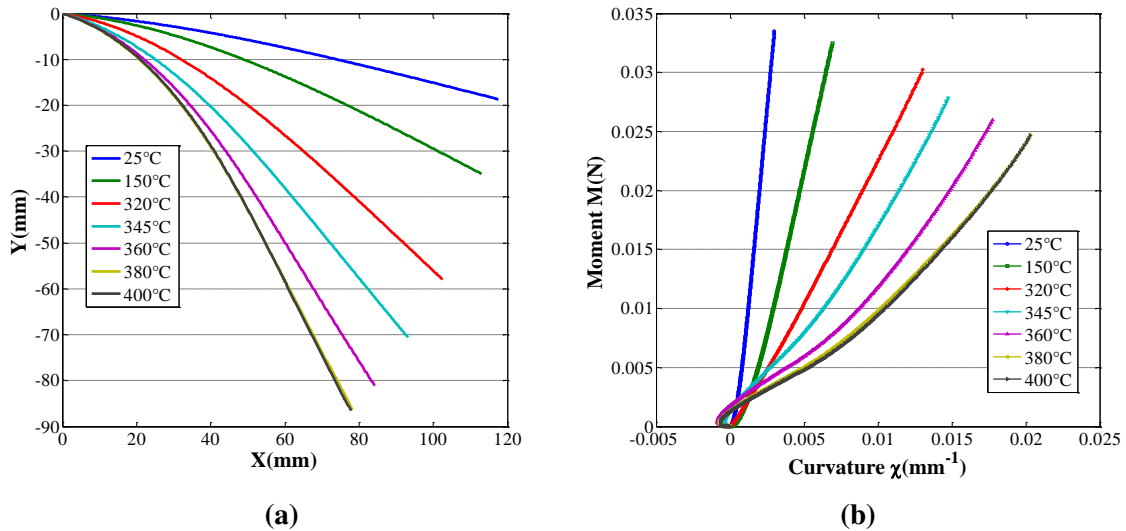


**Figure 2.20** – The definition of mean deflection curve.

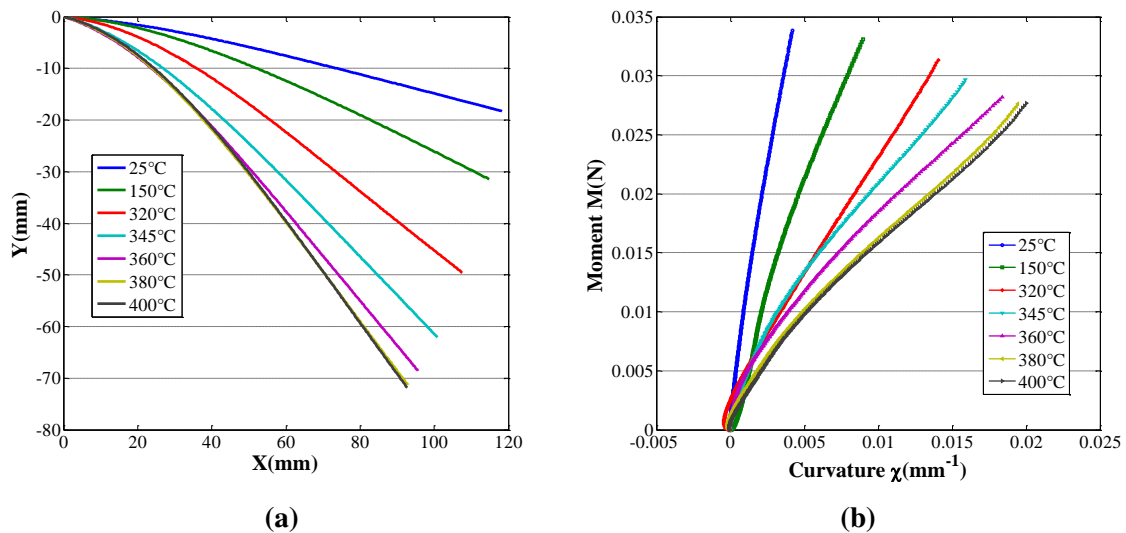
### 2.4.2.1 Experimental results only the gravity

Figure 2.21a shows the deflections of PEEK-Carbon satin prepreg specimens in  $0^\circ$  (the warp direction coincides with the long dimension of the specimen). The deflection is measured under seven different temperatures, from room temperature ( $25^\circ\text{C}$ ) to  $400^\circ\text{C}$ . Four of them cover the range of manufacturing temperatures ( $320^\circ\text{C}$ ,  $345^\circ\text{C}$ ,  $360^\circ\text{C}$ ,  $380^\circ\text{C}$ ). These are close to the melting temperature of PEEK resin ( $343^\circ\text{C}$ ). The deflection increases with the temperature. Nevertheless, at  $380^\circ\text{C}$  the deflection is maximal and does

not increase any more for higher temperatures. This is due to for these higher temperatures, the resin is entirely melted and the bending stiffness is mainly a result of the carbon fabric whose properties are constant in this interval of temperatures.



**Figure 2.21** – PEEK-Carbon satin prepreg bending experiment (orientation 0°). (a) Deflections for different temperatures. (b) Bending moment versus curvature.



**Figure 2.22** – PEEK-Carbon satin prepreg bending experiment (orientation 90°). (a) Deflections for different temperatures. (b) Bending moment versus curvature.

The bending moment versus curvature curves obtained from the deflections following the methods described previously for curvature and for bending moment are presented in Figure 2.21b. Moment is in N (Moment per unit width,  $N = N \cdot \text{mm}/\text{mm}$ ). Note that the unit of bending stiffness used in there is  $N \cdot \text{mm}$ , which denotes the bending stiffness

## 2. Bending stiffness characterization for thermoplastic prepregs at the manufacturing temperature

per unit width. The obtained curvature reaches  $0.02 \text{ mm}^{-1}$  at the clamped end when the temperature is  $380 \text{ }^\circ\text{C}$  or over. The curvatures calculated near the free edge of the specimen (i.e. for a small bending moment) are not accurate and should not be taken into account. This part of specimen is very flat, the curvature is close to zero and its calculation is inaccurate. The results can be considered correct for curvatures larger than  $0.002 \text{ mm}^{-1}$ . For the PEEK-carbon satin prepreg, the bending moment versus curvature curve for a given temperature is not linear but it's not very far.

Figure 2.22 gives the deflection and moment versus curvature curves for the same PEEK-Carbon satin prepreg but with a  $90^\circ$  orientation of the fabric (the weft direction coincides with the long dimension of the specimen). The resulting moments, plotted against curvature, for the warp direction are only slightly different from those obtained in the weft direction (difference inferior to 15%). This unbalance is mainly due to manufacturing constraints. During numerical forming simulations one could consider the properties of the warp and weft directions as identical for added simplicity, or they could be different for added precision.

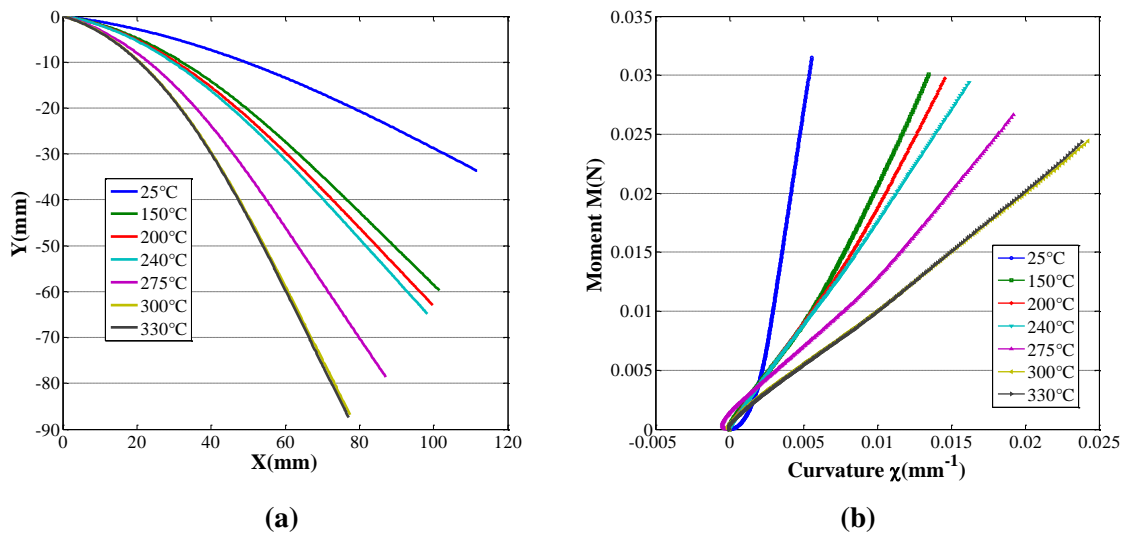


**Figure 2.23** – PPS-Carbon satin prepreg bending experiment (orientation  $0^\circ$ ). Deflections for different temperatures. (b) Bending moment versus curvature.

Figure 2.23 shows the deflections and the bending moment versus curvature curves of the PPS-Carbon satin prepreg for a  $0^\circ$  orientation. The results are of the same nature as those obtained for the PEEK prepreg. The main difference lies in the height of the temperatures. The manufacturing temperature for PPS-Carbon satin is around its melting temperature which is  $285 \text{ }^\circ\text{C}$ . Similarly to PEEK prepreg, the deflection reaches a maximum just above its melting temperature ( $300 \text{ }^\circ\text{C}$ ) and does not increase for higher temperatures. Figure 2.24 shows the deflection and bending moment versus curvature curves for a  $90^\circ$  orientation of PPS-satin specimens.

In order to verify the reproducibility of the measures, two bending tests, respectively at  $200 \text{ }^\circ\text{C}$  and  $380 \text{ }^\circ\text{C}$ , were performed on different PEEK-carbon satin prepreg specimens

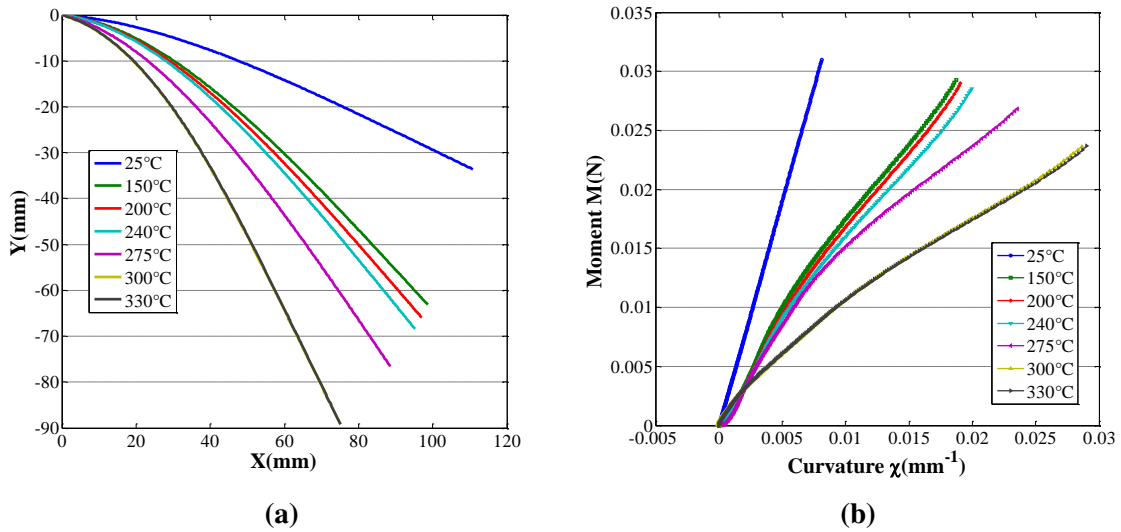


**Figure 2.24** – PPS-Carbon satin prepreg bending experiment (orientation 90°). Deflections for different temperatures. (b) Bending moment versus curvature.

(oriented in 0°). The first temperature is below the melting point, and the second is over the melting point. The results are given in Figure 2.25. The bending moment versus curvature curves are somewhat different but the difference neighbors 10%. This can be considered as acceptable for this type of test.

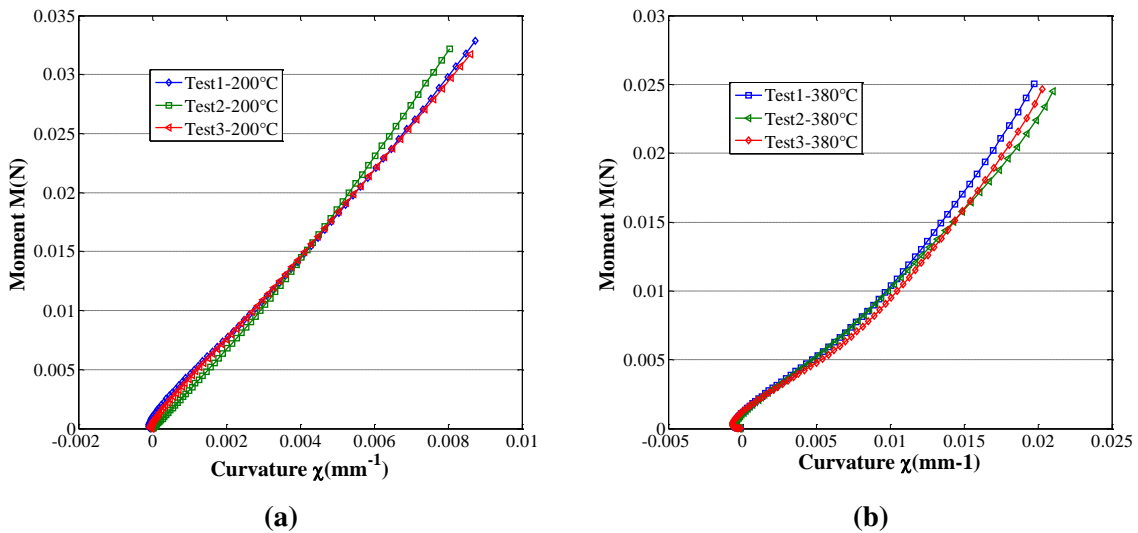


**Figure 2.25** – Reproducibility tests of PEEK-Carbon satin prepreg: (a) 200°C. (b) 380°C.

#### 2.4.2.2 Experimental results with added lump mass

It can be interesting to obtain the bending stiffness for larger curvatures. To this end, test can be performed on longer specimen. This kind of test would need a large environmental

## 2. Bending stiffness characterization for thermoplastic prepregs at the manufacturing temperature

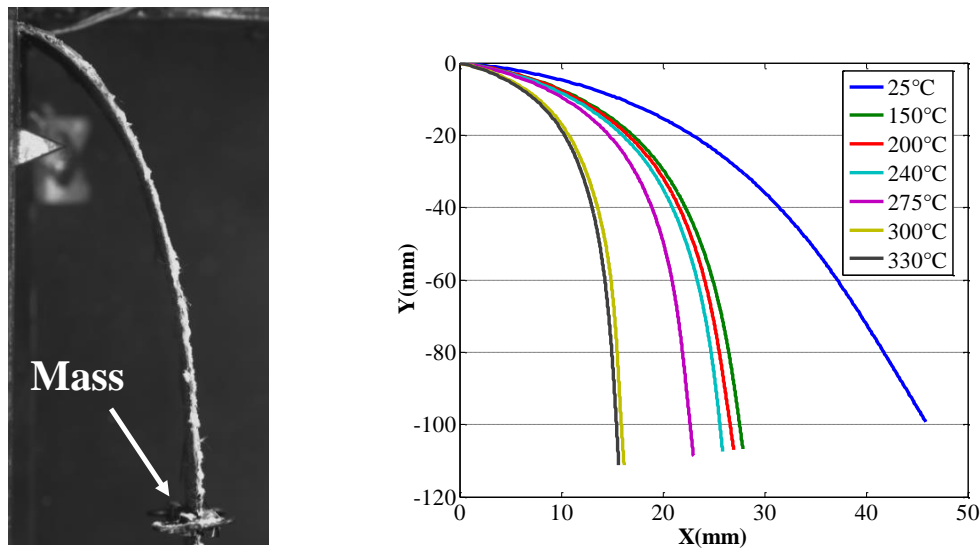


**Figure 2.26** – Bending tests with an added lump mass.

chamber. It would not be possible with the instron chamber shown in Figure 2.10. To increase the curvatures without changing the length of specimen, a lumped mass ( $m = 11$  grams) is added at the free edge of the specimen (Figure 2.26). With the lump mass, it can reduce the distortion compared with the one that is only under its own gravity. The bending moment at point A is increased by  $m \cdot g \cdot (X(F) - X(A))$  and the curvature reaches higher values (up to  $0.07 \text{ mm}^{-1}$ ).

These new moment-curvature curves are compared to the curves obtained without lump mass (Figure 2.27). This comparison is possible by only considering the part of the curves with low curvatures. Their results are in good agreement. The measures for low curvatures are nevertheless more accurate for that without mass, because they are obtained from measures throughout the whole length of the specimen. With the lump mass the low curvatures can only be calculated from measures in the part close to the free edge of the specimen where they intend to have a larger error. To reach higher curvatures, the lump mass can be increased. However, there is a limit. When the bent specimen gets to be vertical, the loading can no longer be characterized as bending.

### 2.4.3 Bending test for PA66-Glass satin prepreg

Bending tests have been carried out for PA66-Glass satin prepreg, where the experimental procedure initially was the same as that used for single ply prepreg mentioned previously. The delamination was observed in the bending test (Figure 2.28). One possible reason causes the delamination is due to in the process of heating the sample to the desired high temperature, it's unavoidable to have temperature gradient. The viscosity of resin is temperature dependent and strongly affects the bending stiffness of each ply. When subjected to bending, some plies would have larger out of plane bending deformation than others, then the delamination occurs. Another possible reason is PA66-Glass satin

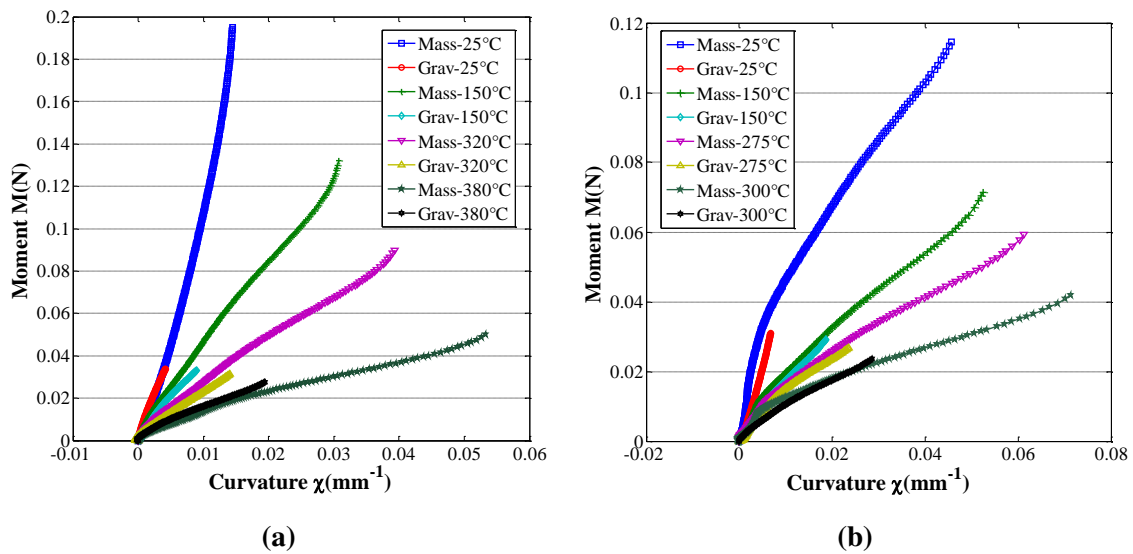


**Figure 2.27** – Bending tests with an added mass: moment versus curvature and comparison with tests without mass. (a) PEEK prepreg. (b) PPS prepreg.

prepreg is pre-consolidated prepreg, there exists the residual compression stress, when the resin is melted, this energy would release and cause the delamination. To avoid the delamination, prior to the desired high temperature is reached at a homogenous state, the

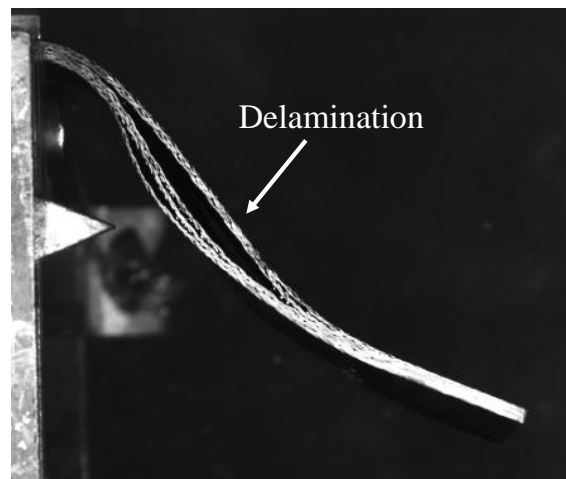


**Figure 2.28** – Delamination was observed in the bending test for PA66-Glass satin prepreg.

sample shouldn't be bent. Consequently, an extra support is used to support the sample in the heating process (Figure 2.29). When the desired temperature is reached and is uniform within the sample, the extra support is removed slowly to let the sample bend under gravity (Figure 2.29).

The accurate temperature measurement is very important for laminated prepreg in

## 2. Bending stiffness characterization for thermoplastic prepregs at the manufacturing temperature

---

the test. For single ply prepreg, its thickness is very small, the temperature gradient through the thickness direction can be neglected, however, for laminated prepreg it's not the case. Thermocouples should be placed at the interior of sample instead of at the external surface to measure the temperature field. A sets of bending tests have been conducted for PA66-Glass satin prepreg with the improved bending test procedure. The length and width of sample are 120 mm x 25 mm, the bending length is 80 mm. PA66-Glass satin prepreg has been compacted at high temperature, so at room temperature it's very stiff. The bending deflection at room temperature is almost zero. The bending deflections and the corresponding curvatures at different temperatures are given in Figure 2.30. In the manufacturing temperatures range from 260 °C to 320 °C, the maximum bending deflection is reached at 300 °C. Above this temperature the bending stiffness is primarily due to the glass fabric and not change with temperature.

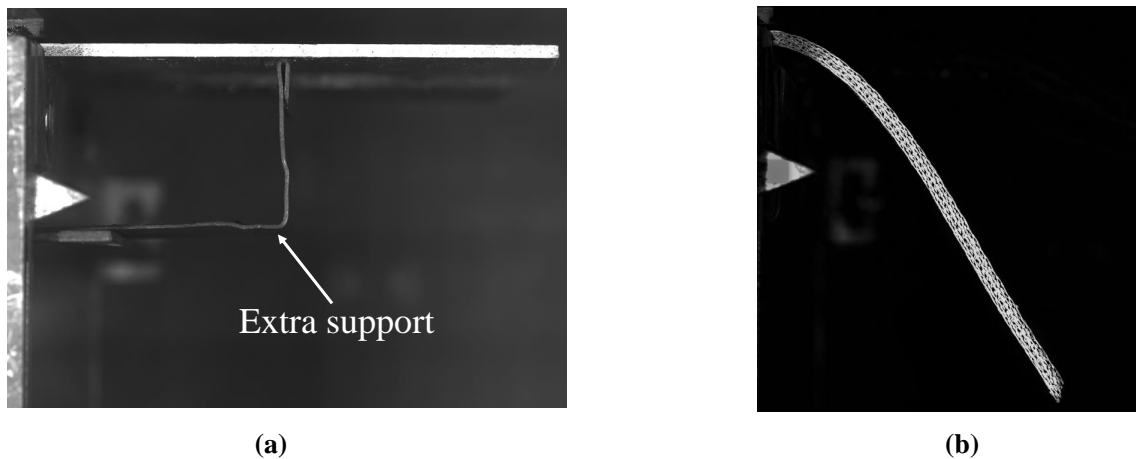


**Figure 2.29** – Bending profile for PA66-Glass prepreg. (a) At room temperature (25°C). (b) At high temperature (260°C).

### 2.5 Forming simulations: influence of the bending stiffness on wrinkling development

The simulations in this section are performed using the PlasFib F.E. software developed at INSA Lyon [HAM 08, HAM 09]. This software is based on an explicit dynamic approach. The finite element is a semi-discrete triangle described in [HAM 08]. It is a rotation free shell element. There is no rotational degree of freedom. The curvatures are obtained from the neighboring elements. The contact- friction is taken into account using forward increment Lagrange multipliers. The coulomb friction between the tool-ply is considered with a coefficient value 0.2. A lubricated friction model can be used as well without modifying the analysis conclusions [FET 13, WAN 13]. The in-plane shear properties of PEEK-Carbon satin prepreg and PPS-Carbon satin prepreg have been measured for

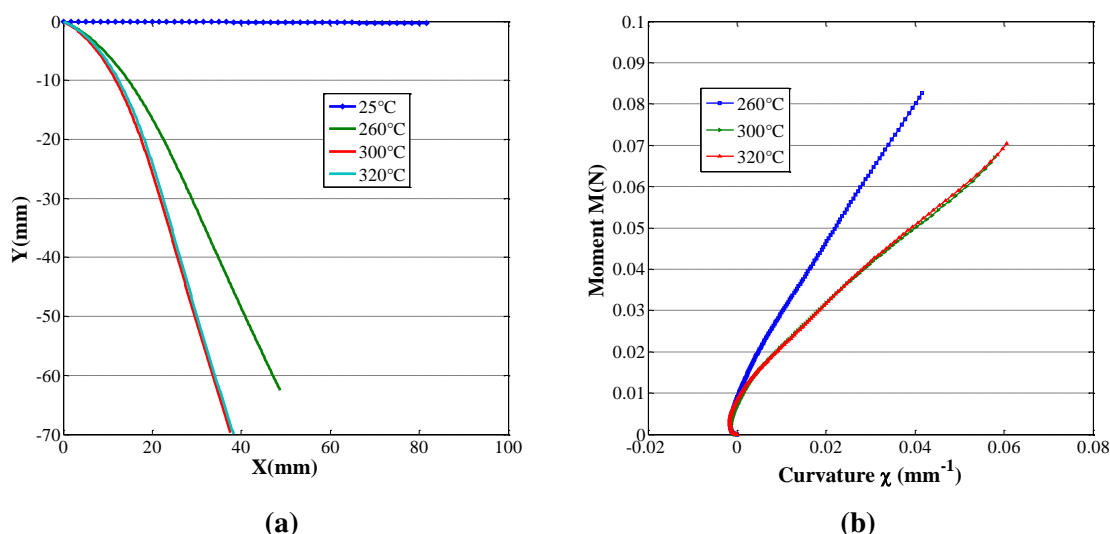


**Figure 2.30** – PA66-glass prepreg bending (orientation 0°). (a) Deflections for different temperatures. (b) Bending moment versus curvature.

different temperatures through a bias extension test [WAN 14]. The bending properties measured in Section 2.4 are used in the simulations. The objective is to quantify the influence of bending stiffness on wrinkling during the forming process.

### 2.5.1 Wrinkling in compression

The warp and weft yarns of a rectangular prepreg strip are parallel to the edges of the specimen (Figure 2.31). A compressive displacement ( $U_d = 15\text{mm}$ ) is prescribed on each edge of the strip (initial dimensions: 80 mm x 20 mm). The resulting wrinkles are shown for different bending rigidities of the PEEK-Carbon satin prepreg at 150°C, 320°C and 380°C. The size of the wrinkles increases along with the bending stiffness. Consequently the number of wrinkles increases along with the temperature which renders the prepreg less stiff to bending. Textile and prepreg reinforcements are very sensitive to compression in the yarn direction. Buckling is almost instantaneous in this context. Therefore, compression is generally avoided in forming processes. Devices such as blank holders are used to avoid compressive states in the fabric.

### 2.5.2 Influence of bending stiffness on wrinkling during forming

The simulation of the forming of a PPS-Carbon satin prepreg by a cylindrical punch is performed under different conditions. The geometry of punch, die and blank holder are shown in Figure 2.32. The blank is meshed using 48000 triangular shell elements (surface dimension of blank is 400 mm x 400 mm). The goal of this section is to investigate the importance of taking into account the bending stiffness of thermoplastic prepreg in thermoforming simulation, particularly the influence of bending rigidity on wrinkling will

## 2. Bending stiffness characterization for thermoplastic prepregs at the manufacturing temperature

---

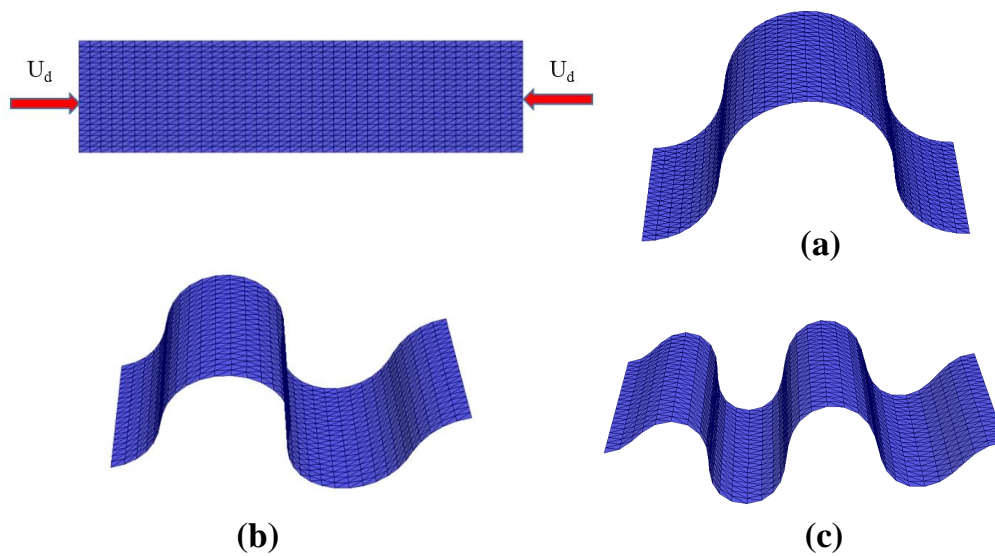


**Figure 2.31** – Simulation of compression of a prepreg strip. (a) 150°C. (b) 320°C. (c) 380°C.

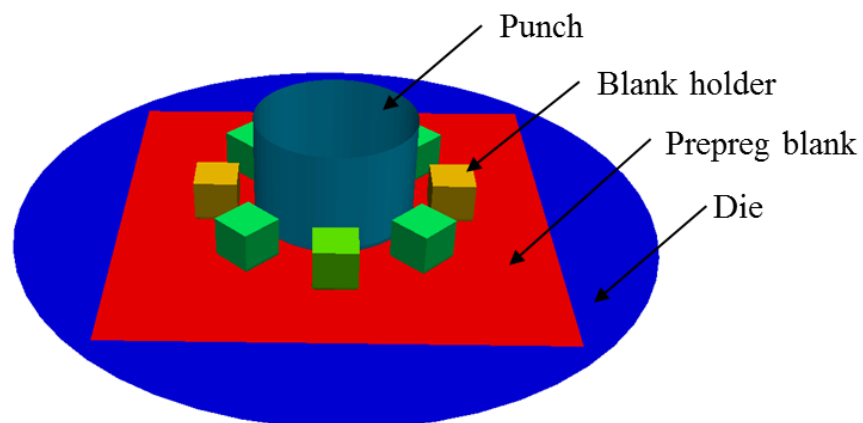


**Figure 2.32** – Forming with a cylindrical punch.

be analyzed.

### 2.5.2.1 The Importance of taking into account the temperature

Figure 2.33 shows the deformed shape computed with bending and in-plane shear at 275°C and 300°C respectively. Even though these temperatures are rather close, the deformed shapes are different. There are many wrinkles at 275°C and almost no wrinkles at 300°C. One explanation is that the melting temperature of the resin is between these two temperatures. It is common in a thermoforming process that two areas of a composite part have such temperatures. This example shows that taking into account the temperature in bending and in-plane shear properties is necessary in a thermoforming simulation.

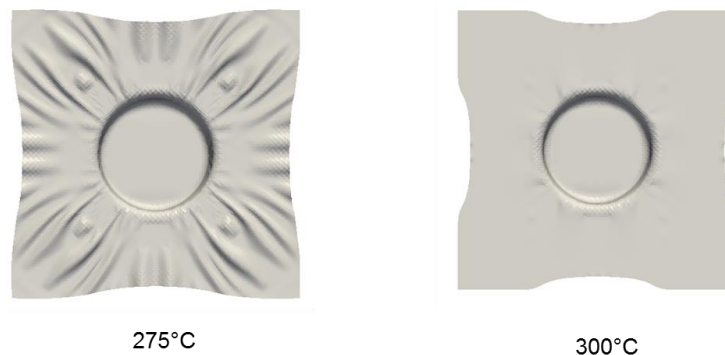


**Figure 2.33** – Forming simulations with prepreg properties at 275°C and 300°C.

### 2.5.2.2 The importance of taking into account bending stiffness

Figure 2.34 presents the deformed shapes obtained from the simulation of thermoforming at 275°C taking into account both in-plane shear stiffness and bending stiffness in Figure 2.34a and taking into account in-plane shear without bending stiffness in Figure 2.34b. There are many wrinkles in both cases but these wrinkles are numerous and small when the bending stiffness is neglected. This corresponds to a membrane assumption that is not able to describe the wrinkle shape. Bending stiffness is necessary to correctly describe wrinkle shape.

### 2.5.2.3 Sensitivity analysis of bending stiffness on wrinkling

Figure 2.35a shows the computed deformation shape of a PPS-Carbon satin prepreg blank when the temperature is set to 275°C. The simulation is performed with experimentally measured values of in-plane shear and bending properties. It is the reference example in this section. In each case, the in-plane shear stiffness is set to the value measured in [23] at 275 °C. The objective of this section is to reveal the effects of the varying bending stiffness (multiplied by 0.1, 0.5, 2 and 10) on the deformed shape, particularly on wrinkles and maximum shear angles. Figure 2.35b shows the computed deformed shape when the

## 2. Bending stiffness characterization for thermoplastic prepregs at the manufacturing temperature

---

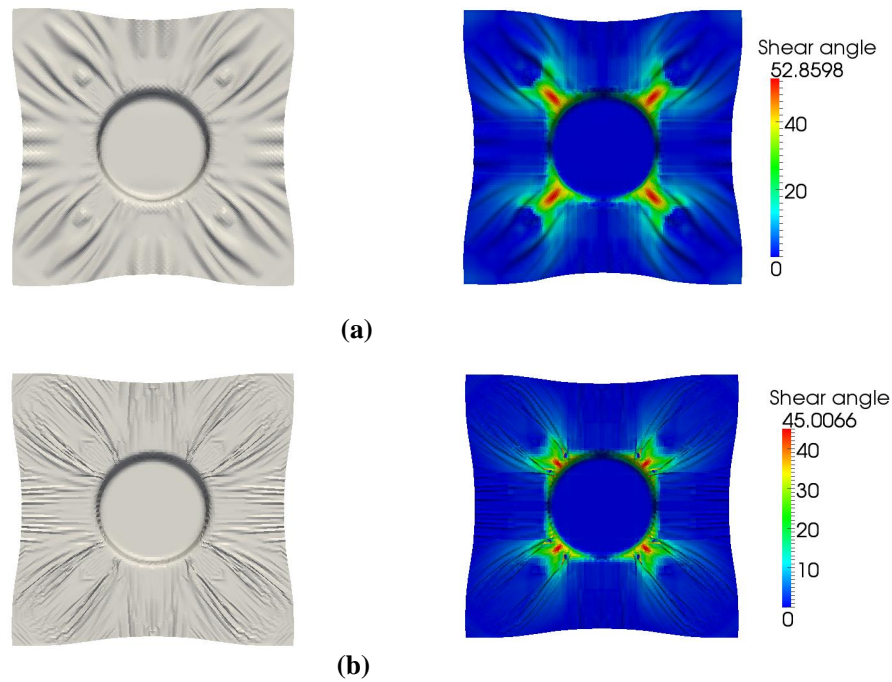


**Figure 2.34** – Simulation of a thermoforming at 275°C. (a) With in-plane shear and bending stiffnesses. (b) With in-plane shear stiffness and without bending stiffness.

bending stiffness is multiplied by 0.1. There are significant differences with the reference simulation (Figure 2.35a). There are more wrinkles in Figure 2.35b and they are smaller. The maximum shear angles are smaller (51°) than in the reference (53°). Figure 2.35e shows the computed deformed shape when the stiffness is multiplied by 10. There are significant differences with the reference test (Figure 2.35a). There are larger wrinkles in Figure 2.35e and they are less numerous. The maximum shear angle is larger (55°) than in the reference which is 53° (Figure 2.35a). Consequently, the difference in bending stiffness ( $\times 10$  in Figure 2.35e and  $\times 0.1$  in Figure 2.35b) leads to two distinct solutions both different from the reference. On the other hand the results obtained in the case of Figure 2.35c (bending stiffness multiplied by 0.5), Figure 2.35a (reference) and Figure 2.35d (bending stiffness multiplied by 2) are close. There are some differences, but they are small. The simulations made with a bending stiffness between half and twice the reference bending stiffness give rather close results.

The forming simulations above give some information regarding the influence of bending stiffness:

- It is important to take into account bending stiffness in a forming simulation, chiefly to describe wrinkling (Figure 2.33 and 2.34)
- It is essential to take into account the effect of temperature that can lead, or not, to wrinkles (Figure 2.33)

- The size of wrinkles obtained in the simulation depends on bending stiffness. Consequently, it is necessary to include bending properties and their variation along with temperature to correctly compute the wrinkles.
- The shape and size of wrinkles depend on bending stiffness but the dependence is rather weak. Measurements of bending stiffness are difficult. If they are not very accurate, the forming simulation results will not be much affected (Figure 2.35).

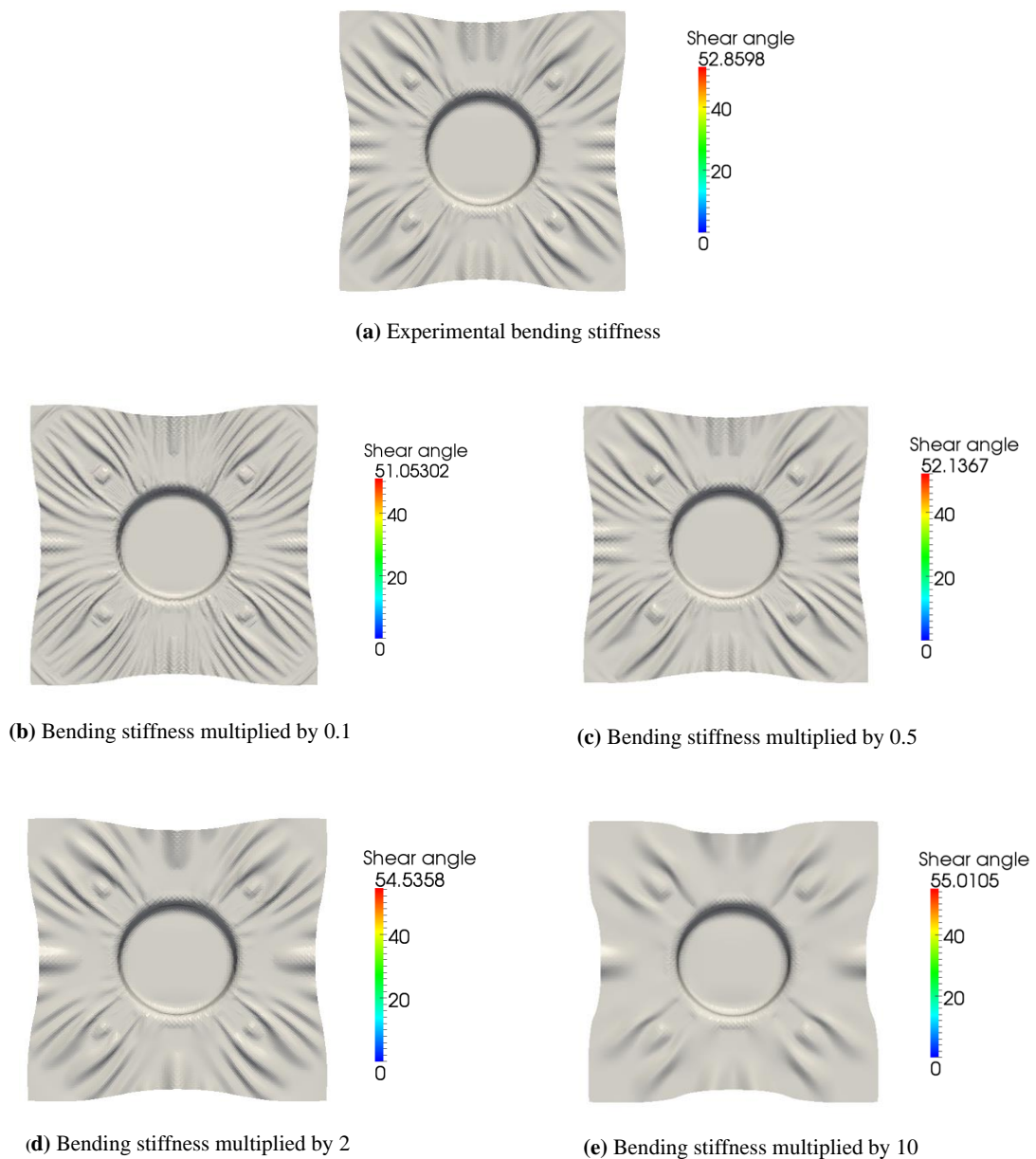


**Figure 2.35** – Sensitivity analysis on the bending stiffness.

## 2.6 Conclusions of chapter 2

A short review about the available bending stiffness test methods for textile dry reinforcement and thermoplastic composites was made. Based on their advantages and disadvantages, an improved cantilever bending test method for thermoplastic prepregs has been proposed. Bending test was operated in a thermal environmental chamber. The homogeneity of temperature within the specimen was tested by a set of thermocouples. The bending deflection shape was acquired by a CCD camera and image processing was used to extract its midline. Midline was fitted by the uniform quartic B-spline curve that gave the curvature. The bending moment versus curvature curves were obtained for PEEK-carbon satin prepreg, PPS-carbon satin prepreg and PA66-Glass satin prepreg within a set of temperatures including the manufacturing temperatures. The bending deflection increases strongly with temperature until a limit was reached in which the resin is completely melted and the bending stiffness mainly comes from the fibers. The measured bending stiffness was used in the thermoforming simulations. Taking into account the bending stiffness of prepreg at the manufacturing temperature is important. Notably it determines the size and shape of wrinkles. Although wrinkle size and shape depend on the material's bending stiffness, this dependence shows itself slowly with regard to the bending stiffness variation.

# Chapter 3

## Specific plane shell element for simulating the bending deformation of thick fibrous materials

### 3.1 Introduction

Thick fibrous materials, such as laminated reinforcements and 3D NCF (Non-crimp fabric) have been successfully used in recent decades in aircraft construction and civil engineering due to their attractive properties of strength, stiffness, and lightness [POR 01, TON 02, DOU 06, MAT 15]. In the present study, thick fibrous materials are continuous fiber reinforced and are only restricted to those whose fibers can be seen as parallel and straight in the material direction. In the forming process of composite part, bending deformation is an important deformation mode, particularly for the double curved part. Compared with the classical continuous materials, the mechanical behavior of thick fibrous materials is very special: because of the absence of resin or resin is melted at the high temperature, fibers that constitute the reinforcement can slide to each other during the deformation. This behaviour can result in significant influence on its kinematics and rigidities. In the section 3.2, some bending tests would show this influence on the bending kinematics and their specialties compared with the classical continuous materials.

Few models currently are available to simulate the bending deformation of thick fibrous materials. De Luycker et al [DEL 09] developed a semi-discrete finite element made of yarn segments to simulate the deformation of thick interlock. This model is efficient in most interlock deformation simulations but some difficulties have been seen to simulate the bending deformation. The main reason lies in their model, yarn segment only accounts for tensile stiffness, while bending stiffness is neglected. Consequently, it's unable to correctly simulate the deformation when bending is the primary deformation mode. Charmetant et al [CHA 12] proposed a hyper-elastic continuum model with 3D hexahedral finite element to simulate the deformation of layer to layer angle interlock. This model works well to predict most deformation modes of interlock but some limits have been highlighted in some bending situations. Three points bending test clearly

### 3. Specific plane shell element for simulating the bending deformation of thick fibrous materials

---

demonstrates this model is unable to correctly simulate the bending deformation of interlock. One main reason is it failed to take into account the local bending energy of fibers in the hyper-elastic constitutive model. To include the bending energy of fibers, A.Madeo et al [MAD 15] have proposed a second gradient model for characterization of the mechanical behaviour of thick interlock. Such second gradient theory is seen being able to directly account for the bending energy of fibers. This model has been used to simulate the three points bending test of interlock to verify its capability. It gives a satisfactory result and captures the main deformation features observed in the bending test. But the main drawbacks are the second gradient theory is relatively complicated than the classical continuum mechanics (or first gradient theory) and some additional variables in the second gradient model need be identified by the experiments. Some experiments even are difficult to conduct.

Based on the aforementioned issues, another purpose of this thesis is to develop a specific shell element made of continuous fiber segments to simulate the bending deformation of thick fibrous materials. In the first step, a shell element in the plane will be considered for simplicity reason. Both the tensile and bending stiffnesses of fibers are taken into account in this element. The deformation theory of this plane shell element falls within the frame work of classical continuum mechanics. Therefore, it's relatively simple and less mechanical parameters need to be identified compared with the second gradient model.

## 3.2 The highlight of the specific bending behaviour of thick fibrous materials

Thick fibrous materials can be seen as an assembly of fibers. In this thesis, book is selected as an example since it's a layered structure. In the bending, each page paper is close to be inextensible and there exists slippage between papers, which are very similar to the bending kinematics of thick fibrous materials composed by parallel fibers. Therefore, bending deformation experiments of book and thick fibrous materials have been conducted respectively to show the specific bending deformation mechanism of thick fibrous materials (Figure 3.1). To track the motion of material points, some straight lines are drawn on the cross-section of book and some soft filaments are attached on the thick fibrous reinforcements. The unit vector of the drawn straight line or the filament is called material director. Some interesting points can be noted from the experiments:

- In certain deformation region, there is almost no rotation for the material director, curvature of mid-surface or fibers in this region is not zero (region A in Figure 3.1a, b and c).
- There exists a thickness stretching in the material director direction (region B in Figure 3.1a, b and c).

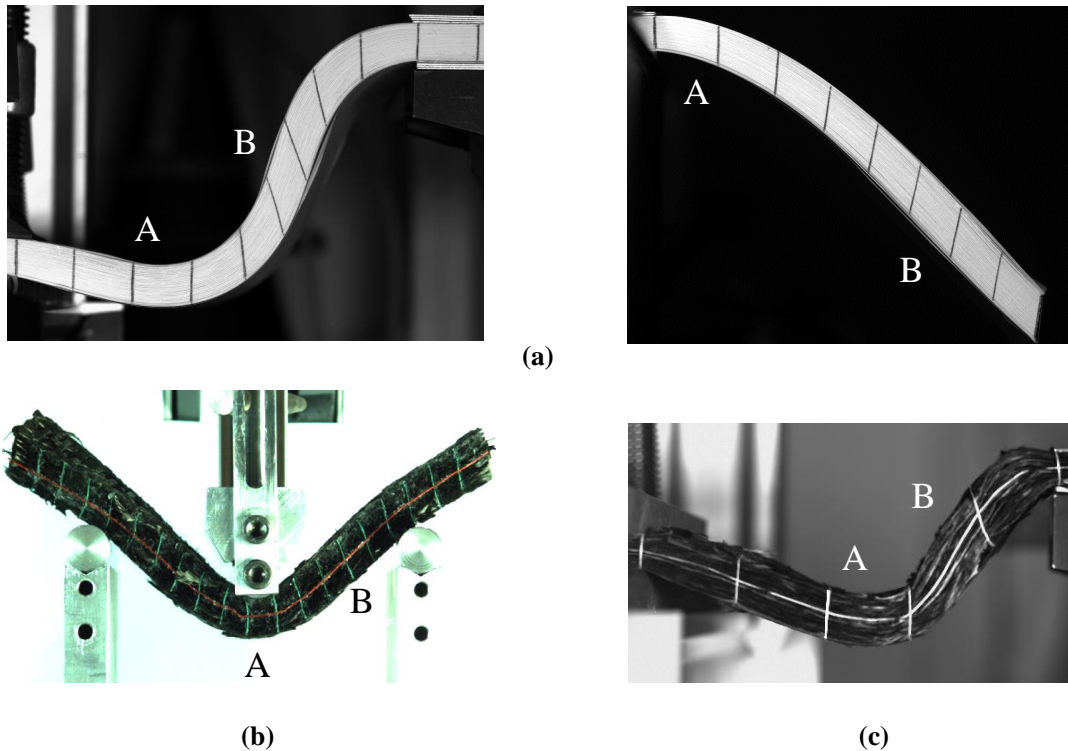


**Figure 3.1** – Bending deformation experiments. (a) Book made of 130 pages. (b) Layer to layer angle interlock [MAT 15]. (c) Laminated reinforcement (all plies are orientated in the same direction).

These observed phenomenons are not consistent with the Mindlin shell theory. In Mindlin shell theory, curvature is defined only for the points located on the mid-surface and is defined as the first derivative of the rotation angle of the material director [BAT 85, ZIE 05]. Following this curvature definition, if there is no rotation for the material director, the mid-surface's curvature should be zero. However, this curvature definition contradicts with what we have observed in the bending experiments (region A in Figure 3.1a, b and c, there is almost no rotation for the material director, but curvature of mid-surface is not zero and there also exists curvature variation along the material director direction). One conclusion can be made is for the shell structure of thick fibrous materials, its mid-surface's curvature is not directly related to the first derivative of rotation angle of material director as that for the shell structure of classical continuous materials. Besides, in Mindlin shell theory it's supposed the thickness in the material director direction keeps constant during deformation [BAT 85, BIS 04], which also contradicts with the experimental results (region B in Figure 3.1a, b and c, there is a stretching in the material director direction). These facts demonstrate that Mindlin shell theory is unable to describe the bending deformation of thick fibrous materials. Consequently, Mindlin shell element is incapable to correctly simulate the bending of thick fibrous materials. In this thesis, we would like to propose a specific shell element which is able to simulate the bending defor-

### 3. Specific plane shell element for simulating the bending deformation of thick fibrous materials

---

mation of thick fibrous materials. Its kinematics are based on the degenerated continuum shell theory first proposed by Ahmad [AHM 70, BAT 81, BAT 86, BOI 92], in which a specific modelling of the mechanical behaviour of fibrous material is introduced.

## 3.3 Specific plane shell element made of continuous fiber segments

### 3.3.1 Assumptions

This specific plane shell element has two nodes. Fiber segments are crossing in the element as shown in Figure 3.2 (actually there are thousands of fiber segments in the element, for visual clarity, only four fiber segments are drawn to make the illustration). These fiber segments initially are straight and parallel in the element.  $\mathbf{V}_m^k$  is the unit material director defined at each node  $k$ , which is in the direction that joins the top and bottom edge of the shell element. Two assumptions are made for the specific plane shell element based on the bending experimental results (Figure 3.1):

- A straight line in the material director direction remains straight after deformation but not necessarily remains perpendicular to the mid-surface.
- The element thickness in the direction of material director can stretch, but the element thickness along the direction of normal to the mid-surface keeps constant since it's the summation of fiber's thickness.

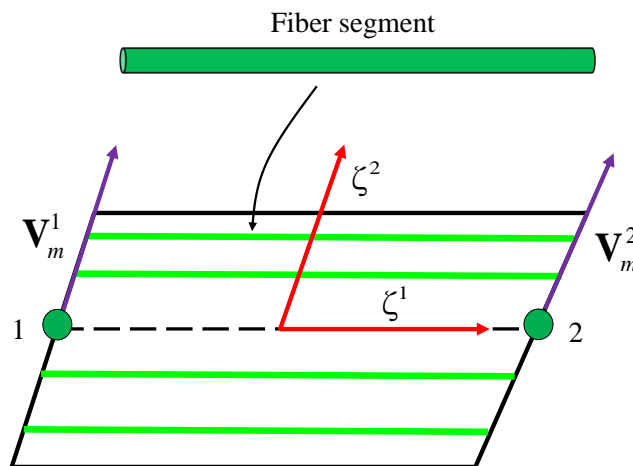


**Figure 3.2** – Specific plane shell element made of continuous fiber segments.

Element natural coordinates  $\zeta^1, \zeta^2$  are defined in the element ( $-1 \leq \zeta^1 \leq 1, -1 \leq \zeta^2 \leq 1$ ).  $\zeta^1$  is on the mid-surface,  $\zeta^2$  is along material director direction. A point with position

vector  $\mathbf{x}$  in the element gives the following covariant vectors with respect to the natural coordinates:

$$\mathbf{g}_1 = \frac{\partial \mathbf{x}}{\partial \zeta^1}, \quad \mathbf{g}_2 = \frac{\partial \mathbf{x}}{\partial \zeta^2} \quad (3.1)$$

In the present study, the material direction of fiber segment is parallel to  $\mathbf{g}_1$ .

### 3.3.2 Internal virtual work

Each fiber segment in the specific plane shell element can be taken as an Euler-Bernoulli beam. It's subjected to tensile and bending deformations. Friction exists between fibers and would have an influence on fiber's mechanical behaviour. It's not easy to determine the friction properties between fibers, since numerous factors need to be considered. In the present study, the internal energy caused by the friction can be neglected or implicitly considered and incorporated into the bending energy of fibers. In this case, the bending stiffness of fiber accounts for the influence of friction. According to the virtual work principle, the internal virtual work in the specific plane shell element is separated into two parts: the tension and bending energy of fiber segments:

$$\delta W_{\text{int}}^e = \sum_{p=1}^n \int_{L^p} (T^{11})^p (\delta \varepsilon_{11})^p dL + \sum_{p=1}^n \int_{L^p} (M^{11})^p (\delta \chi_{11})^p dL \quad (3.2)$$

Where  $\delta W_{\text{int}}^e$  denotes the elementary internal virtual work,  $(\dots)^p$  means the value of quantity  $(\dots)$  of fiber segment  $p$ ,  $n$  is the total number of fiber segments in the element,  $T^{11}$  is the tension force,  $\delta \varepsilon_{11}$  is the virtual tensile strain in the fiber segment direction,  $M^{11}$  is the moment on the fiber segment,  $\delta \chi_{11}$  is virtual curvature,  $L$  is the length of fiber segment.

### 3.3.3 Explicit dynamic approach

Generally, two classes of solution approaches are widely used in the finite element: Implicit approach and Explicit dynamic approach [BEL 13]. The former, implicit approach is widely used for the static and nonlinear stress analysis. One main disadvantage of the implicit approach is the inverse of the global structure stiffness needs to be calculated to advance the iteration, so there is a formidable challenge for computer's computing power. The Explicit dynamic approach has received increasing attention during the past two decades, particularly for the dynamic, highly non-linear and contact dominated problems. For example, car crash simulation is an application particularly well suited to this technique. Although most forming processes are quasi-static, the codes for their simulation are often based on the explicit dynamic approach which is more numerically efficient than using the implicit one. In the present study, the explicit dynamic approach will be used. The dynamic effects would be checked to make sure they are small enough that

### 3. Specific plane shell element for simulating the bending deformation of thick fibrous materials

---

not to modify results of simulation. In the following, for all the variables with a left superscript  $i$  denote the quantity obtained at time  ${}^i t$  ( $i$  is the index number of time step,  ${}^i t$  denotes the time at time setp  $i$ ).

After a finite element discretization, the dynamic motion equation can be established for each node:

$$\mathbf{M} {}^i \ddot{\mathbf{u}}_N + \mathbf{C} {}^i \dot{\mathbf{u}}_N = {}^i \mathbf{F}_{\text{ext}} - {}^i \mathbf{F}_{\text{int}} \quad (3.3)$$

Where  ${}^i \ddot{\mathbf{u}}_N$ ,  ${}^i \dot{\mathbf{u}}_N$  and  ${}^i \mathbf{u}_N$  are the single column matrix of nodal acceleration, velocity and displacements,  $\mathbf{M}$  and  $\mathbf{C}$  are the lumped mass and damping matrices,  ${}^i \mathbf{F}_{\text{int}}$  and  ${}^i \mathbf{F}_{\text{ext}}$  are the single column matrix of internal and external nodal loads.  ${}^i \mathbf{F}_{\text{int}}$  is composed of two parts in the present study: global tensile nodal loads  ${}^i \mathbf{F}_{\text{Ten-int}}$  and global bending nodal loads  ${}^i \mathbf{F}_{\text{Bend-int}}$ . Both of them are the assembly of elementary tensile nodal loads  ${}^i \mathbf{F}_{\text{Ten-int}}^e$  and elementary bending nodal loads  ${}^i \mathbf{F}_{\text{Bend-int}}^e$  on all elements. Material damping can be neglected in a short duration dynamic problems, this leads to the following equation:

$$\mathbf{M} {}^i \ddot{\mathbf{u}}_N = {}^i \mathbf{F}_{\text{ext}} - {}^i \mathbf{F}_{\text{int}} \quad (3.4)$$

Then the nodal acceleration at time  ${}^i t$  can be obtained:

$${}^i \ddot{\mathbf{u}}_N = \mathbf{M}^{-1} ({}^i \mathbf{F}_{\text{ext}} - {}^i \mathbf{F}_{\text{int}}) \quad (3.5)$$

The nodal velocities  ${}^{i+1/2} \dot{\mathbf{u}}_N$  and nodal displacements  ${}^{i+1} \mathbf{u}_N$  then can be obtained by integration in the time domain using the central finite difference operators:

$$\Delta t = {}^{i+1} t - {}^i t \quad (3.6)$$

$${}^{i+1/2} \dot{\mathbf{u}}_N = {}^{i-1/2} \dot{\mathbf{u}}_N + \frac{1}{2} (\Delta t + \Delta t^{i-1}) {}^i \ddot{\mathbf{u}}_N \quad (3.7)$$

$${}^{i+1} \mathbf{u}_N = {}^i \mathbf{u}_N + {}^{i+1/2} \dot{\mathbf{u}}_N \Delta t \quad (3.8)$$

Finally, the updated displacements are used to compute the new internal nodal loads and then the problem is advanced with a new time step. Equations (3.7) and (3.8) are conditionally stable and restrict the allowable time incremental  $\Delta t$  to less than the critical time incremental  $\Delta t_{\text{critical}}$  which is dependent on the smallest element size and materials properties [BEL 13].

#### 3.3.4 Geometry and kinematics of the specific plane shell element

The position vector of point  $M$  ( $\zeta^1, \zeta^2$ ) is defined as the summation of the position vector of its associated point of mid-surface  ${}^i \mathbf{x}(H)$  and its position  ${}^i \mathbf{y}(M)$  along the material director  ${}^i \mathbf{V}_m$  (Figure 3.3):

$${}^i \mathbf{x}(M) = {}^i \mathbf{x}(H) + {}^i \mathbf{y}(M) \quad (3.9)$$

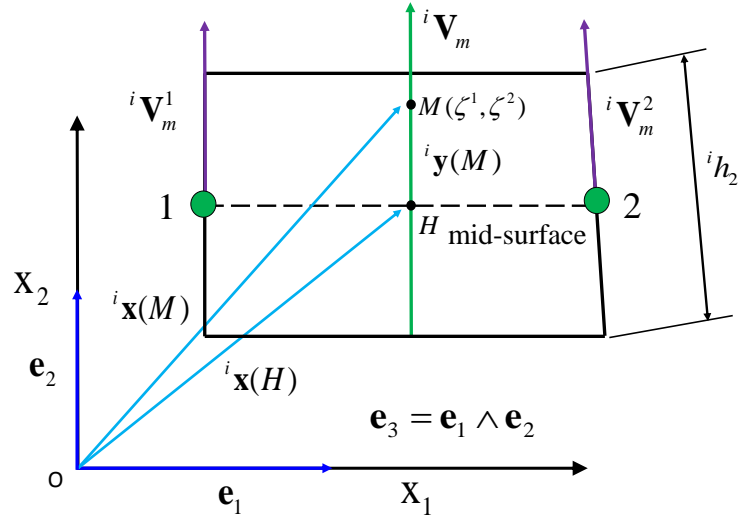


**Figure 3.3** – Geometry of the specific plane shell element at time  $t$ .

By interpolation:

$$i_{\mathbf{x}}(\zeta^1, \zeta^2) = \sum_{k=1}^2 N_k i_{\mathbf{x}_k} + \sum_{k=1}^2 N_k \left( \frac{i_{h_k} \zeta^2}{2} i_{\mathbf{V}_m^k} \right) \quad (3.10)$$

Where  $i_{\mathbf{x}_k}$  is the position vector of node  $k$ ,  $i_{h_k}$  is the element thickness along the direction of  $i_{\mathbf{V}_m^k}$  at node  $k$ ,  $\mathbf{e}_1$ ,  $\mathbf{e}_2$ ,  $\mathbf{e}_3$  are the unit global base vectors,  $N_k$  is the interpolation function of node  $k$ :

$$N_1 = \frac{1}{2} (1 - \zeta^1), \quad N_2 = \frac{1}{2} (1 + \zeta^1) \quad (3.11)$$

To guarantee the element thickness along the normal to the mid-surface keeps constant, the following constraint is imposed on the  $i_{h_k}$ :

$$i_{h_k} = \frac{h}{i_{\mathbf{V}_m^k} \cdot i_{\mathbf{n}}} \quad (3.12)$$

Where  $i_{\mathbf{n}}$  is the unit normal vector to the element mid-surface,  $h$  is the element thickness in the direction of element normal to the mid-surface and it keeps constant during the deformation. Equation (3.12) allows  $i_{h_k}$  to stretch, this is the different point compared with the general Ahmad shell element. Incremental displacement of point  $M(\zeta^1, \zeta^2)$  is:

$$\Delta \mathbf{u}(M) = {}^{i+1} \mathbf{x}(M) - i_{\mathbf{x}}(M) \quad (3.13)$$

By interpolation:

### 3. Specific plane shell element for simulating the bending deformation of thick fibrous materials

$$\Delta \mathbf{u}(\zeta^1, \zeta^2) = \sum_{k=1}^2 N_k \Delta \mathbf{u}_k + N_k \frac{\zeta^2}{2} ({}^{i+1}h_k {}^{i+1}\mathbf{V}_m^k - {}^i h_k {}^i \mathbf{V}_m^k) \quad (3.14)$$

Where  $\Delta \mathbf{u}_k$  is the incremental displacement vector of node  $k$  from time  ${}^i t$  to  ${}^{i+1} t$ . Following the fact  $\|{}^{i+1}\mathbf{V}_m^k\| = \|{}^i \mathbf{V}_m^k\| = 1$ , an orthonormal tensor  $\mathbf{R}^k$  ( $\det \mathbf{R}^k = 1$ ) is defined to transform  ${}^i \mathbf{V}_m^k$  to  ${}^{i+1}\mathbf{V}_m^k$  [BOL 79]:

$${}^{i+1}\mathbf{V}_m^k - {}^i \mathbf{V}_m^k = (\mathbf{R}_k - \mathbf{I}) {}^i \mathbf{V}_m^k \quad (3.15)$$

Where  $\mathbf{I}$  is the second order unit tensor. Assuming the rotation is small enough in the time step and calling  $\mathbf{a}_k$  is the rotation vector of node  $k$ :

$$(\mathbf{R}_k - \mathbf{I}) {}^i \mathbf{V}_m^k = \mathbf{a}_k \wedge {}^i \mathbf{V}_m^k \quad (3.16)$$

An local orthogonal frame  $({}^i \mathbf{V}_1^k, {}^i \mathbf{V}_2^k, {}^i \mathbf{V}_3^k)$  is defined at each node  $k$ , with  ${}^i \mathbf{V}_1^k = \mathbf{e}_3$ ,  ${}^i \mathbf{V}_3^k = {}^i \mathbf{V}_m^k$  (Figure 3.4), then:

$$\mathbf{a}_k = \alpha_k {}^i \mathbf{V}_1^k \quad (3.17)$$

Where  $\alpha_k$  is the rotation angle of material director  ${}^i \mathbf{V}_m^k$  around  ${}^i \mathbf{V}_1^k$  from the configuration at time  ${}^i t$  to the configuration at time  ${}^{i+1} t$ . With equation (3.17), the incremental displacement expressed in equation (3.14) finally can be approximated as:

$$\Delta \mathbf{u}(\zeta^1, \zeta^2) = \sum_{k=1}^2 N_k \Delta \mathbf{u}_k - \sum_{k=1}^2 N_k \left( \frac{\zeta^2}{2} {}^i h_k \alpha_k {}^i \mathbf{V}_2^k \right) \quad (3.18)$$

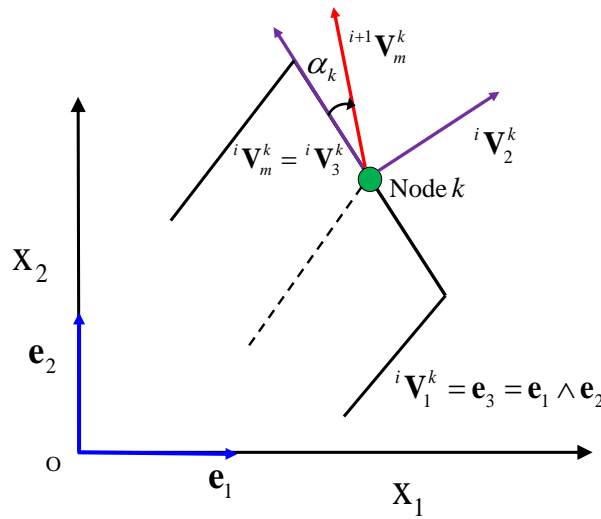


**Figure 3.4** – Definition of local orthogonal frame  $({}^i \mathbf{V}_1^k, {}^i \mathbf{V}_2^k, {}^i \mathbf{V}_3^k)$ .

Another thing should pay attention: the normal vector to the element mid-surface is not continuous at the junction node of two elements due to the element interpolation is  $C^0$  continuous (Figure 3.5). For a junction node  $k$ , the element thickness in the material director direction is computed as following to meet the continuous and unique requirements:

$${}^i h_k = \frac{1}{2} \left( \frac{h}{{}^i \mathbf{V}_m^k \cdot {}^i \mathbf{n}_1} + \frac{h}{{}^i \mathbf{V}_m^k \cdot {}^i \mathbf{n}_2} \right) \quad (3.19)$$

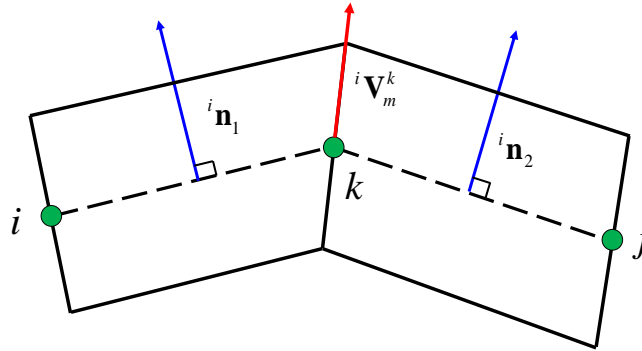


**Figure 3.5** – Thickness modelling for the junction node of two elements.

### 3.3.5 Strategies to characterize tensile and bending deformations for fiber segments in the element

The specific plane shell element is using linear interpolation ( $C^0$  continuous). The positions of endpoints of fiber segments come from the element interpolation. In the present study, fiber segment initially is assumed straight and parallel with element edge, after deformation it would remain straight in the element if it's interpolated by the element interpolation. This assumption and its consequence on tensile characterization would be discussed below. A local curve  $w$  is constructed from the endpoints of any three adjacent fiber segments after deformation (Figure 3.6). The positions of fiber endpoints can be written in terms of nodal positions.  $l$  is the length of geometry straight segment  $f1 - f2$  and  $L$  is the length of the local curve  $w$  between fiber endpoints  $f1$  and  $f2$ . To characterize tensile deformation for fiber segment  $f1 - f2$ , two options are available:

- Fiber segment  $f1 - f2$  after deformation remains straight and is coincident with the geometry straight segment  $f1 - f2$ . This is the most direct and simple way to characterize the tensile deformation for fiber segment, since its length  $l$  can be directly obtained from the element interpolation. However, from the experiment observation (Figure 3.1), fiber segments after deformation are a curve shape not a straight one. Since fiber's tensile deformation is very sensitive due to its high tensile stiffness, it should characterize tensile strain as accurate as possible. This leads to the following second option to characterize tensile strain.

### 3. Specific plane shell element for simulating the bending deformation of thick fibrous materials

- Fiber segment  $f1 - f2$  after deformation is seen as the local curve  $w$  that between fiber endpoints  $f1$  and  $f2$  and its length is  $L$ . By this way, it makes the possibility of fiber segment  $f1 - f2$  stay quasi-inextensible. For the material direction of fiber segment  $f1 - f2$ , strictly speaking, it should be in the tangent direction of the local curve  $w$ , here simplification has been made and it's assumed it's in the direction of the geometry straight segment  $f1 - f2$ .

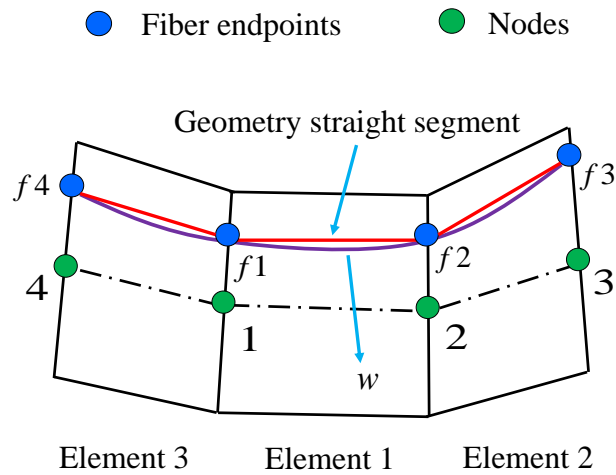


**Figure 3.6** – The local curve represented by the endpoints of three adjacent fiber segments.

Curve length  $L$  allows more accurately to characterize tensile deformation for fiber segment than using  $l$ , particularly when the mesh is coarse and bending deformation is large, there would have a great difference between using  $L$  and  $l$  to characterize the tensile strain. Consequently, in the present study, we would adopt the curve length  $L$  to characterize the tensile deformation for fiber segment  $f1 - f2$ .

To characterize the bending deformation for fiber segment  $f1 - f2$ , one important parameter is its curvature. The curvature of fiber segment  $f1 - f2$  is not directly related to the first derivative of rotation angle of material director (this point has already been indicated in Figure 3.1), it would be calculated from the local curve  $w$ , where the curvature equals the second derivative of  $w$ . Other fiber segments would employ the same method as fiber segment  $f1 - f2$  to characterize tensile and bending deformations.

#### 3.3.6 Construction of the local curve

At time  ${}^i t$ , three geometry straight segments composed by the endpoints of three adjacent fiber segments are shown in Figure 3.7 and their configuration is  $f4 - f1 - f2 - f3$ . A co-rotated Cartesian frame  $x - y$  is defined, in which the  $x$  axis coincides with the straight segment  $f1 - f2$ , the origin is at fiber endpoint  $f1$ . When imposed an incremental displacement  $\Delta \mathbf{u}$ , their deformed configuration at time  ${}^{i+1} t$  is  $F4 - F1 - F2 - F3$ . In the co-rotated

Cartesian frame  $x - y$ , the configuration  $f4 - f1 - f2 - f3$  is interpolated by a cubic order polynomial curve  ${}^i w$ :

$${}^i w = ax^3 + bx^2 + cx + d \quad (3.20)$$

The coefficients  $a, b, c, d$  in equation (3.20) can be solved by the following boundary conditions:

$${}^i w(x = -{}^i l_3) \approx -{}^i \varphi_1 {}^i l_3, \quad {}^i w(x = 0) = {}^i w(x = {}^i l_1) = 0, \quad {}^i w(x = {}^i l_1 + {}^i l_2) \approx {}^i \varphi_2 {}^i l_2 \quad (3.21)$$

Where  ${}^i l_1, {}^i l_2, {}^i l_3$  are respectively the length of geometry segments  $f1 - f2, f2 - f3$  and  $f4 - f1$ ,  ${}^i \varphi_1$  and  ${}^i \varphi_2$  are called relative angles of fiber endpoints  $f1$  and  $f2$  (Figure 3.7). Relative angle denotes the angle between two adjacent geometry straight segments. They are assumed small and this assumption can be met by confining element size. Angle in the counterclockwise direction is defined as positive in this thesis.

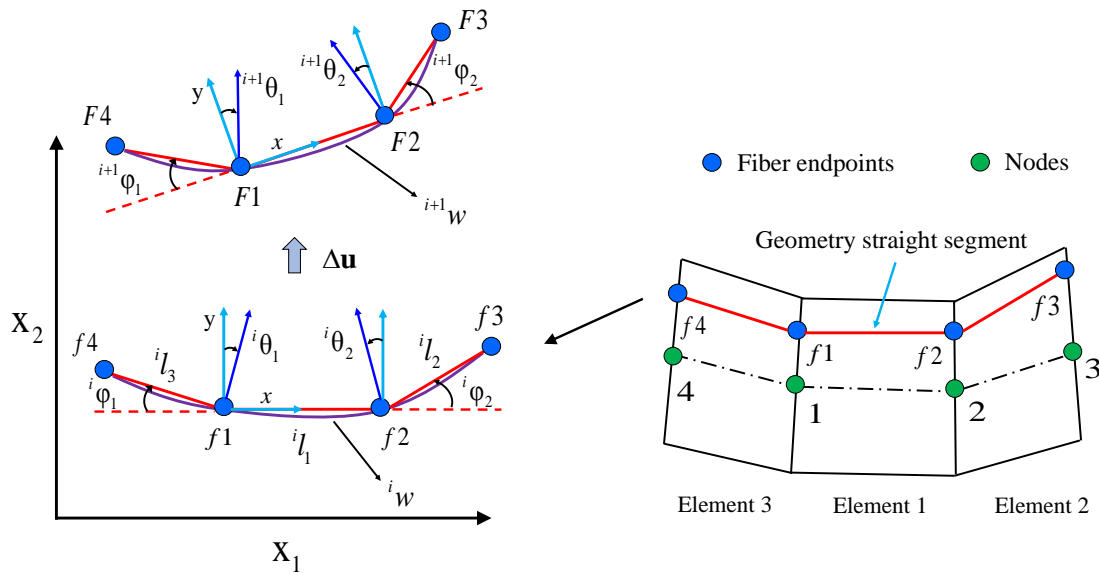


**Figure 3.7** – The interpolation of the local curve represented by the endpoints of three adjacent fiber segments.

As shown in Figure 3.7,  ${}^i \theta_1$  and  ${}^i \theta_2$  are called rotation angles of fiber endpoints  $f1$  and  $f2$ . Rotation angle denotes the inclination angle of the normal vector of local curve  ${}^i w$  with respect to the local co-rotated  $y$  axis. When the curve function  ${}^i w$  is obtained with the boundary equation (3.21),  ${}^i \theta_1$  and  ${}^i \theta_2$  can be calculated as following:

$$\begin{aligned} {}^i \theta_1 &\approx \tan {}^i \theta_1 = \frac{\partial {}^i w}{\partial x}(x = 0) = \frac{{}^i l_1({}^i l_1 + {}^i l_2)}{({}^i l_1 + {}^i l_3)({}^i l_1 + {}^i l_2 + {}^i l_3)} {}^i \varphi_1 + \frac{-{}^i l_1 {}^i l_3}{({}^i l_1 + {}^i l_2)({}^i l_1 + {}^i l_2 + {}^i l_3)} {}^i \varphi_2 \\ &= {}^i A_1 {}^i \varphi_1 + {}^i A_2 {}^i \varphi_2 \end{aligned} \quad (3.22)$$

### 3. Specific plane shell element for simulating the bending deformation of thick fibrous materials

---

$$\begin{aligned} {}^i\theta_2 &\approx \tan {}^i\theta_2 = \frac{\partial {}^i w}{\partial x}(x = {}^i l_1) = \frac{-{}^i l_1 {}^i l_2}{({}^i l_1 + {}^i l_3)({}^i l_1 + {}^i l_2 + {}^i l_3)} {}^i\varphi_1 + \frac{{}^i l_1({}^i l_1 + {}^i l_3)}{({}^i l_1 + {}^i l_2)({}^i l_1 + {}^i l_2 + {}^i l_3)} {}^i\varphi_2 \\ &= {}^i A_3 {}^i\varphi_1 + {}^i A_4 {}^i\varphi_2 \end{aligned} \quad (3.23)$$

Written in matrix form for equation (3.22) and (3.23):

$$\begin{bmatrix} {}^i\theta_1 \\ {}^i\theta_2 \end{bmatrix} = \begin{bmatrix} {}^i A_1 & {}^i A_2 \\ {}^i A_3 & {}^i A_4 \end{bmatrix} \begin{bmatrix} {}^i\varphi_1 \\ {}^i\varphi_2 \end{bmatrix} \quad (3.24)$$

Equation (3.24) gives the relation between the rotation angles of fiber endpoints and relative angles. In order to correct the approximation made in equation (3.21), (3.22) and (3.23), the value of coefficients  ${}^i A_j$  ( $j = 1, 2, 3, 4$ ) in the equation (3.24) can be amended according to Jean-marc Battini [BAT 08]. He has found the following amended value of  ${}^i A_j$  works best for his rotation free beam element in the simulation and in the present work we would adopt these values:

$$\begin{aligned} {}^i A_1 &= \frac{2}{3} \frac{{}^i l_1}{{}^i l_1 + {}^i l_3} + \frac{1}{3} \frac{{}^i l_1({}^i l_1 + {}^i l_2)}{({}^i l_1 + {}^i l_3)({}^i l_1 + {}^i l_2 + {}^i l_3)} \\ {}^i A_2 &= -\frac{1}{3} \frac{{}^i l_3}{({}^i l_1 + {}^i l_2)({}^i l_1 + {}^i l_2 + {}^i l_3)} \\ {}^i A_3 &= -\frac{1}{3} \frac{{}^i l_1 {}^i l_2}{({}^i l_1 + {}^i l_3)({}^i l_1 + {}^i l_2 + {}^i l_3)} \\ {}^i A_4 &= \frac{2}{3} \frac{{}^i l_1}{{}^i l_1 + {}^i l_2} + \frac{1}{3} \frac{{}^i l_1({}^i l_1 + {}^i l_3)}{({}^i l_1 + {}^i l_2)({}^i l_1 + {}^i l_2 + {}^i l_3)} \end{aligned} \quad (3.25)$$

Finally, the curve function for the curve  ${}^i w$  that between fiber endpoints  $f1$  and  $f2$  can be expressed in terms of  ${}^i\theta_1$  and  ${}^i\theta_2$  instead of using the function form in equation (3.20) (this is called Hermite interpolation):

$${}^i w = x(1 - \frac{x}{{}^i l_1})^2 {}^i\theta_1 + \frac{(x)^2}{{}^i l_1} (\frac{x}{{}^i l_1} - 1) {}^i\theta_2 \quad (0 \leq x \leq {}^i l_1) \quad (3.26)$$

Using the same derivation process as for curve  ${}^i w$ , the deformed configuration  $F4 - F1 - F2 - F3$  is also interpolated by a cubic order polynomial  ${}^{i+1}w$  in the co-rotated Cartesian frame  $x - y$ , we can get the rotation angles  ${}^{i+1}\theta_1$  and  ${}^{i+1}\theta_2$  at fiber endpoints  $F1$  and  $F2$  for the local curve  ${}^{i+1}w$  in the co-rotated frame  $x - y$ :

$$\begin{bmatrix} {}^{i+1}\theta_1 \\ {}^{i+1}\theta_2 \end{bmatrix} = \begin{bmatrix} \frac{\partial {}^{i+1}w}{\partial x}(x = 0) \\ \frac{\partial {}^{i+1}w}{\partial x}(x = {}^{i+1}l_1) \end{bmatrix} = \begin{bmatrix} {}^{i+1}A_1 & {}^{i+1}A_2 \\ {}^{i+1}A_3 & {}^{i+1}A_4 \end{bmatrix} \begin{bmatrix} {}^{i+1}\varphi_1 \\ {}^{i+1}\varphi_2 \end{bmatrix} \quad (3.27)$$

With:

$$\begin{aligned}
 {}^{i+1}A_1 &= \frac{2}{3} \frac{{}^{i+1}l_1}{{}^{i+1}l_1 + {}^{i+1}l_3} + \frac{1}{3} \frac{{}^{i+1}l_1({}^{i+1}l_1 + {}^{i+1}l_2)}{({}^{i+1}l_1 + {}^{i+1}l_3)({}^{i+1}l_1 + {}^{i+1}l_2 + {}^{i+1}l_3)} \\
 {}^{i+1}A_2 &= -\frac{1}{3} \frac{{}^{i+1}l_3}{{}^{i+1}l_1 + {}^{i+1}l_2} \frac{1}{{}^{i+1}l_1 + {}^{i+1}l_2 + {}^{i+1}l_3} \\
 {}^{i+1}A_3 &= -\frac{1}{3} \frac{{}^{i+1}l_1 {}^{i+1}l_2}{{}^{i+1}l_1 + {}^{i+1}l_3} \frac{1}{{}^{i+1}l_1 + {}^{i+1}l_2 + {}^{i+1}l_3} \\
 {}^{i+1}A_4 &= \frac{2}{3} \frac{{}^{i+1}l_1}{{}^{i+1}l_1 + {}^{i+1}l_2} + \frac{1}{3} \frac{{}^{i+1}l_1({}^{i+1}l_1 + {}^{i+1}l_3)}{({}^{i+1}l_1 + {}^{i+1}l_2)({}^{i+1}l_1 + {}^{i+1}l_2 + {}^{i+1}l_3)}
 \end{aligned} \tag{3.28}$$

Where  ${}^{i+1}l_1$ ,  ${}^{i+1}l_2$  and  ${}^{i+1}l_3$  are respectively the length of the geometry straight segments  $F1 - F2$ ,  $F2 - F3$  and  $F4 - F1$ ,  ${}^{i+1}\varphi_1$  and  ${}^{i+1}\varphi_2$  are the relative angles of fiber endpoints  $F1$  and  $F2$ , they can be decomposed as following:

$$\begin{bmatrix} {}^{i+1}\varphi_1 \\ {}^{i+1}\varphi_2 \end{bmatrix} = \begin{bmatrix} {}^i\varphi_1 \\ {}^i\varphi_2 \end{bmatrix} + \begin{bmatrix} \Delta\varphi_1 \\ \Delta\varphi_2 \end{bmatrix} \tag{3.29}$$

Where  $\Delta\varphi_1$  and  $\Delta\varphi_2$  are called incremental relative angles due to the incremental displacements, since the incremental displacements are assumed very small,  $\Delta\varphi_1$  and  $\Delta\varphi_2$  can be calculated as following [GUO 02, SAB 06] (seen in Appendix A.2):

$$\begin{bmatrix} \Delta\varphi_1 \\ \Delta\varphi_2 \end{bmatrix} = \begin{bmatrix} -\frac{\Delta\bar{\mathbf{u}}_4^f \cdot {}^i\bar{\mathbf{n}}_3 - \Delta\bar{\mathbf{u}}_1^f \cdot {}^i\bar{\mathbf{n}}_3}{i_3} - \frac{\Delta\bar{\mathbf{u}}_2^f \cdot {}^i\bar{\mathbf{n}}_1 - \Delta\bar{\mathbf{u}}_1^f \cdot {}^i\bar{\mathbf{n}}_1}{i_1} \\ \frac{\Delta\bar{\mathbf{u}}_3^f \cdot {}^i\bar{\mathbf{n}}_2 - \Delta\bar{\mathbf{u}}_2^f \cdot {}^i\bar{\mathbf{n}}_2}{i_2} - \frac{\Delta\bar{\mathbf{u}}_2^f \cdot {}^i\bar{\mathbf{n}}_1 - \Delta\bar{\mathbf{u}}_1^f \cdot {}^i\bar{\mathbf{n}}_1}{i_1} \end{bmatrix} = \mathbf{G}\Delta\mathbf{u}^f \tag{3.30}$$

With:

$$\mathbf{G} = \begin{bmatrix} G_{11} & G_{12} & G_{13} & G_{14} & G_{15} & G_{16} & G_{17} & G_{18} \\ G_{21} & G_{22} & G_{23} & G_{24} & G_{25} & G_{26} & G_{27} & G_{28} \end{bmatrix}$$

$$\Delta\mathbf{u}^f = \begin{bmatrix} \Delta\bar{u}_{11}^f & \Delta\bar{u}_{12}^f & \Delta\bar{u}_{21}^f & \Delta\bar{u}_{22}^f & \Delta\bar{u}_{31}^f & \Delta\bar{u}_{32}^f & \Delta\bar{u}_{41}^f & \Delta\bar{u}_{42}^f \end{bmatrix}^T \tag{3.31}$$

Where  ${}^i\bar{\mathbf{n}}_1$ ,  ${}^i\bar{\mathbf{n}}_2$  and  ${}^i\bar{\mathbf{n}}_3$  are the unit normal vectors to the geometry straight segments  $f1 - f2$ ,  $f2 - f3$  and  $f4 - f1$  respectively (Figure 3.7),  $\Delta\bar{\mathbf{u}}_j^f$  is the incremental displacement vector of fiber endpoint  $fj$  ( $j = 1, 2, 3, 4$ ),  $\Delta\mathbf{u}^f$  is the single column matrix of the incremental displacements of fiber endpoints, in which  $\Delta\bar{u}_{js}^f$  denotes the  $s$ th global component of  $\Delta\bar{\mathbf{u}}_j^f$ . The incremental displacements of fiber endpoints can be written in terms of incremental nodal displacements and rotations based on the displacement interpolation equation (3.18):

$$\Delta\mathbf{u}^f = \mathbf{H}\Delta\mathbf{u}^n \tag{3.32}$$

### 3. Specific plane shell element for simulating the bending deformation of thick fibrous materials

With:

$$\mathbf{H} = \begin{pmatrix} 1 & 0 & -\frac{i h_1 \zeta^2}{2} (i \mathbf{V}_2^1 \cdot \mathbf{e}_1) & 0 & 0 & 0 & 0 & 0 & 0 & 0 & 0 \\ 0 & 1 & -\frac{i h_1 \zeta^2}{2} (i \mathbf{V}_2^1 \cdot \mathbf{e}_2) & 0 & 0 & 0 & 0 & 0 & 0 & 0 & 0 \\ 0 & 0 & 0 & 1 & 0 & -\frac{i h_2 \zeta^2}{2} (i \mathbf{V}_2^2 \cdot \mathbf{e}_1) & 0 & 0 & 0 & 0 & 0 \\ 0 & 0 & 0 & 0 & 1 & -\frac{i h_2 \zeta^2}{2} (i \mathbf{V}_2^2 \cdot \mathbf{e}_2) & 0 & 0 & 0 & 0 & 0 \\ 0 & 0 & 0 & 0 & 0 & 0 & 1 & 0 & -\frac{i h_3 \zeta^2}{2} (i \mathbf{V}_2^3 \cdot \mathbf{e}_1) & 0 & 0 \\ 0 & 0 & 0 & 0 & 0 & 0 & 0 & 1 & -\frac{i h_3 \zeta^2}{2} (i \mathbf{V}_2^3 \cdot \mathbf{e}_2) & 0 & 0 \\ 0 & 0 & 0 & 0 & 0 & 0 & 0 & 0 & 0 & 1 & 0 \\ 0 & 0 & 0 & 0 & 0 & 0 & 0 & 0 & 0 & 0 & 1 \end{pmatrix} \begin{matrix} -\frac{i h_4 \zeta^2}{2} (i \mathbf{V}_2^4 \cdot \mathbf{e}_1) \\ -\frac{i h_4 \zeta^2}{2} (i \mathbf{V}_2^4 \cdot \mathbf{e}_2) \end{matrix}$$

$$\Delta \mathbf{u}^n = \left[ \Delta u_{11} \quad \Delta u_{12} \quad \alpha_1 \quad \Delta u_{21} \quad \Delta u_{22} \quad \alpha_2 \quad \Delta u_{31} \quad \Delta u_{32} \quad \alpha_3 \quad \Delta u_{41} \quad \Delta u_{42} \quad \alpha_4 \right]^T \quad (3.33)$$

Where  $\mathbf{H}$  is the transformation matrix between the incremental displacements of fiber endpoints and the incremental nodal displacements and rotations,  $\Delta \mathbf{u}^n$  is the single column matrix of incremental nodal displacements and rotations of three adjacent elements, in which  $\Delta u_{kj}$  is the  $j$ th global component of  $\Delta \mathbf{u}_k$ , others have the same meaning as defined previously. In the present study, the endpoints of any three adjacent fiber segments have the same value  $\zeta^2$ , the meaning of these index numbers are shown in Figure 3.7.

Taking equation (3.32) into equation (3.30), the incremental relative angles  $\Delta \phi_1$  and  $\Delta \phi_2$  can be expressed in terms of incremental nodal displacements and rotations:

$$\begin{bmatrix} \Delta \phi_1 \\ \Delta \phi_2 \end{bmatrix} = \mathbf{G} \Delta \mathbf{u}^f = \mathbf{G} \mathbf{H} \Delta \mathbf{u}^n = \mathbf{Q} \Delta \mathbf{u}^n \quad (3.34)$$

Where  $\mathbf{Q} = \mathbf{G} \mathbf{H}$  is called the transformation matrix between the incremental relative angles of fiber endpoints and the incremental nodal displacements and rotations. With the equation (3.24) and (3.27), we can obtain the incremental rotation angles  $\Delta \theta_1$  and  $\Delta \theta_2$  at fiber endpoints  $f1$  and  $f2$  due to the incremental displacement  $\Delta \mathbf{u}$ :

$$\begin{bmatrix} \Delta \theta_1 \\ \Delta \theta_2 \end{bmatrix} = \begin{bmatrix} {}^{i+1} \theta_1 \\ {}^{i+1} \theta_2 \end{bmatrix} - \begin{bmatrix} {}^i \theta_1 \\ {}^i \theta_2 \end{bmatrix} = \begin{bmatrix} {}^{i+1} A_1 & {}^{i+1} A_2 \\ {}^{i+1} A_3 & {}^{i+1} A_4 \end{bmatrix} \begin{bmatrix} {}^{i+1} \phi_1 \\ {}^{i+1} \phi_2 \end{bmatrix} - \begin{bmatrix} {}^i A_1 & {}^i A_2 \\ {}^i A_3 & {}^i A_4 \end{bmatrix} \begin{bmatrix} {}^i \phi_1 \\ {}^i \phi_2 \end{bmatrix} \quad (3.35)$$

The incremental displacement  $\Delta \mathbf{u}$  is assumed small in the time step, the influence of geometry straight segment's extension on the incremental rotation angle of fiber endpoint can be neglected [GUO 02, SAB 06], we can postulate:

$${}^{i+1} A_1 \approx {}^i A_1, \quad {}^{i+1} A_2 \approx {}^i A_2, \quad {}^{i+1} A_3 \approx {}^i A_3, \quad {}^{i+1} A_4 \approx {}^i A_4 \quad (3.36)$$

Substituting equation (3.36) into (3.35) and with equation (3.29), the incremental rotation angles are:

$$\begin{bmatrix} \Delta\theta_1 \\ \Delta\theta_2 \end{bmatrix} = \begin{bmatrix} {}^iA_1 & {}^iA_2 \\ {}^iA_3 & {}^iA_4 \end{bmatrix} \begin{bmatrix} {}^{i+1}\varphi_1 - {}^i\varphi_1 \\ {}^{i+1}\varphi_2 - {}^i\varphi_2 \end{bmatrix} = \mathbf{A} \begin{bmatrix} \Delta\varphi_1 \\ \Delta\varphi_2 \end{bmatrix} = \mathbf{A}\mathbf{Q}\Delta\mathbf{u}^n = \mathbf{T}\Delta\mathbf{u}^n \quad (3.37)$$

Where  $\mathbf{T} = \mathbf{A}\mathbf{Q}$  is called the transformation matrix between the incremental rotation angles of fiber endpoints and the incremental nodal displacements and rotations.

Finally, the curve function for the curve  ${}^{i+1}w$  that between fiber endpoints  $F1$  and  $F2$  can also be written in terms of  ${}^{i+1}\theta_1$  and  ${}^{i+1}\theta_2$  (this is called Hermite interpolation):

$$\begin{aligned} {}^{i+1}w &= x\left(1 - \frac{x}{{}^{i+1}l_1}\right)^2 {}^{i+1}\theta_1 + \frac{(x)^2}{{}^{i+1}l_1} \left(\frac{x}{{}^{i+1}l_1} - 1\right) {}^{i+1}\theta_2 \\ &= x\left(1 - \frac{x}{{}^{i+1}l_1}\right)^2 ({}^i\theta_1 + \Delta\theta_1) + \frac{(x)^2}{{}^{i+1}l_1} \left(\frac{x}{{}^{i+1}l_1} - 1\right) ({}^i\theta_2 + \Delta\theta_2) \quad (0 \leq x \leq {}^{i+1}l_1) \end{aligned} \quad (3.38)$$

### 3.3.7 Elementary tensile nodal loads

At time  ${}^it$ , a virtual incremental displacement  $\delta\mathbf{u}$  is imposed, then the corresponding virtual incremental rotation angles of fiber endpoints  $f1$  and  $f2$  can be obtained according to equation (3.37):

$$\begin{bmatrix} \delta\theta_1 \\ \delta\theta_2 \end{bmatrix} = \mathbf{T}\delta\mathbf{u}^n \quad (3.39)$$

The curve function that between fiber endpoints  $f1$  and  $f2$  after the virtual displacement  $\delta\mathbf{u}$  is called  ${}^iw^*$ . According to equation (3.38),  ${}^iw^*$  can be expressed as:

$${}^iw^* = x\left(1 - \frac{x}{l_1 + \delta^i l_1}\right)^2 ({}^i\theta_1 + \delta\theta_1) + \frac{x^2}{l_1 + \delta^i l_1} \left(\frac{x}{l_1 + \delta^i l_1} - 1\right) ({}^i\theta_2 + \delta\theta_2) \quad (0 \leq x \leq l_1 + \delta^i l_1) \quad (3.40)$$

Where  $\delta^i l_1$  is virtual length extension of geometry straight segment  $f1 - f2$ .

The length for the local curve  ${}^iw$  that between fiber endpoints  $f1$  and  $f2$  is:

$${}^iL = \int_0^{l_1} \left(1 + \left(\frac{d^i w}{dx}\right)^2\right)^{0.5} dx \quad (3.41)$$

With:

$$\frac{d^i w}{dx} = \left(1 + \frac{3x^2}{(l_1)^2} - \frac{4x}{l_1}\right) {}^i\theta_1 + \left(\frac{3x^2}{(l_1)^2} - \frac{2x}{l_1}\right) {}^i\theta_2 \quad (3.42)$$

Using one Gauss point to integrate in equation (3.41), we can obtain the length  ${}^iL$ :

$${}^iL = l_1 \sqrt{1 + \frac{1}{16} ({}^i\theta_1 + {}^i\theta_2)^2} \quad (3.43)$$

### 3. Specific plane shell element for simulating the bending deformation of thick fibrous materials

---

Applying the same manner, the length of virtual local curve  ${}^i w^*$  is  ${}^i L^*$  and can be obtained as following:

$${}^i L^* = ({}^i l_1 + \delta^i l_1) \sqrt{1 + \frac{1}{16} ({}^i \theta_1 + \delta \theta_1 + {}^i \theta_2 + \delta \theta_2)^2} \quad (3.44)$$

The virtual tensile strain for fiber segment  $f1 - f2$  at time  ${}^i t$  is:

$$\delta \epsilon_{11} = \frac{{}^i L^* - {}^i L}{{}^i L} \approx \frac{({}^i L^*)^2 - ({}^i L)^2}{2({}^i L)^2} \quad (3.45)$$

Substituting equation (3.43) and (3.44) into equation (3.45) and make the linerization:

$$\begin{aligned} \delta \epsilon_{11} &= \frac{\delta^i l_1}{{}^i l_1} + \frac{1}{(1 + \frac{1}{16} ({}^i \theta_1 + {}^i \theta_2)^2)} \left[ \frac{1}{16} {}^i \theta_1 + \frac{1}{16} {}^i \theta_2 \quad \frac{1}{16} {}^i \theta_1 + \frac{1}{16} {}^i \theta_2 \right] \begin{bmatrix} \delta \theta_1 \\ \delta \theta_2 \end{bmatrix} \\ &= \delta \epsilon_{11}^1 + \delta \epsilon_{11}^2 \end{aligned} \quad (3.46)$$

The meaning of the two parts of the virtual strain in equation (3.46) can be illustrated as follows:

- $\delta \epsilon_{11}^1 = \frac{\delta^i l_1}{{}^i l_1}$  denotes the virtual tensile strain for the geometry straight segment  $f1 - f2$ , for which its length is directly calculated from the element interpolation, so:

$$\delta \epsilon_{11}^1 = \frac{\delta^i l_1}{{}^i l_1} = \frac{{}^i \mathbf{g}_1}{\|{}^i \mathbf{g}_1\|} \cdot \nabla (\delta \mathbf{u}) \cdot \frac{{}^i \mathbf{g}_1}{\|{}^i \mathbf{g}_1\|} = {}^i \mathbf{B}^{Ten-1} \delta \mathbf{u}^e \quad (3.47)$$

With:

$$\delta \mathbf{u}^e = \begin{bmatrix} \delta u_{11} & \delta u_{12} & \delta \alpha_1 & \delta u_{21} & \delta u_{22} & \delta \alpha_2 \end{bmatrix}^T \quad (3.48)$$

Where  ${}^i \mathbf{g}_1$  is in the direction of geometry straight segment  $f1 - f2$ ,  $\delta \mathbf{u}^e$  is the single column matrix of virtual incremental nodal displacements and rotations of the element where fiber segment  $f1 - f2$  locates.  ${}^i \mathbf{B}^{Ten-1} = \begin{bmatrix} \mathbf{B}_1^{Ten-1} & \mathbf{B}_2^{Ten-1} & \mathbf{B}_3^{Ten-1} & \mathbf{B}_4^{Ten-1} & \mathbf{B}_5^{Ten-1} & \mathbf{B}_6^{Ten-1} \end{bmatrix}^T$  and its components are

as following:

$$\begin{aligned}
 \mathbf{B}_1^{Ten-1} &= \frac{1}{\|{}^i\mathbf{g}_1\|^2} \frac{\partial N_1}{\partial \zeta^1} \mathbf{e}_1 \cdot {}^i\mathbf{g}_1 \\
 \mathbf{B}_2^{Ten-1} &= \frac{1}{\|{}^i\mathbf{g}_1\|^2} \frac{\partial N_1}{\partial \zeta^1} \mathbf{e}_2 \cdot {}^i\mathbf{g}_1 \\
 \mathbf{B}_3^{Ten-1} &= -\frac{1}{\|{}^i\mathbf{g}_1\|^2} \left( \left( \frac{{}^i h_1 \zeta^2}{2} \frac{\partial N_1}{\partial \zeta^1} \right) \mathbf{e}_1 \cdot {}^i\mathbf{V}_2^1 \right) \mathbf{e}_1 \cdot {}^i\mathbf{g}_1 - \frac{1}{\|{}^i\mathbf{g}_1\|^2} \left( \left( \frac{{}^i h_1 \zeta^2}{2} \frac{\partial N_1}{\partial \zeta^1} \right) \mathbf{e}_2 \cdot {}^i\mathbf{V}_2^1 \right) \mathbf{e}_2 \cdot {}^i\mathbf{g}_1 \\
 \mathbf{B}_4^{Ten-1} &= \frac{1}{\|{}^i\mathbf{g}_1\|^2} \frac{\partial N_2}{\partial \zeta^1} \mathbf{e}_1 \cdot {}^i\mathbf{g}_1 \\
 \mathbf{B}_5^{Ten-1} &= \frac{1}{\|{}^i\mathbf{g}_1\|^2} \frac{\partial N_2}{\partial \zeta^1} \mathbf{e}_2 \cdot {}^i\mathbf{g}_1 \\
 \mathbf{B}_6^{Ten-1} &= -\frac{1}{\|{}^i\mathbf{g}_1\|^2} \left( \left( \frac{{}^i h_2 \zeta^2}{2} \frac{\partial N_2}{\partial \zeta^1} \right) \mathbf{e}_1 \cdot {}^i\mathbf{V}_2^2 \right) \mathbf{e}_1 \cdot {}^i\mathbf{g}_1 - \frac{1}{\|{}^i\mathbf{g}_1\|^2} \left( \left( \frac{{}^i h_2 \zeta^2}{2} \frac{\partial N_2}{\partial \zeta^1} \right) \mathbf{e}_2 \cdot {}^i\mathbf{V}_2^2 \right) \mathbf{e}_2 \cdot {}^i\mathbf{g}_1
 \end{aligned} \tag{3.49}$$

- $\delta \boldsymbol{\varepsilon}_{11}^2 = \frac{1}{\left(1 + \frac{1}{16}({}^i\theta_1 + {}^i\theta_2)^2\right)} \begin{bmatrix} \frac{1}{16}{}^i\theta_1 + \frac{1}{16}{}^i\theta_2 & \frac{1}{16}{}^i\theta_1 + \frac{1}{16}{}^i\theta_2 \end{bmatrix} \begin{bmatrix} \delta\theta_1 \\ \delta\theta_2 \end{bmatrix}$  is the extra virtual tensile strain contributed by taking fiber segment as a curve after deformation, with equation (3.39):

$$\delta \boldsymbol{\varepsilon}_{11}^2 = \mathbf{S} \begin{pmatrix} \delta\theta_1 \\ \delta\theta_2 \end{pmatrix} = \mathbf{S} \mathbf{T} \delta \mathbf{u}^n = {}^i\mathbf{B}^{Ten-2} \delta \mathbf{u}^n \tag{3.50}$$

Where:

$$\mathbf{S} = \frac{1}{\left(1 + \frac{1}{16}({}^i\theta_1 + {}^i\theta_2)^2\right)} \begin{bmatrix} \frac{1}{16}{}^i\theta_1 + \frac{1}{16}{}^i\theta_2 & \frac{1}{16}{}^i\theta_1 + \frac{1}{16}{}^i\theta_2 \end{bmatrix} \tag{3.51}$$

Finally, Substituting equation (3.47) and (3.50) into (3.46), the virtual tensile strain for fiber segment  $f1 - f2$  in the fiber segment direction is:

$$\delta \boldsymbol{\varepsilon}_{11} = {}^i\mathbf{B}^{Ten-1} \delta \mathbf{u}^e + {}^i\mathbf{B}^{Ten-2} \delta \mathbf{u}^n = {}^i\mathbf{B}^{Ten} \delta \mathbf{u}^n \tag{3.52}$$

Where  ${}^i\mathbf{B}^{Ten}$  is the Strain-displacement matrix for tension at time  ${}^i t$ .

The elementary tensile nodal loads at time  ${}^i t$  are given as:

$${}^i\mathbf{F}_{Ten-int}^e = \sum_{p=1}^n \int_{({}^i L)^p} \left( ({}^i\mathbf{B}^{Ten})^p \right)^T ({}^i T^{11})^p dL \tag{3.53}$$

### 3.3.8 Fiber segment tension force update

The explicit dynamic scheme in equation (3.8) gives the nodal displacement at time  ${}^{i+1}t$ , the tension force of fiber segment  $({}^{i+1}T^{11})^p$  at time  ${}^{i+1}t$  can be updated using the following equations in order to perform the next time step iteration:

$$({}^{i+1}T^{11})^p = ({}^iT^{11})^p + (\Delta T^{11})^p \quad (3.54)$$

With:

$$(\Delta T^{11})^p = C \frac{({}^{i+1}L)^p - ({}^iL)^p}{({}^iL)^p} \quad (3.55)$$

Where  $C$  is the tensile stiffness of fiber and is assumed constant during the deformation.

### 3.3.9 Elementary bending nodal loads

At time  ${}^it$ , due to the virtual incremental displacement  $\delta \mathbf{u}$ , the virtual incremental curvature  $\delta \chi_{11}$  can be obtained for fiber segment  $f1 - f2$  (assuming  ${}^il_1 \approx {}^il_1 + \delta {}^il_1$ ):

$$\delta \chi_{11} = -\frac{\partial^2({}^iw^*)}{\partial x^2} - \left(-\frac{\partial^2({}^iw)}{\partial x^2}\right) = \left(\frac{4}{{}^il_1} - 6\frac{x}{({}^il_1)^2}\right) \delta \theta_1 + \left(\frac{2}{{}^il_1} - 6\frac{x}{({}^il_1)^2}\right) \delta \theta_2 \quad (0 \leq x \leq {}^il_1) \quad (3.56)$$

Written in matrix form for equation (3.56):

$$\delta \chi_{11} = \begin{bmatrix} \frac{4}{{}^il_1} - 6\frac{x}{({}^il_1)^2} & \frac{2}{{}^il_1} - 6\frac{x}{({}^il_1)^2} \end{bmatrix} \begin{bmatrix} \delta \theta_1 \\ \delta \theta_2 \end{bmatrix} = \begin{bmatrix} \frac{4}{{}^il_1} - 6\frac{x}{({}^il_1)^2} & \frac{2}{{}^il_1} - 6\frac{x}{({}^il_1)^2} \end{bmatrix} \mathbf{T} \delta \mathbf{u}^n = {}^i\mathbf{B}^{Bend} \delta \mathbf{u}^n \quad (3.57)$$

Where  ${}^i\mathbf{B}^{Bend}$  is the Strain-displacement matrix for bending at time  ${}^it$ :

The elementary bending nodal loads at time  ${}^it$  are given as:

$${}^i\mathbf{F}_{Bend-int}^e = \sum_{p=1}^n \int_{({}^iL)^p} ({}^i\mathbf{B}^{Bend})^p T ({}^iM^{11})^p dL \quad (3.58)$$

### 3.3.10 Fiber segment bending moment update

The fiber segment bending moment  $({}^{i+1}M^{11})^p$  at time  ${}^{i+1}t$  can be updated using the following equations:

$$({}^{i+1}M^{11})^p = \Gamma \left( ({}^{i+1}\chi_{11})^p \right) \quad (3.59)$$

Where  $\Gamma$  is constitutive function that relates fiber's bending moment and curvature. Curvature  ${}^{i+1}\chi_{11}$  can be updated as following:

$$({}^{i+1}\chi_{11})^p = ({}^i\chi_{11})^p + ({}^i\mathbf{B}^{Bend} \Delta \mathbf{u}^n)^p \quad (3.60)$$

### 3.3.11 Imposition of the boundary conditions

In the above derivation process of the incremental rotation angles  $\Delta\theta_1$  and  $\Delta\theta_2$ , it's implicitly assumed fiber segment  $f1 - f2$  has two neighbor fiber segments. The boundary conditions at node 1 when node 4 is missing are needed to consider (this equals fiber endpoints  $f1, f2$  and  $f3$  exist,  $f4$  is missing), since it would affect the calculation of incremental rotation angles. The boundary condition at node 2 when node 3 is missing can be handled in the same way (this equals fiber endpoints  $f1, f2$  and  $f4$  exist,  $f3$  is missing). The method to impose the boundary conditions is very similar as that in reference [BAT 08, SAB 06]. Two cases concerning the boundary condition at node 1 when node 4 is missing are considered for the calculation of incremental rotation angles of fiber endpoints:

- Clamp or symmetry condition, which equally means the displacements of fiber endpoint  $f1$  are null and fiber endpoint  $f4$  is missing. The equation (3.37) is not valid anymore to calculate the incremental rotation angle and should be modified as following:

$$\begin{bmatrix} \Delta\theta_1 \\ \Delta\theta_2 \end{bmatrix} = \begin{bmatrix} -1 & 0 \\ {}^iA_3 & {}^iA_4 \end{bmatrix} \begin{bmatrix} \beta \\ \Delta\phi_2 \end{bmatrix} \quad (3.61)$$

Where  $\beta = \frac{\Delta\bar{\mathbf{u}}_2^f \cdot {}^i\bar{\mathbf{n}}_1 - \Delta\bar{\mathbf{u}}_1^f \cdot {}^i\bar{\mathbf{n}}_1}{i l_1}$  is the incremental rigid rotation angle of geometry straight segment  $f1 - f2$ ,  $\Delta\phi_2$  is the same as in equation (3.30), the coefficients  ${}^iA_3$  and  ${}^iA_4$  are as follows:

$${}^iA_3 = \frac{1}{3} \frac{i l_2}{i l_1 + i l_2}, \quad {}^iA_4 = \frac{2}{3} \frac{i l_2}{i l_1 + i l_2} + \frac{1}{3} \frac{i l_1^2}{(i l_1 + i l_2)^2} \quad (3.62)$$

- Free edge condition, which equally means the curvature at fiber endpoint  $f1$  is zero:

$$\begin{bmatrix} \Delta\theta_1 \\ \Delta\theta_2 \end{bmatrix} = \begin{bmatrix} -\frac{1}{2} {}^iA_4 & 0 \\ 0 & {}^iA_4 \end{bmatrix} \begin{bmatrix} \Delta\phi_2 \\ \Delta\phi_2 \end{bmatrix} \quad (3.63)$$

Where  $\Delta\phi_2$  is the same as in equation (3.30), the coefficient  ${}^iA_4$  is:

$${}^iA_4 = \frac{2}{3} \frac{i l_1}{i l_1 + i l_2} + \frac{1}{3} \frac{2 i l_1^2}{(2 i l_1^2 + 3 i l_1 i l_2 + i l_2^2)} \quad (3.64)$$

## 3.4 Numerical simulation and experimental comparisons

The proposed specific plane shell element is composed of fiber segments, in the actual implementation, it's not necessary to make a summation over the real number of fiber segments in the element, a set of equivalent number of fiber segments can be assumed to be uniformly distributed through the thickness direction of element and their summation of tensile and bending stiffnesses equal sample's realistic mechanical properties.

### 3.4.1 Simulations of book bending tests

To verify whether this specific plane shell element has the capability to simulate the bending deformation of thick fibrous materials, book is no doubt one of the best candidates. In the bending, each page paper can be modeled as 'fiber', it's close to be inextensible and there exists relative sliding between pages. These features are very similar to the bending kinematics of thick fibrous materials made of parallel fibers. A book made of 130 sheets of A4 size blank papers (297 x 210 mm) is used for the following bending tests (total thickness of the book is about 13 mm).

#### 3.4.1.1 The influence of friction between pages on the bending stiffness of book

Cantilever bending has been conducted for the book and its single page paper respectively (Figure 3.8). The main purpose is to investigate the influence of friction on the bending stiffness. Figure 3.8c shows the comparison of the midline for the the bending of a book and for the bending of single page paper in the cantilever bending (same bending length in the two cases). They are almost coincident. This indicates the friction force between pages is very small, in some extent it can be neglected. Consequently, book's bending stiffness mainly depends on the bending stiffness of individual page paper and equals their summation. The bending stiffness of single page paper can be obtained by processing its image of bending deflection shape that shown in Figure 3.8b with the bending test method mentioned in chapter 2. The result is shown in Figure 3.9 (moment refers to bending moment per unit width,  $\text{N} \cdot \text{mm}/\text{mm} = \text{N}$ ). The unit of bending stiffness is  $\text{N} \cdot \text{mm}$  (bending stiffness per unit width). In the bending deformation, each page paper is close to be inextensible, which requires the use of a relative high tensile stiffness in the simulation. It works as penalty factor. The real tensile stiffness of paper can be used, but using a higher value would not noticeably affect the simulation result. The detailed information about the mechanical properties of single page paper used in the following simulations is shown in Table 3.1.

**Table 3.1** – Mechanical properties of single page paper

Tensile stiffness $C$ (per unit width)	230 N/mm
Bending stiffness $B$ (per unit width)	0.4 N · mm

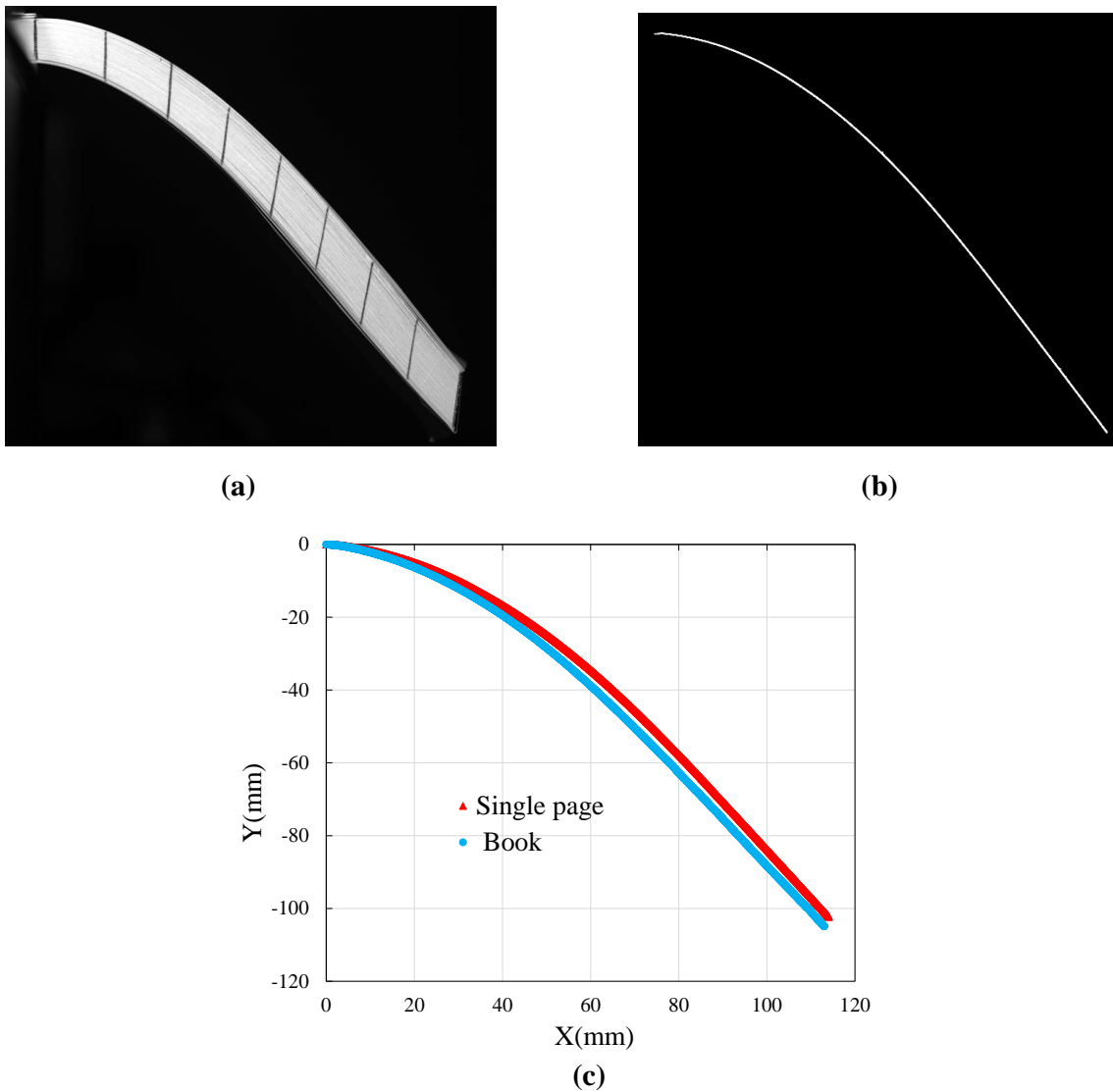


**Figure 3.8** – Cantilever bending: (a) Book. (b) Single page paper. (c) Comparison of their midlines.

### 3. Specific plane shell element for simulating the bending deformation of thick fibrous materials

---

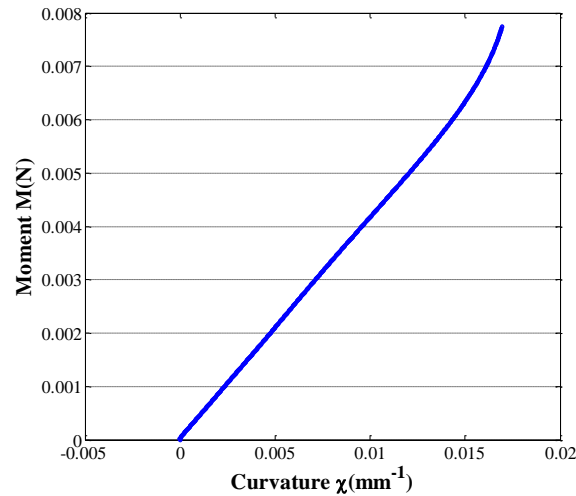


Figure 3.9 – Moment-curvature curve of single page paper.

#### 3.4.1.2 Bending test 1

The cantilever bending of book under gravity has been simulated (Figure 3.10). Figure 3.11 shows the deformation shapes from experiment and simulation. Their midlines are almost coincident (Figure 3.12). Another two important aspects that we concern are the angle between the material director and the horizontal direction and the thickness along the direction of material director after deformation. In this thesis, unless specifically mentioned, the horizontal direction refers to  $\mathbf{e}_1$  (Figure 3.3). The angles between the material directors that are numbered in Figure 3.11 a and the horizontal direction have been compared with the simulation results. As shown from Figure 3.13, they are very close to each other. Figure 3.14 presents the comparison between experiment and simulation for the thickness along the material director direction after deformation. They are in good agreement and it's shown that there exists thickness stretching in the material director direction.

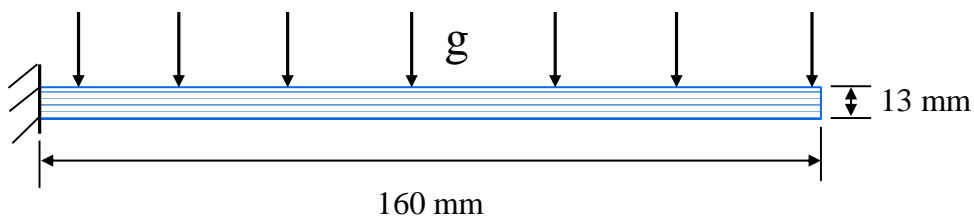
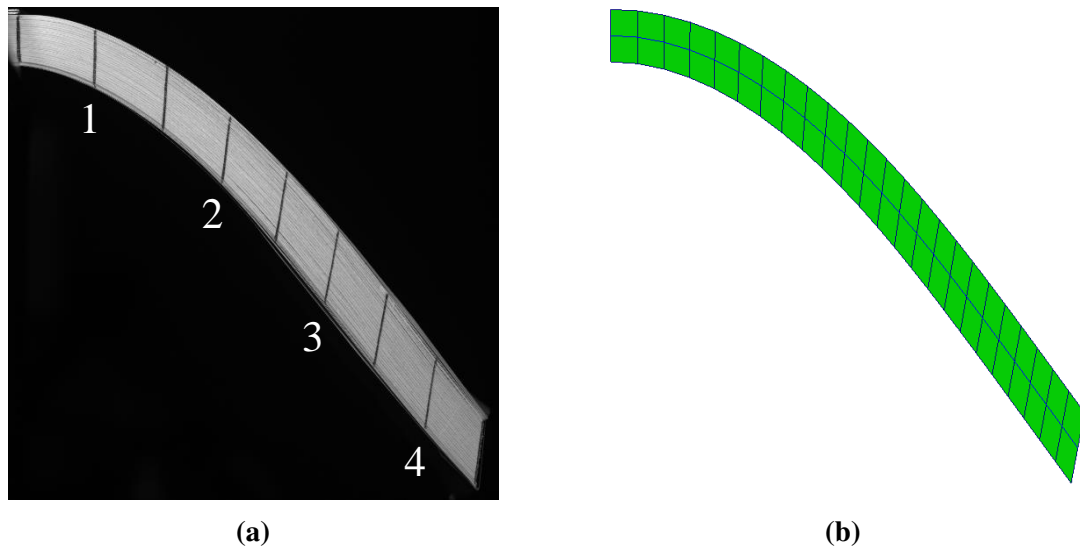


Figure 3.10 – Geometry parameters of book cantilever bending.

#### 3.4.1.3 Bending test 2

One end of the book is clamped, and the other end is imposed a 46 mm horizontal displacement (Figure 3.15). Figure 3.16 presents the deformation shapes from experiment



**Figure 3.11** – Book cantilever bending deformation: (a) Experiment. (b) Simulation (with midline plotting).

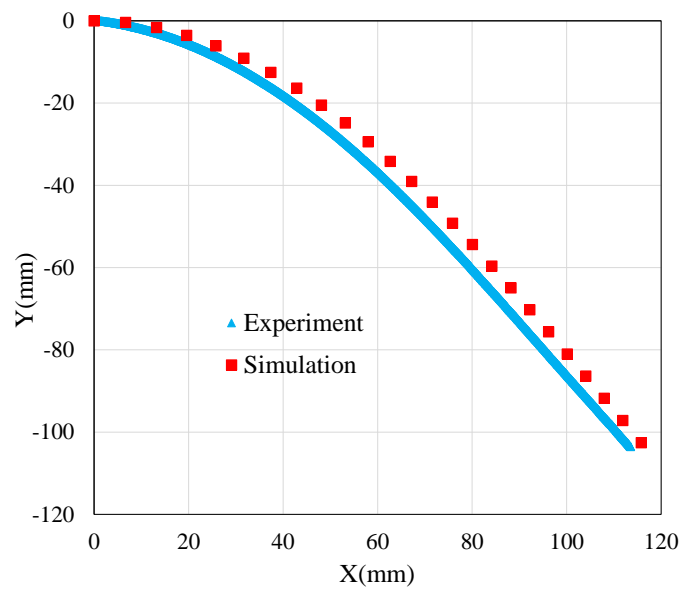


**Figure 3.12** – Comparison of the midline between experiment and simulation for book cantilever bending

### 3. Specific plane shell element for simulating the bending deformation of thick fibrous materials

---

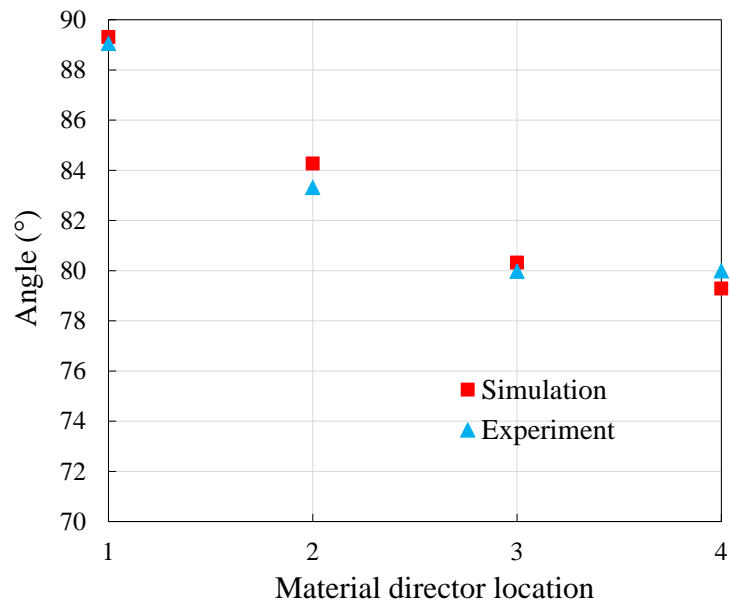


**Figure 3.13** – Comparison of experiment and simulation for book cantilever bending: the angle between the material director and the horizontal direction

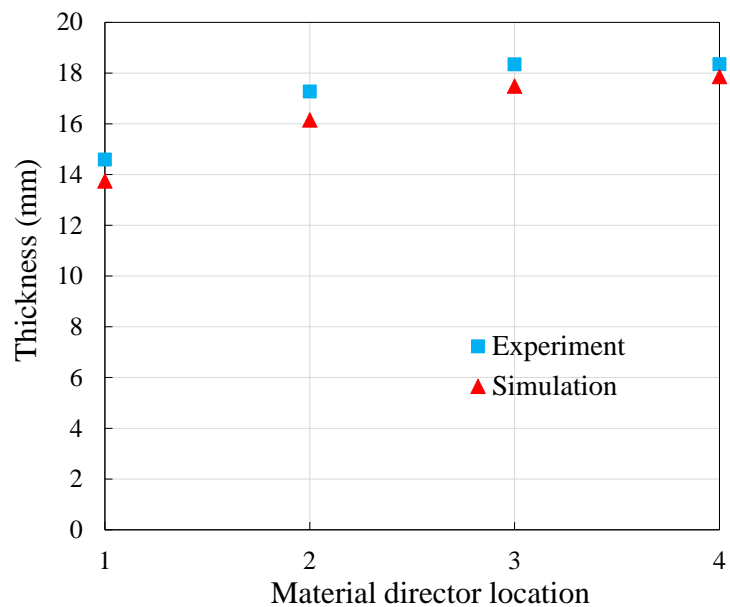


**Figure 3.14** – Comparison of the thickness in the material director direction between experiment and simulation for book cantilever bending

and simulation. Their midline shapes comparison is shown in Figure 3.17. They are almost the same. Comparison for the angles between the material directors numbered in Figure 3.16a and the horizontal direction have been performed between experiment and simulation. As indicated from Figure 3.18, they are in good agreement. The thickness in the material director direction has been verified with the experiment. Their comparison is shown in Figure 3.19, they are very close to each other.

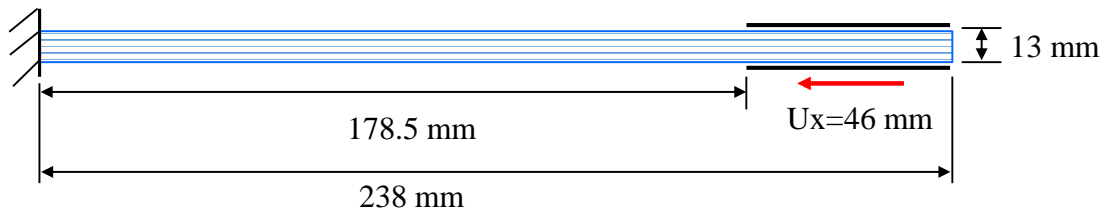
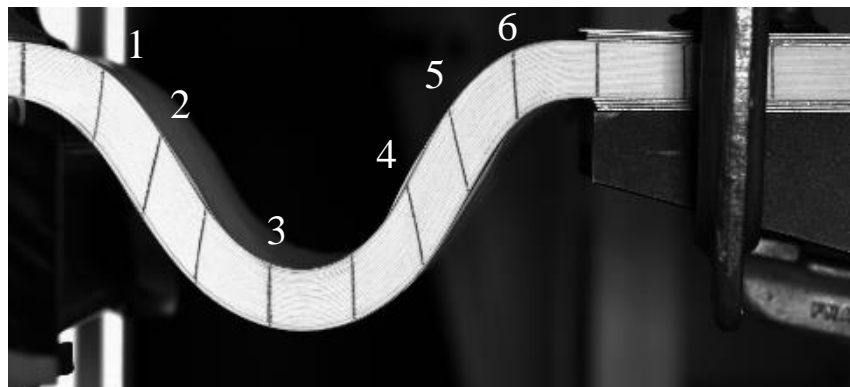
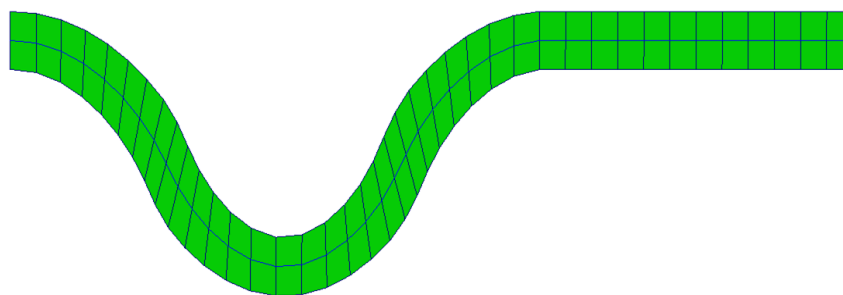


**Figure 3.15** – Boundary conditions of book bending test 2.



(a)



(b)

**Figure 3.16** – Deformation shape of book bending test 2: (a) Experiment. (b) Simulation (with midline plotting).

3. Specific plane shell element for simulating the bending deformation of thick fibrous materials

---

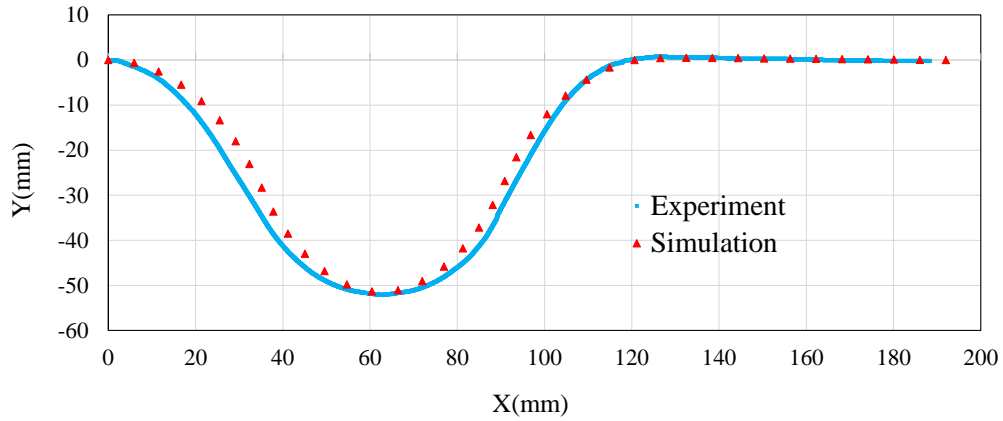


**Figure 3.17** – Comparison of the midline between experiment and simulation for book bending test 2.

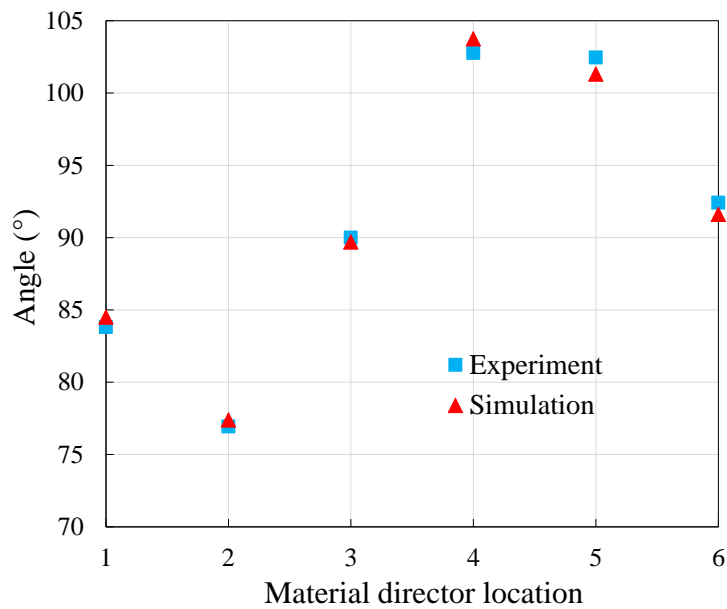


**Figure 3.18** – Comparison of experiment and simulation for book bending test 2: the angle between the material director and the horizontal direction

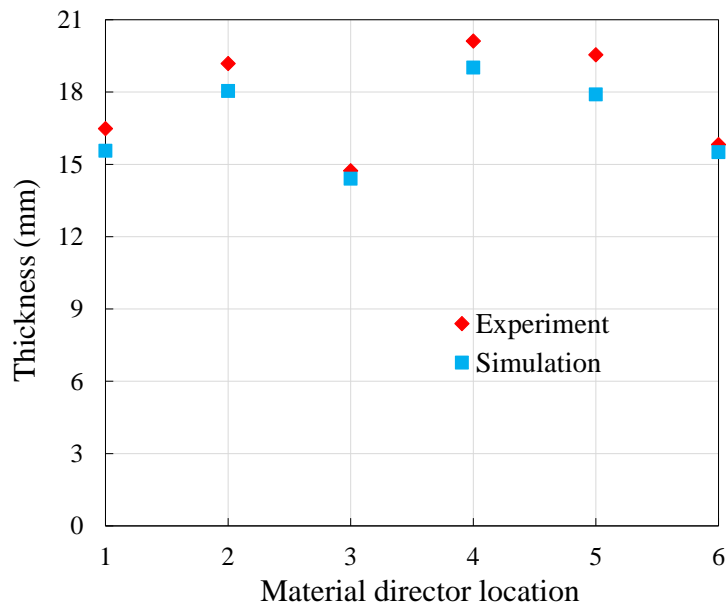


**Figure 3.19** – Comparison of the thickness in the material director direction between experiment and simulation for book bending test 2.

#### 3.4.1.4 Bending test 3

A more complex bending deformation test on the book has been conducted. One end of the book is clamped, and another end is imposed both horizontal and vertical displacements (Figure 3.20). The deformation shapes from experiment and simulation are shown in Figure (Figure 3.21). Midline shapes comparison is made in Figure 3.22. They are almost coincident. Figure 3.23 presents the comparison of experiment and simulation for the angles between the material directors numbered in Figure 3.21a and the horizontal direction. It's evident that they are very close to each other. The thickness in the material director direction has also been checked. Figure 3.24 shows the comparison results. They are in good agreement.

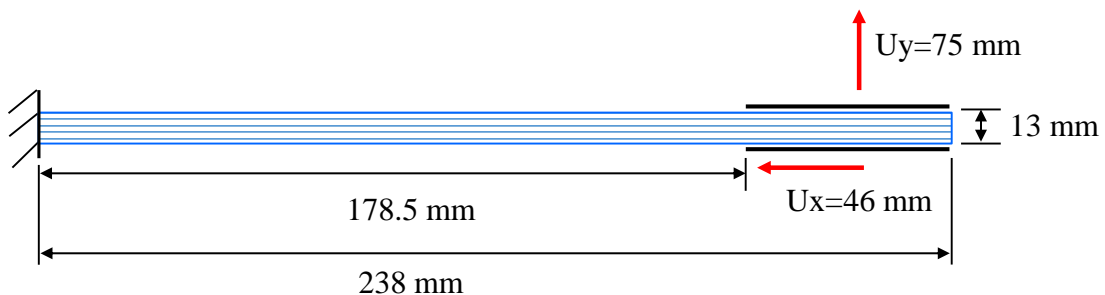


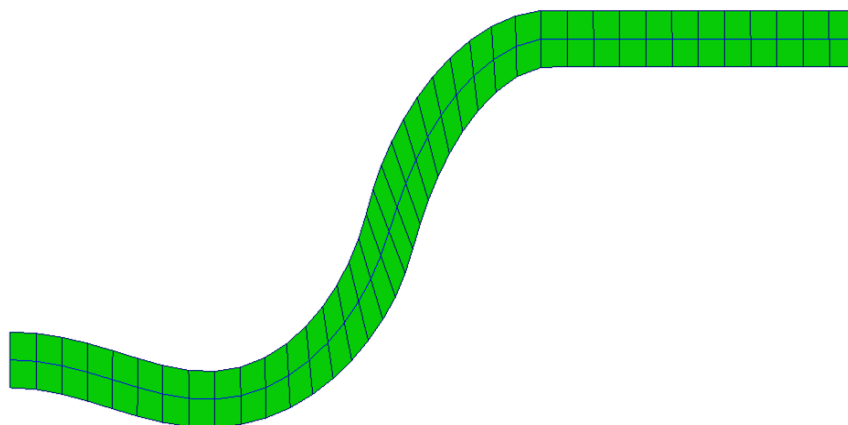
**Figure 3.20** – Boundary conditions of book bending test 3.

### 3. Specific plane shell element for simulating the bending deformation of thick fibrous materials

---



(a)



(b)

**Figure 3.21** – Deformation shape of book bending test 3: (a) Experiment. (b) Simulation (with midline plotting).

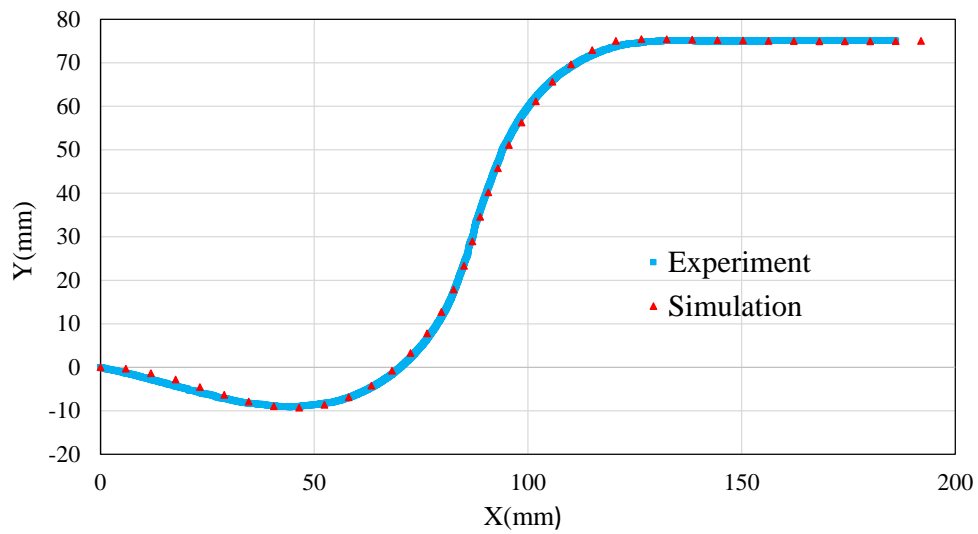


**Figure 3.22** – Comparison of the midline between experiment and simulation for book bending test 3.

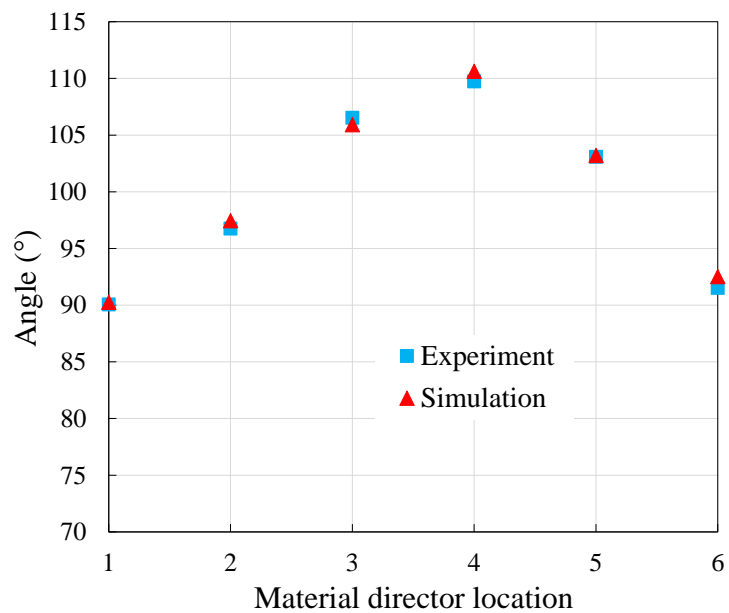


**Figure 3.23** – Comparison of experiment and simulation for book bending test 3: the angle between the material director and the horizontal direction.

### 3. Specific plane shell element for simulating the bending deformation of thick fibrous materials

---

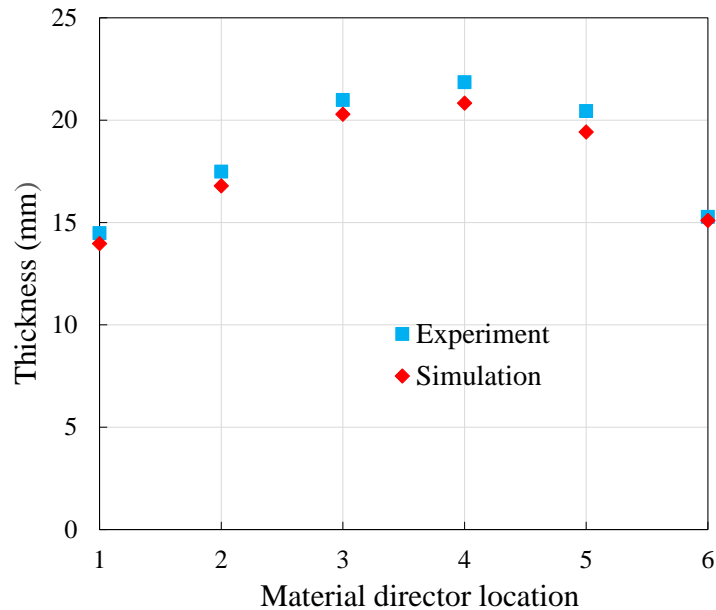


**Figure 3.24** – Comparison of the thickness in the material director vector direction between experiment and simulation for book bending test 3.

#### 3.4.2 Simulations of laminated reinforcement bending tests

The laminated reinforcement in the present work is an assembly of 20 plies of dry fabrics G0986 (total thickness is about 10 mm), which are stacked in the same orientation. Some soft threads are placed by manual in the thickness direction to hold all the plies together but allowing the relative sliding between the plies in the deformation.

##### 3.4.2.1 The influence of friction between plies on the bending stiffness of laminated reinforcement

The bending stiffness of laminated reinforcement not only depends on the bending stiffness of its single ply but also the friction force between them. It's very necessary to have a knowledge about the portion of bending stiffness contributed by the friction force. Figure 3.25a and b present respectively the bending deformation shapes of laminated reinforcement and its single ply under gravity. Bending length is the same in the two cases (118 mm). Image processing on single ply's bending deflection shape shown in Figure 3.25b has been performed. Its corresponding moment-curvature curve is shown Figure 3.26. It's almost linear and the bending stiffness of single ply can be seen as a constant value. The bending behaviour of laminated reinforcement is also characterized by the moment-curvature curve on its midline. Figure 3.27 shows the corresponding result that comes from the image processing of the bending deflection shape in Figure 3.25a. For laminated reinforcement, if there is no friction between plies, its bending stiffness should be the summation of individual ply and this value is shown in Figure 3.27. A comparison has been made for the two moment-curvature curves (Figure 3.27). We call the moment-

curvature curve which comes from the bending test of laminated reinforcement is curve 1 and that comes from the summation of individual ply is curve 2. When given a certain curvature, the corresponding moment required for the curve 1 is larger than curve 2, their difference is called the friction moment, which is induced by the friction force. The friction moment seems almost constant throughout all curvatures, and takes a large part of the total moment that required for the bending of laminated reinforcement, up to about 50% (Figure 3.27). Consequently, taking into account the friction contribution on the bending stiffness of laminated reinforcement is very necessary and indispensable. In the following simulations, each ply can be modeled as a ‘fiber’, the bending stiffness of each ply comes from the moment-curvature curve of laminated reinforcement that is shown in Figure 3.27, which can be approximated by a piecewise linear curve. For tensile deformation, a relative high tensile stiffness would be used to work as penalty factor to meet the in-extensibility requirement for fiber in the bending deformation. The real tensile stiffness of single ply can be used, but using a higher value would not significantly change the simulation result. The detailed information about the mechanical properties of laminated reinforcement single ply used in the following simulation tests is given in Table 3.2.

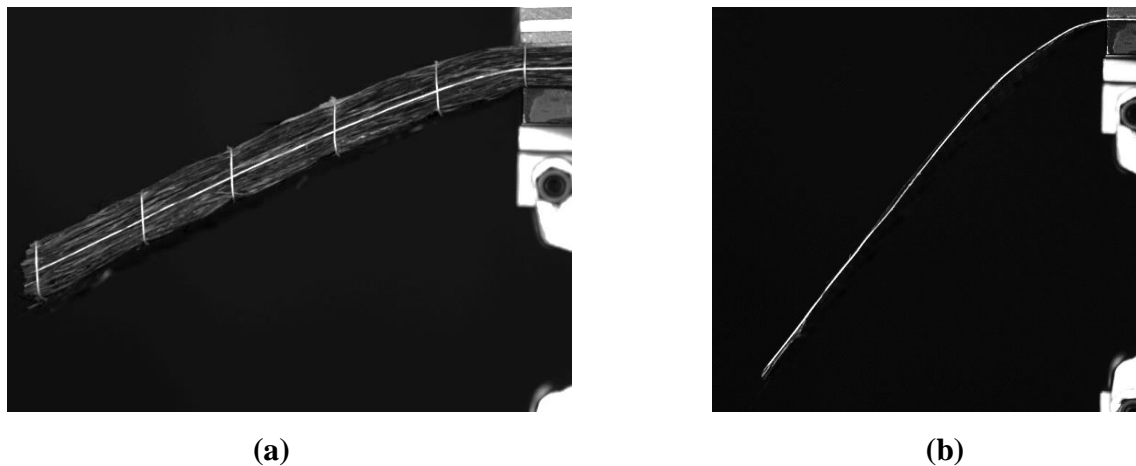


**Figure 3.25** – Cantilever bending test: (a) Laminated reinforcement. (b) Single ply.

### 3.4.2.2 Cantilever bending test

Cantilever bendings have been conducted for laminated reinforcement. The bending length in test A is 118 mm and in test B is 132 mm. The only difference for the samples used in test A and test B is their length, others are identical. Figure 3.28 shows the experiment and simulation results. They are almost the same. An interested thing can be noted from Figure 3.28: there is almost no rotation for the material directors and they are parallel to each other in the bending. For the part close to clamp end, even there is no rotation for the material directors, the corresponding curvature of midline is not zero. This phenomenon further proves our deduction previously that curvature calculation used in

3. Specific plane shell element for simulating the bending deformation of thick fibrous materials

---

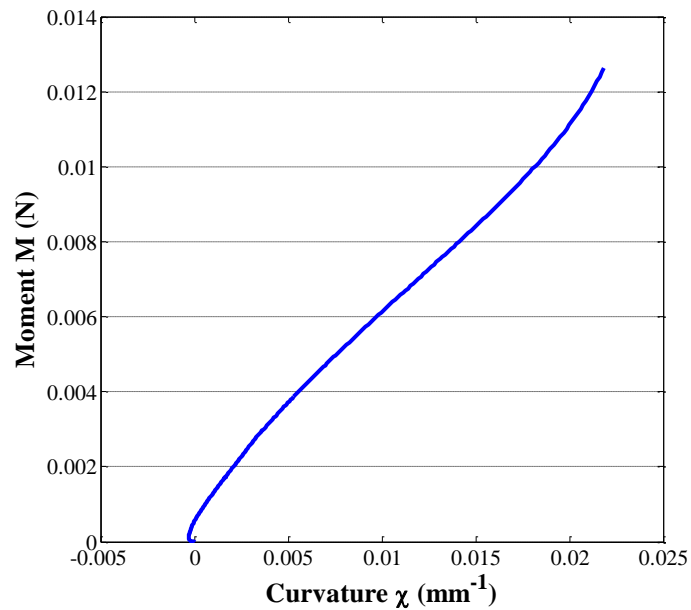


**Figure 3.26** – Moment-curvature curve of laminated reinforcement's single ply

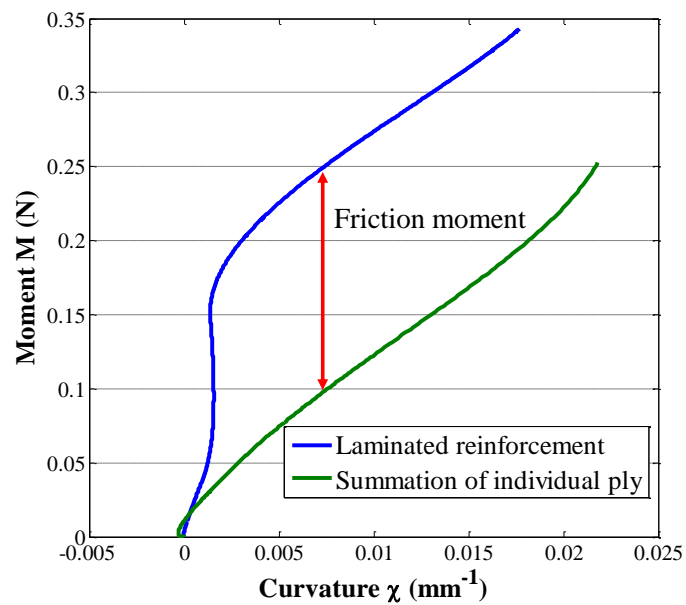


**Figure 3.27** – Moment-curvature curve from bending test of laminated reinforcement and from summation of individual ply.

**Table 3.2** – Mechanical properties of laminated reinforcement’s single ply with taking into account the influence of friction on the bending stiffness

Number of plies	20
Tensile stiffness $C$ (per unit width)	1200 N/mm
	$B=7.5 \text{ N} \cdot \text{mm}$ , when $-0.001 \leq \chi_{11} \leq 0.001$ bending moment $M^{11} = B\chi_{11}$
	$B=0.5 \text{ N} \cdot \text{mm}$ , when $\chi_{11} \geq 0.001$
Bending stiffness $B$ (per unit width)	bending moment $M^{11} = B\chi_{11} + 0.075$ $B=0.5 \text{ N} \cdot \text{mm}$ , when $\chi_{11} \leq -0.001$ bending moment $M^{11} = B\chi_{11} - 0.075$

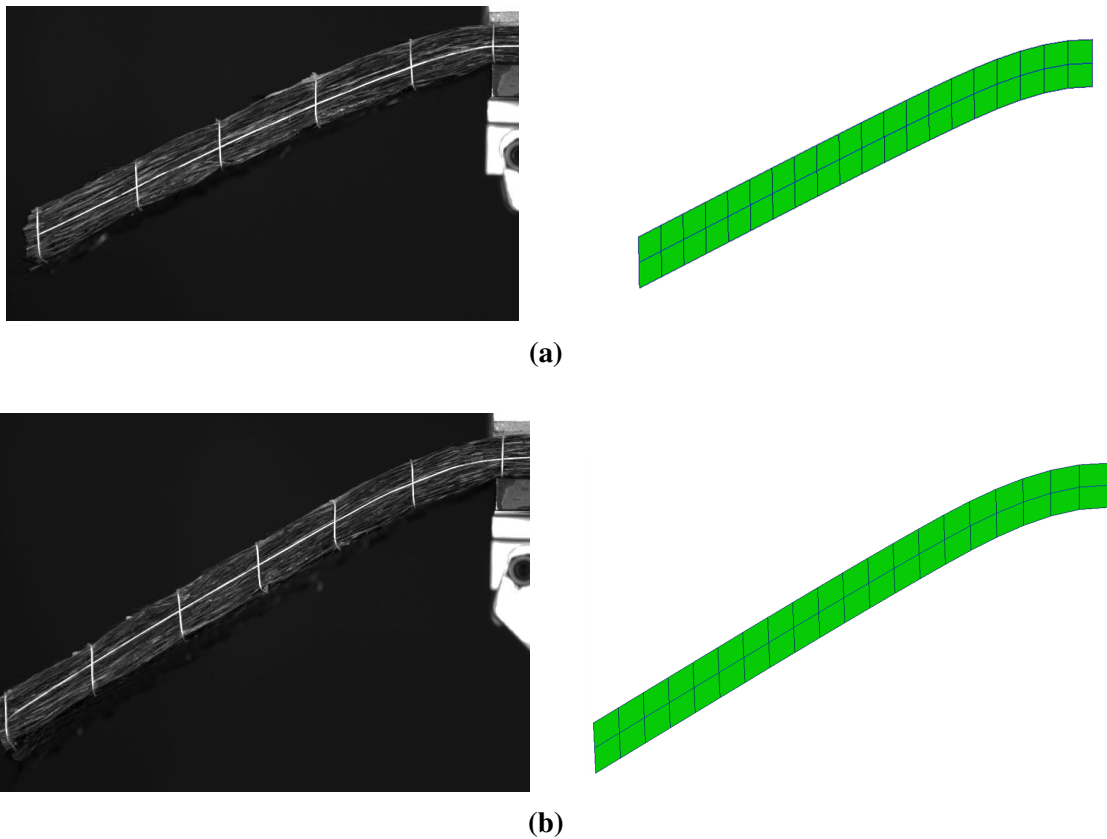


**Figure 3.28** – Deformation shape of laminated reinforcement in the cantilever bendings: (a) Test A: bending length 118 mm. Left: experiment, Right: simulation. (b) Test B: bending length 132 mm. Left: experiment, Right: simulation.

### 3. Specific plane shell element for simulating the bending deformation of thick fibrous materials

---

the Mindlin shell theory can't be applied to the shell structure of fibrous materials. Simulations with the specific plane shell element correctly captures the phenomenon observed in the experiments (Figure 3.28). Figure 3.29 presents the comparison of midline between experiment and simulation. They are almost coincident.

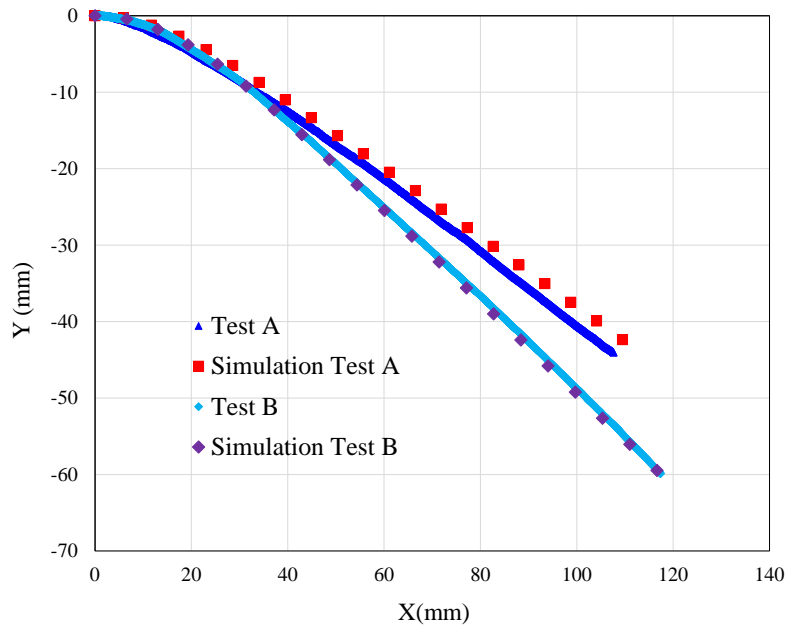


**Figure 3.29** – Comparison of the midline between experiment and simulation for laminated reinforcement in the cantilever bending.

#### 3.4.2.3 Complex bending test 1

One end of the laminated reinforcement is clamped, and another end is imposed both horizontal and vertical displacements (Figure 3.30). The deformation shapes from the experiment and simulation are shown in Figure 3.31. Figure 3.32 presents the comparison of their midlines. They are almost the same. The angles between the material directors that are numbered in Figure 3.31a and the horizontal direction have been compared with the simulation results. As shown from Figure 3.33, they are very close. The thickness in the material director direction also has been checked. Figure 3.34 shows the comparison. An extension of thickness in the material director direction can be observed and they are in good agreement with experiment results.

#### 3.4.2.4 Complex bending test 2

A larger horizontal displacement is imposed on the laminated reinforcement compared with complex bending test 1 ( $U_x = 19$  mm), while the vertical displacement keeps the same. The deformation shapes from experiment and simulation are shown in Figure 3.35. Figure 3.36 shows their midline shapes comparison. They are very close to each other.

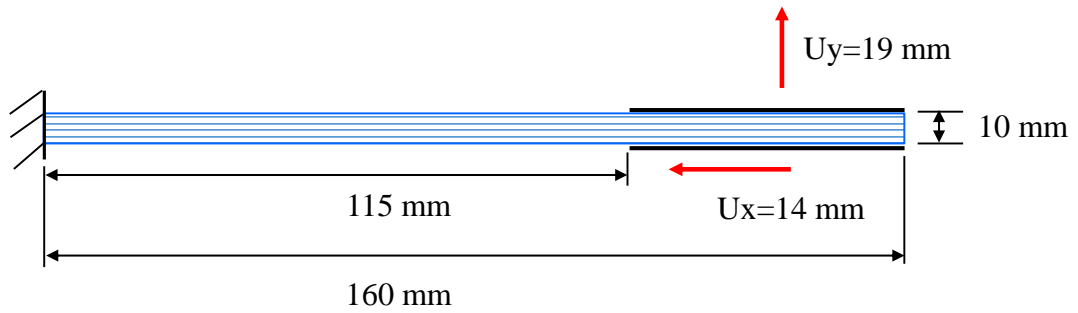
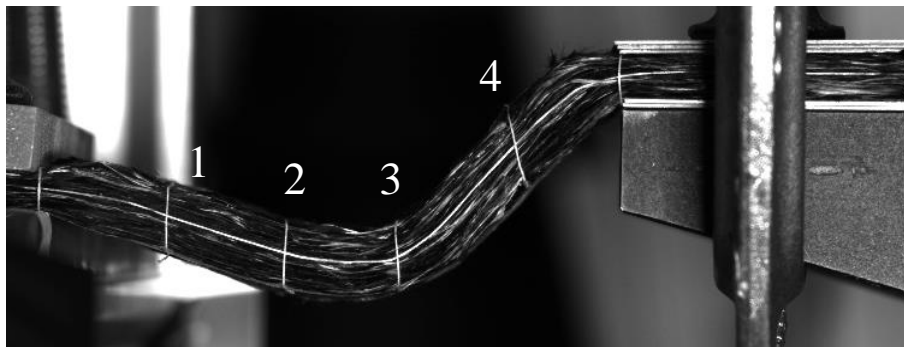
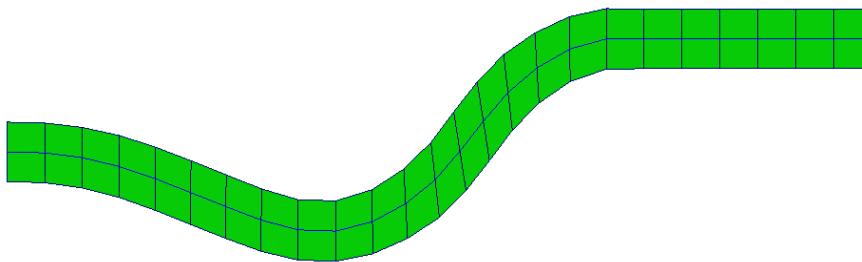


**Figure 3.30** – Boundary conditions of complex bending test 1 for laminated reinforcement.



(a)



(b)

**Figure 3.31** – Deformation shape of laminated reinforcement in complex bending test 1: (a) Experiment. (b) Simulation (with midline plotting).

3. Specific plane shell element for simulating the bending deformation of thick fibrous materials

---

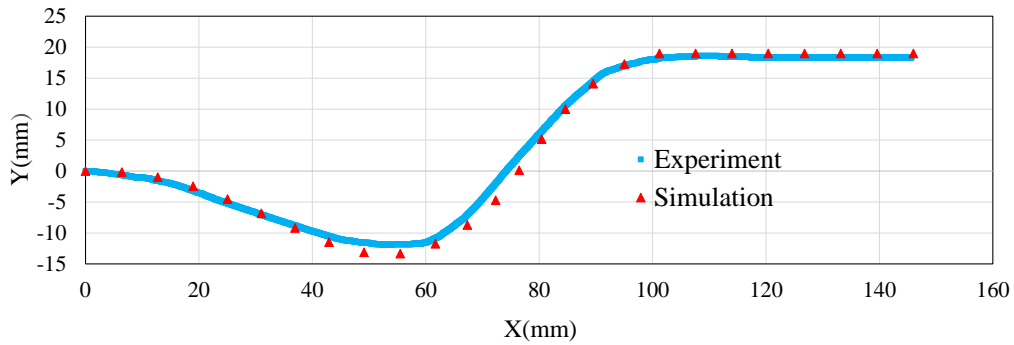


**Figure 3.32** – Comparison of the midline between experiment and simulation for laminated reinforcement in complex bending test 1.

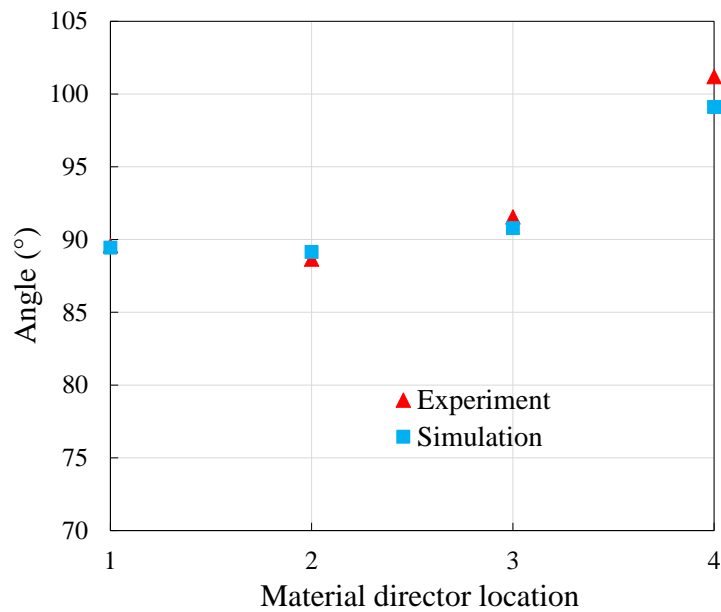


**Figure 3.33** – Comparison of experiment and simulation for laminated reinforcement in complex bending test 1: the angle between the material director and the horizontal direction.

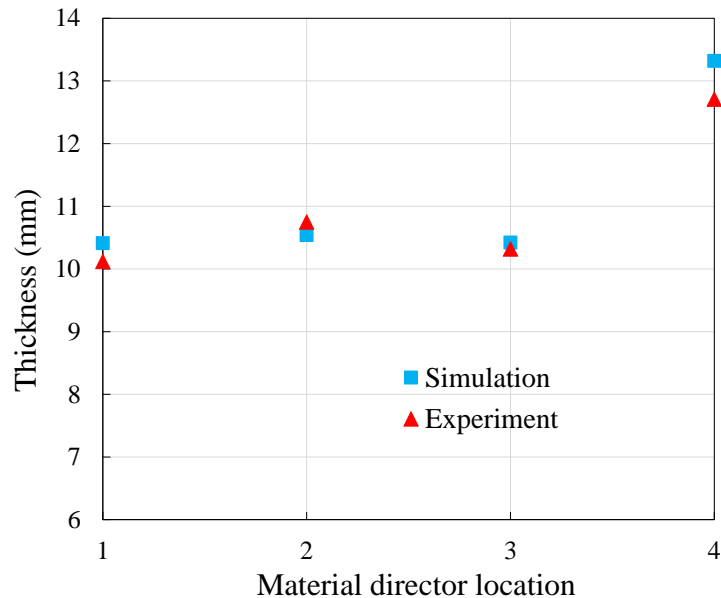


**Figure 3.34** – Comparison of the thickness in the material director direction between experiment and simulation for laminated reinforcement in complex bending test 1.

Figure 3.37 presents the comparison of experiment and simulation for the angles between the material directors numbered in Figure 3.35 and the horizontal direction. A good coincidence is demonstrated. The thickness in the material director direction has also been checked. Figure 3.38 shows the comparison results. They are in good agreement.

### 3.4.3 Three points bending tests for layer to layer angle interlock

Three points bending simulations have been conducted to show this specific plane shell element has the capability to simulate bending deformation for thick interlock. The interested interlock is the same type as that in reference [MAT 14], which is layer to layer angle interlock. In all the following simulations we consider the sample with the dimension of 200 mm x 30 mm x 15 mm, and a displacement is directly imposed in the middle of the specimen. The bending stiffness of fiber comes from the literature [MAT 14], in which the bending stiffness of interlock is about 80 N.mm (bending stiffness per unit width). The tensile stiffness of interlock is chosen as 11500 N/mm (tensile stiffness per unit width). Figure 3.39 shows the simulation results with different displacements. They are globally consistent with experiments, especially correctly captures the shape of the external ends of sample after deformation. The comparison of midline between experiment and simulation is shown in Figure 3.40. They are in a good agreement. These results are as good as those obtained by S.Mathieu using 3D solid elements with taking into account fiber's bending [MAT 15] and those obtained by A.madeo using the second gradient theory [MAD 15], but here we use fewer elements compared with them. The angles between the material directors numbered in Figure 3.39 and the horizontal direc-

### 3. Specific plane shell element for simulating the bending deformation of thick fibrous materials

---

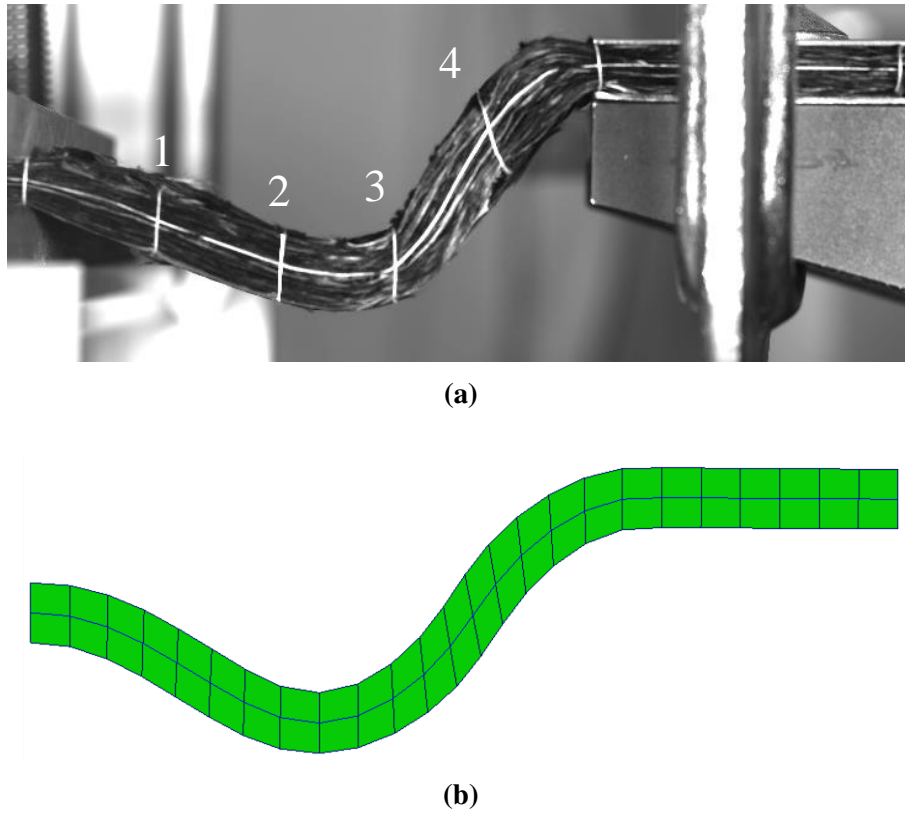


**Figure 3.35** – Deformation shape of laminated reinforcement in complex bending test 2: (a) Experiment. (b) Simulation (with midline plotting).

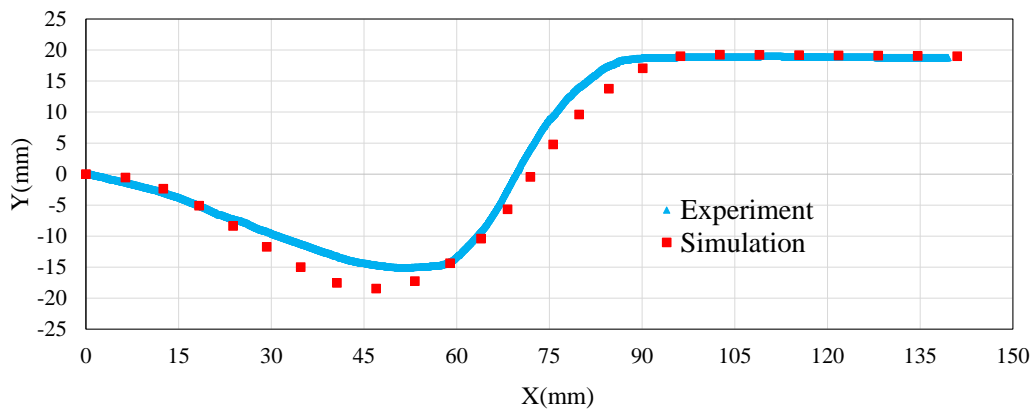


**Figure 3.36** – Comparison of the midline between experiment and simulation for laminated reinforcement in complex bending test 2.

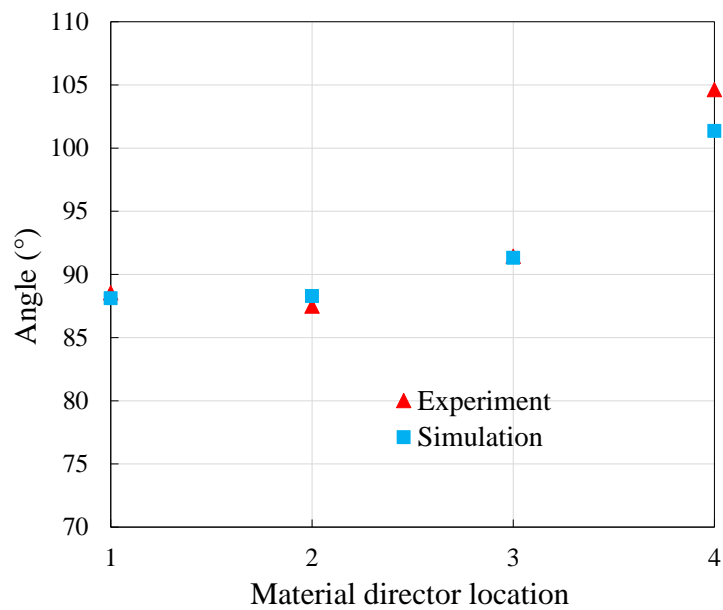


**Figure 3.37** – Comparison of experiment and simulation for laminated reinforcement in complex bending test 2: the angle between the material director and the horizontal direction.

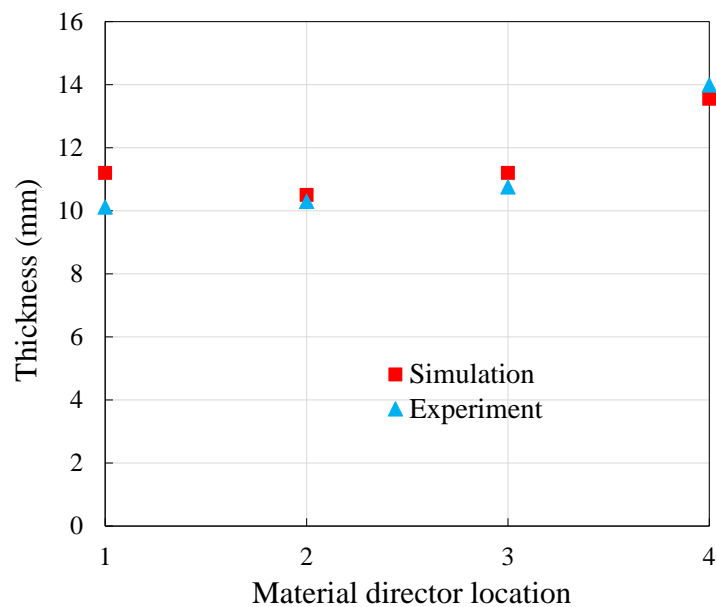


**Figure 3.38** – Comparison of the thickness in the material director direction between experiment and simulation for laminated reinforcement in complex bending test 2.

### 3. Specific plane shell element for simulating the bending deformation of thick fibrous materials

---

tion have been compared with simulations. Figure 3.41 and 3.42 show the corresponding comparison between experiment and simulation for 40 mm and 60 mm displacement test respectively. There exists some discrepancies between experiment and simulation, but globally they are in good coincidence. These discrepancies can be attributed to the local contact between the rigid steel hemisphere and sample in the experimental testing where deformation is driven by the interaction between the rigid steel hemisphere and sample, but in the simulation, the displacement is directly imposed on the sample and there is no such local contact. The local contact makes the fibers contacting with rigid steel hemi-

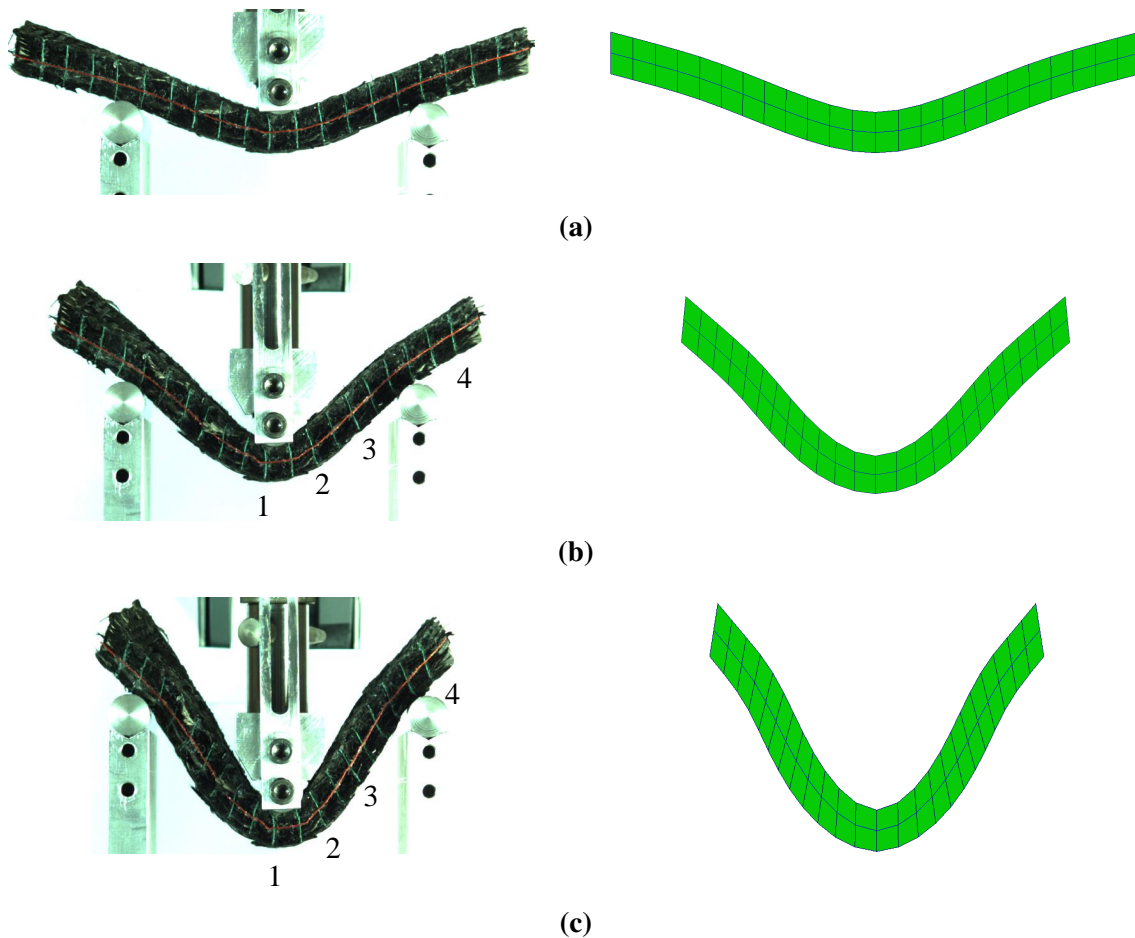


**Figure 3.39** – Three points bending test of interlock: (a) 20 mm displacement, left: experiment, right: simulation. (b) 40 mm displacement, left: experiment, right: simulation. (c) 60 mm displacement, left: experiment, right: simulation.

sphere have much larger curvature than the fibers which are not. Since fiber is subjected to the quasi-inextensibility constraint, which imposes a relative sliding for these fibers, as a result, an additional rotation of the material director occurs due to the local contact. This results in the discrepancy that we have observed between the experiment and simulation. In the experimental test, if we use a smaller radius rigid steel hemisphere to impose the

deformation, the influence of local contact would decrease and there would have a better agreement between experiment and simulation.

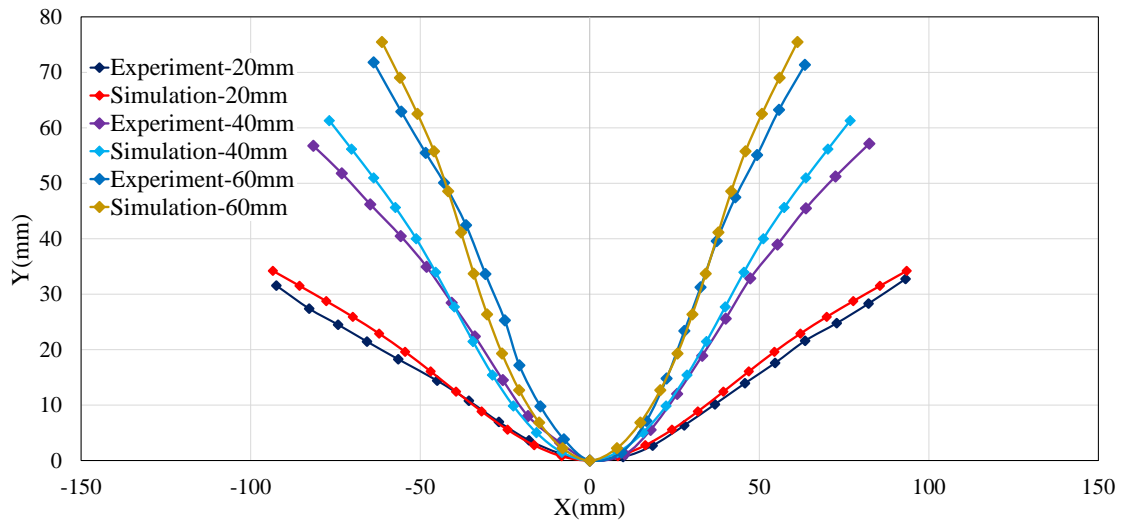


**Figure 3.40** – Comparison of the midline between experiment and simulation for interlock three points bending test.

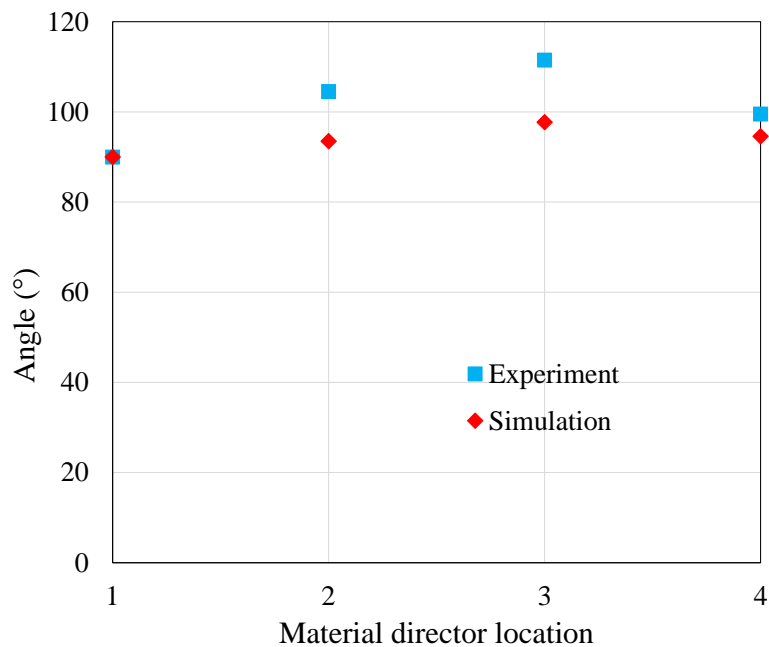


**Figure 3.41** – Comparison of experiment and simulation for interlock three points bending with 40 mm displacement: the angle between the material director and the horizontal direction.

### 3. Specific plane shell element for simulating the bending deformation of thick fibrous materials

---

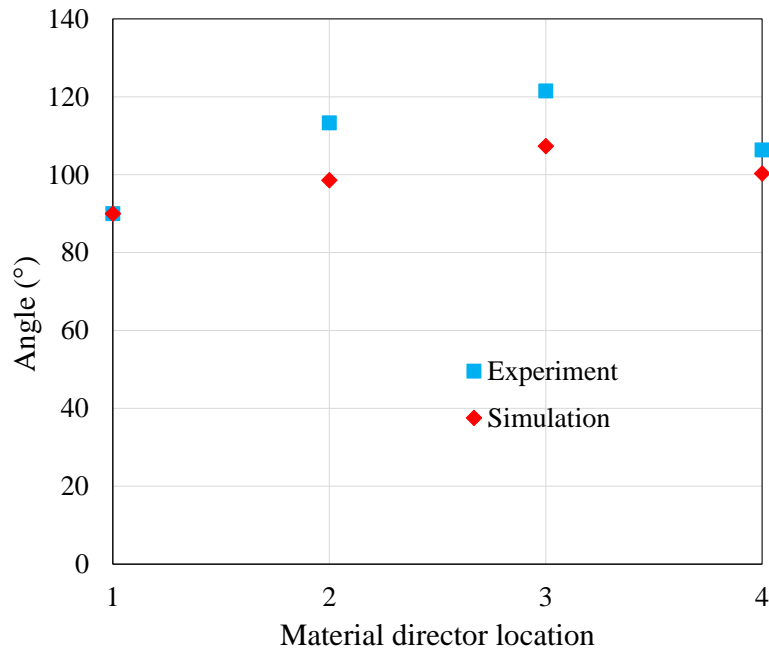


**Figure 3.42** – Comparison of experiment and simulation for interlock three points bending with 60 mm displacement: the angle between the material director and the horizontal direction.

#### 3.4.4 Simulation of L-flange bending deformation

Daniel Leutz et al [LEU 16] recently have conducted L-flange bending deformation experiments for a thick laminate with 36 plies. We would try to use our specific plane shell element to reproduce this bending deformation. Our main purpose is to see whether the specific plane shell element can correctly predict the bending deformation shape of fibrous materials with very high ratio of thickness to length. The dimension of sample in the simulation is the same as that used in the article [LEU 16], which is 33.8 mm (Length) x 76.2 mm (Width) x 6.4 mm (Thickness). In the reference [LEU 16], it didn't give a detailed information about the bending stiffness of laminate or its single ply. Consequently, in our simulation, we would give it an estimated value (with inverse method). The bending stiffness of single ply at the forming temperature is given as 0.4 N.mm (bending stiffness per unit width). In the experiment, it's the pressure force to make the sample deform, in our simulation we impose an equivalent displacement, there is no doubt this element would also work when imposed a pressure force. The equivalent displacement comes from the measurement of final experimental configuration in Figure 3.43a. Figure 3.43b presents the simulation result with the specific plane shell element. It's very close to the experimental shape, particularly for the shape at the free end. The angle between the material director located at the free end and the horizontal direction (Figure 3.43a) has been compared with the simulation, in which the value measured from the experiment is  $77.38^\circ$  and the value from the simulation is  $76.51^\circ$ . They are very close. The thickness in

the direction of this material director is also compared with simulation. The value from the experiment and simulation is 8.25 mm and 9.15 mm respectively. Compared with the simulation result in Figure 3.43c, where each ply is discretized by the classical shell element, the specific plane shell element allows to use fewer elements but meantime it still has a good predication ability. This example further demonstrates the new specific shell element can accurately simulate the bending deformation for thick fibrous materials.

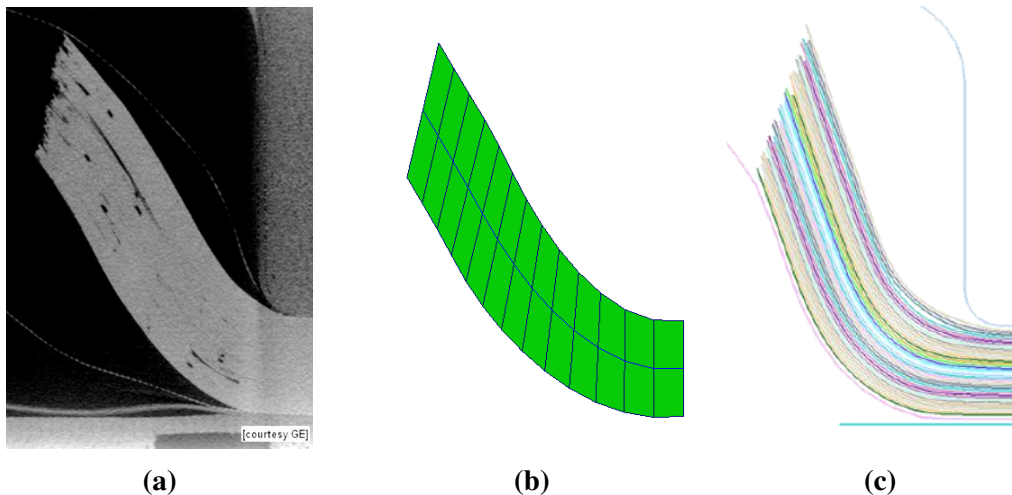


**Figure 3.43** – L-flange bending deformation: (a) Experiment [LEU 16]. (b) Simulation with the specific plane shell element (with midline plotting). (c) Simulation with classical shell element for each ply in PAM-FORM [LEU 16]

### 3.4.5 The emphasis of the Mindlin shell element is unable to simulate the bending deformation of thick fibrous materials

The internal energy of Mindlin shell element is composed by three parts: membrane, bending and shearing (in-plane shearing and transverse shearing). In the commercial software, such as ABAQUS, the bending stiffness of Mindlin shell element comes from the integration in-plane tensile modulus through the thickness direction. However, allowing the bending stiffness of fibrous materials to be calculated from the tensile modulus would result in a numerically high bending stiffness that is not the true property of fibrous materials. Consequently, bending stiffness measured from experiment is very indispensable. However, the application of measured bending stiffness to the Mindlin shell element in ABAQUS is not easy. A constitutive equation defining bending moment and curvature needs to be implemented through the subroutine, like UGENS in ABAQUS/implicit. This may prove to be difficult when utilizing commercial FE software, since the shell section behavior is related to the stress integration through the thickness and therefore related to

### 3. Specific plane shell element for simulating the bending deformation of thick fibrous materials

---

the development of a new finite element algorithm rather than to simply define a constitutive equation [YU 05]. Therefore, a shell element based on the Mindlin shell theory has been developed by us and its bending stiffness is independent of its tensile modulus. In the following simulations, the membrane and bending stiffness of this Mindlin shell element

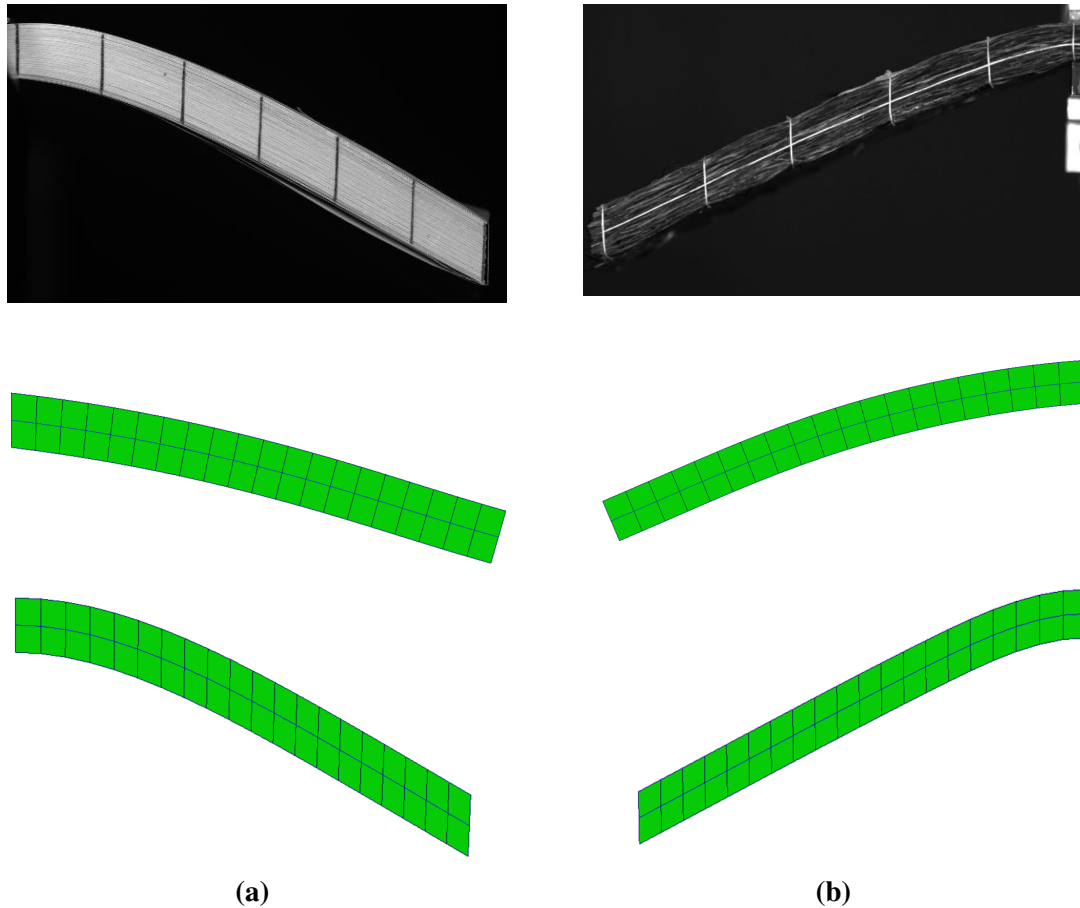


**Figure 3.44** – (a):Book cantilever bending under gravity (Bending length 120 mm). Top: experiment, middle: simulation with Mindlin shell element, bottom: simulation with the specific plane shell element. (b): Laminated reinforcement cantilever bending under gravity (Bending length 118 mm). Top: experiment, middle: simulation with Mindlin shell element, bottom: simulation with the specific plane shell element.

equals the summation of fiber's tensile and bending stiffness in the specific plane shell element (Tab.3.1 and Tab.3.2). Transverse shearing modulus is needed (transverse shearing modulus can't be zero, otherwise it would not be able to simulate the bending deformation). Due to lack of experimental data to characterize the transverse shearing for book and laminated reinforcement, estimated value would be used. For laminated reinforcement, its transverse shearing modulus  $G$  is chosen as 0.01 Mpa, for book its transverse shearing modulus  $G$  is 0.005 Mpa. Figure 3.44 presents the comparison between the experimental test, simulation result with Mindlin shell element and simulation result with

the specific plane shell element. There exists a great difference between experiment and simulation with Mindlin shell element, especially to the rotation of the material director. In the experiment, there is almost no rotation for the material director, for simulation with Mindlin shell element, there exists the rotation, especially for the material directors that are close to the free end. Further-more, from the experiment, we can note there is a thickness extension in the direction of material director, particularly for the part close to the free end, however, simulation using the Mindlin shell element fails to describe this feature. These discrepancies show the Mindlin shell element doesn't allow to correctly describe the bending deformation of thick fibrous materials. On the other hand, a good agreement can be noted in the Figure 3.44 between experiment and simulation with the specific plane shell element. For the part close to clamp end of sample (Figure 3.44), there are almost no rotations for the material directors, but fiber's curvature is not zero.

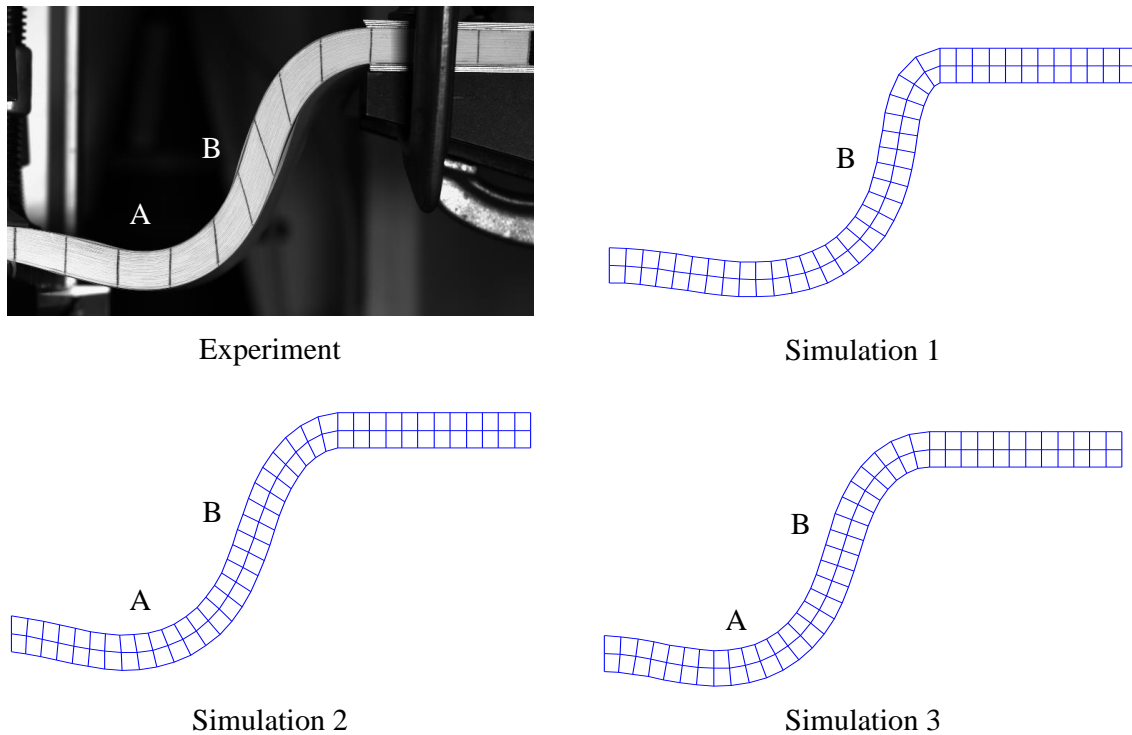


**Figure 3.45** – Comparison of bending deformation shape between simulation with the Mindlin shell element S4R provided by ABAQUS and experiment

Some simulations using the shell element S4R provided by ABAQUS have also been done to simulate the book bending test 3 (Figure 3.20 or Figure 3.45). Shell element S4R is a typical Mindlin shell element, its bending stiffness is coupled with its tensile modulus in ABAQUS. We would try to adjust the tensile modulus and transverse shearing modulus to see whether the simulation can approach to the experimental result. For simulation 1, both the tensile modulus  $E$  and the transverse shearing modulus  $G$  are 10 Mpa; for simulation 2, the tensile modulus  $E$  increases to 100 Mpa, while the transverse shearing modulus  $G$  keeps the same as simulation 1; for simulation 3, both the tensile modulus  $E$

### 3. Specific plane shell element for simulating the bending deformation of thick fibrous materials

---

and the transverse shearing modulus  $G$  are 100 Mpa. Figure 3.45 shows the deformation shapes from experiments and simulations. The comparison of their midlines is shown in Figure 3.46. It's very evident to see the midline of simulation 1 is a little far from the experiment, the midlines of simulation 2 and simulation 3 are close to the experiment. However, if we have a close look at the rotations of the material directors, there are the discrepancies. For the experiment in the region A, there is almost no rotation for the material director, but for simulation 2 and 3 in region A, there exists rotations for the material directors. Besides, in the region B for the experiment, the material director is not perpendicular to the midline, there exists remarkable transverse shearing and a stretching in the material director direction, but for simulation 1, 2 and 3 in region B, the material director almost remains perpendicular to the midline and there is no stretching along the direction of material director.

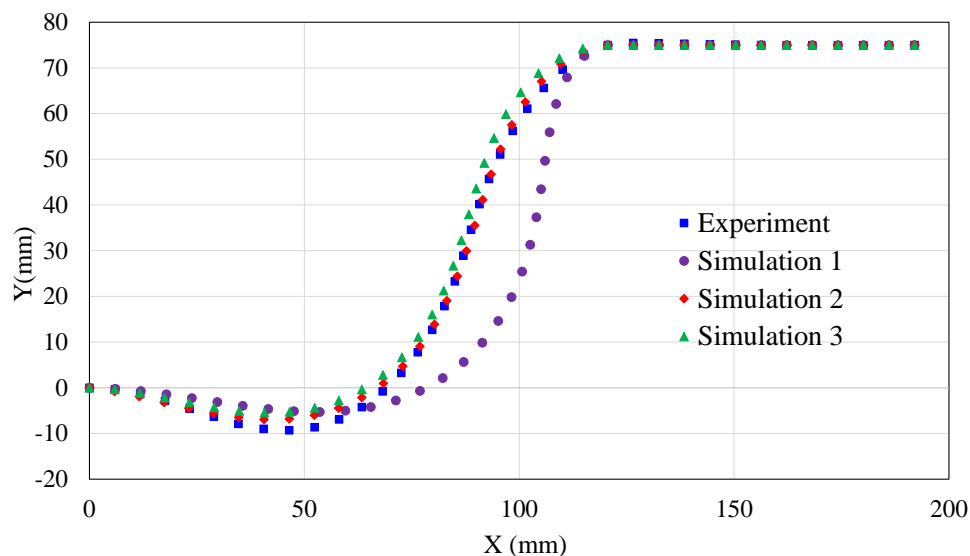


**Figure 3.46** – Comparison of the midline between experiment and simulation with the Mindlin shell element S4R provided by ABAQUS.

These simulation and experimental results further indicate that for the shell structure of fibrous materials, its curvature is not directly related to the first derivative of the rotation angle of material director as that for the shell structure of conventional continuous materials, the curvature calculation used in the Mindlin shell theory can't be directly applied to the shell structure of fibrous materials. This point also implies the Mindlin shell element can't correctly simulate the bending deformation of thick fibrous materials.

## 3.5 Conclusions of chapter 3

A specific plane shell element made of continuous fiber segments was proposed to simulate the bending deformation of thick fibrous materials. The tensile and bending deforma-

tions of fibers were taken into account in the element. Several numerical bending simulation tests were performed with this specific plane shell element and were compared with the experimental results. There is a very good agreement, demonstrating this element can describe the bending deformation of thick fibrous materials. Simulations with the Mindlin shell element were also performed to simulate the bending deformation of thick fibrous materials. It shows there is a large discrepancy compared with the experimental results, particularly to the rotation of the material director. This proves the shell element based on the Mindlin shell theory is unable to correctly simulate the bending deformation of thick fibrous materials. The results obtained in the present study are a very important step for the characterization of bending behaviour of thick fibrous materials, even now it can be only be used to simulate the plane bending deformation. In the next step, this plane shell element would be expanded to spatial shell element and used to the forming simulations of whole component part.

### 3. Specific plane shell element for simulating the bending deformation of thick fibrous materials

---

## Conclusions and perspectives

Bending stiffness of thermoplastic prepregs is temperature dependent and is not directly related to its in-plane tensile modulus as the conventional continuous materials at the elevated temperature. In most thermo-forming simulations, bending stiffness is neglected due to lack of experimental method to measure its value. The consequence is these forming simulations can't accurately predict the final deformation shape, particularly the appearance and shape of wrinkles. A bending stiffness test method was proposed to measure the bending stiffness of thermoplastic prepregs in this thesis. It was operated in an environmental chamber. The homogeneity of temperature within the specimen was tested by a set of thermocouples. The bending deflection shape was acquired by a CCD camera and image processing was used to extract its midline. The midline was fitted by the uniform quartic B-spline curve that gave the curvature. The bending moment versus curvature curves were obtained for PEEK-carbon satin prepreg, PPS-carbon satin prepreg and PA66-Glass satin prepreg within a set of temperatures including the manufacturing temperatures. The bending deflection increases strongly with temperature until a limit is reached in which the resin is completely melted and the bending stiffness entirely comes from the reinforcement. The moment-curvature curve is non-linear. The measured bending stiffness was used in the thermoforming simulations. Taking into account the bending stiffness of the prepreg at the manufacturing temperature is important. Notably it determines the size and shape of wrinkles. Although wrinkle size and shape depend on the material's bending stiffness, but the sensitivity of wrinkle size and shape to the bending stiffness is weak.

Fiber is the most basic constituent of fibrous materials. Due to the existence of relative sliding between fibers, the bending deformation kinematics of thick fibrous materials would be affected and show some specialties compared with the conventional continuous materials. These facts lead to the elements based on the 3D constitutive model or the general shell theory can't correctly simulate the bending deformation of thick fibrous materials. Based on the above issues, a specific plane shell element was developed. This specific plane shell element was made of continuous fiber segments. Both the bending and tensile stiffnesses of fiber were taken into account. Several numerical bending simulation tests have been performed with this specific plane shell element and have been compared with experimental results. There is good agreement, demonstrating this element can accurately predict the bending deformation of thick fibrous materials. Simulations with the Mindlin shell element also been performed to simulate the bending deformation of thick fibrous materials. It shows there is a large discrepancy compared with the experimental

results, particularly the rotation of material director. This demonstrates the Mindlin shell element is unable to correctly simulate the bending deformation of thick fibrous materials. The results obtained in the present study are a very important step for the characterization of bending behaviour of thick fibrous materials, although currently it can only be used to simulate the plane bending, it proposes a new possible way to simulate bending deformation for thick fibrous materials.

## Perspectives

From the major conclusions obtained in this thesis, additional investigations can be performed in the future works. A summary of these is presented below:

- In the present study, only some simple image processing techniques have been used to process the bending deflection shape, in the future, some more sophisticated image processing methods can be applied.
- In the current work, the influence of deformation rate on the bending stiffness of thermoplastic composites is neglected. In the future, the influence of deformation rate on the bending stiffness should be studied.
- Bending behaviour of thermoplastic composites is time dependent, in the future the relaxation behaviour of bending stiffness can be investigated.
- Friction influence on the bending stiffness is implicitly and simply considered in the present study, in the future, more detailed work should be done to investigate how fiber to fiber friction and fiber sliding in fibrous structure affect the bending behaviour.
- The relation between bending recovery and imposed curvature is very important, in the future, it's very interesting to have some studies on this aspect.
- In the present study, the element that is developed to simulate the bending behaviour of thick fibrous materials is a plane shell element. Consequently, it can only be used to simulate the plane bending deformation. In the future, this element should be expanded into spatial shell element to simulate more complex bending deformation.

# Appendices



# Appendix A

## A.1 The calculation of system stiffness matrix for the uniform quartic B-spline curve

Calculation of matrix  $\mathbf{K}_1$ ,  $\mathbf{K}_2$  and  $\mathbf{K}_3$  can be simplified into evaluating integrals of sub-matrices for each curve segment and assembling them together as that done in the finite element stiffness assembly [FAN 95]. These integrals of sub-matrices for each segment are called element stiffness matrices and can be calculated as:

$$\mathbf{K}_1^e = \int_0^1 \dot{\mathbf{N}}^e (\dot{\mathbf{N}}^e)^T du \quad (\text{A.1})$$

$$\mathbf{K}_2^e = \int_0^1 \ddot{\mathbf{N}}^e (\ddot{\mathbf{N}}^e)^T du \quad (\text{A.2})$$

$$\mathbf{K}_3^e = \int_0^1 \dddot{\mathbf{N}}^e (\dddot{\mathbf{N}}^e)^T du \quad (\text{A.3})$$

$\dot{\mathbf{N}}^e$ ,  $\ddot{\mathbf{N}}^e$  and  $\dddot{\mathbf{N}}^e$  denote the first, second and third derivative of  $\mathbf{N}^e$ :

$$\mathbf{N}^e = [ M_{0,4}(u) \quad M_{1,4}(u) \quad M_{2,4}(u) \quad M_{3,4}(u) \quad M_{4,4}(u) ] \quad (\text{A.4})$$

$$\dot{\mathbf{N}}^e = \left[ \frac{dM_{0,4}(u)}{du} \quad \frac{dM_{1,4}(u)}{du} \quad \frac{dM_{2,4}(u)}{du} \quad \frac{dM_{3,4}(u)}{du} \quad \frac{dM_{4,4}(u)}{du} \right] \quad (\text{A.5})$$

$$\ddot{\mathbf{N}}^e = \left[ \frac{d^2M_{0,4}(u)}{du^2} \quad \frac{d^2M_{1,4}(u)}{du^2} \quad \frac{d^2M_{2,4}(u)}{du^2} \quad \frac{d^2M_{3,4}(u)}{du^2} \quad \frac{d^2M_{4,4}(u)}{du^2} \right] \quad (\text{A.6})$$

$$\dddot{\mathbf{N}}^e = \left[ \frac{d^3M_{0,4}(u)}{du^3} \quad \frac{d^3M_{1,4}(u)}{du^3} \quad \frac{d^3M_{2,4}(u)}{du^3} \quad \frac{d^3M_{3,4}(u)}{du^3} \quad \frac{d^3M_{4,4}(u)}{du^3} \right] \quad (\text{A.7})$$

Where  $M_{k,4}$  are basis functions of quartic B-spline ( $k=0,1,2,3,4$ ).

## A.2 Incremental relative angle calculation

Since the incremental displacement is very small, it's assumed the influence of the axial extension on the rotation of geometry straight segments is neglected. The motion of the two geometry straight segments can be decomposed into two steps. The first step is the rigid translation and rigid rotation, which makes the initial configuration  $f1 - f2 - f3$  goes to the configuration  $F1 - F2 - C3$ . The second step consists the rotation  $\Delta\varphi_2$ , so that endpoint  $C3$  is coincident with fiber endpoint  $F3$ . When given a small incremental displacement, the incremental rigid rotation angle of geometry straight segment  $f1 - f2$  around fiber endpoint  $f1$  is  $\beta$  (counterclockwise is positive):

$$\beta \approx \frac{\Delta\bar{\mathbf{u}}_2^f \cdot \bar{\mathbf{n}}_1 - \Delta\bar{\mathbf{u}}_1^f \cdot \bar{\mathbf{n}}_1}{l_1} \quad (\text{A.8})$$

Where  $\Delta\bar{\mathbf{u}}_j^f$  is the incremental displacement vector at fiber endpoint  $ff$ ,  $\bar{\mathbf{n}}_1$  and  $\bar{\mathbf{n}}_2$  are the unit normal vectors to the geometry straight segment  $f1 - f2$  and  $f2 - f3$ ,  $l_1$  and  $l_2$  are the length of geometry straight segments  $f1 - f2$  and  $f2 - f3$ .

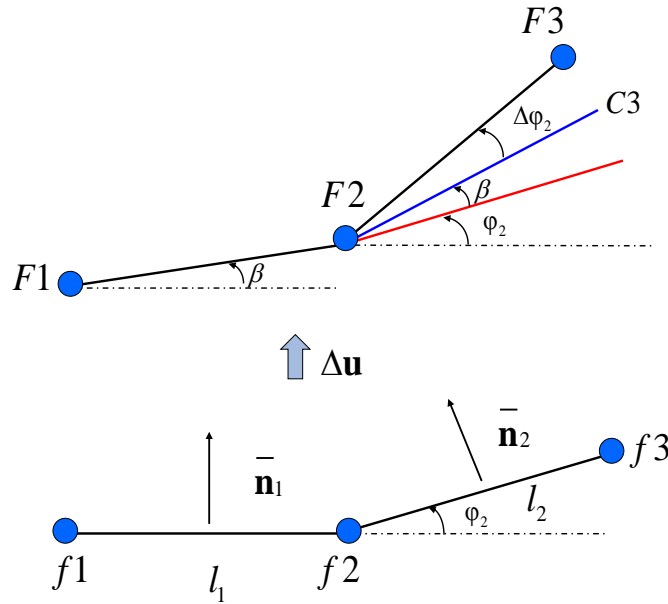


**Figure A.1** – The schematic of the motion of geometry straight segments.

The incremental rigid rotation angle of geometry straight segment  $f2 - f3$  around the fiber endpoint  $f2$  is  $\beta + \Delta\varphi_2$ :

$$\beta + \Delta\varphi_2 \approx \frac{\Delta\bar{\mathbf{u}}_3^f \cdot \bar{\mathbf{n}}_2 - \Delta\bar{\mathbf{u}}_2^f \cdot \bar{\mathbf{n}}_2}{l_2} \quad (\text{A.9})$$

Finally, the incremental relative angle between geometry straight segments  $f1 - f2$  and

$f_2 - f_3$  is  $\Delta\varphi_2$  and can be calculated as:

$$\Delta\varphi_2 = (\beta + \Delta\varphi_2) - \beta = \frac{\Delta\bar{\mathbf{u}}_3^f \cdot \bar{\mathbf{n}}_2 - \Delta\bar{\mathbf{u}}_2^f \cdot \bar{\mathbf{n}}_2}{l_2} - \frac{\Delta\bar{\mathbf{u}}_2^f \cdot \bar{\mathbf{n}}_1 - \Delta\bar{\mathbf{u}}_1^f \cdot \bar{\mathbf{n}}_1}{l_1} \quad (\text{A.10})$$

A.

---

# Bibliography

- [ABB 51] ABBOTT N.  
The measurement of stiffness in textile fabrics. *Textile Research Journal*, vol. 21, n° 6, 1951, p. 435–441, Sage Publications.
- [AHM 70] AHMAD S., IRONS B. M., ZIENKIEWICZ O.  
Analysis of thick and thin shell structures by curved finite elements. *International Journal for Numerical Methods in Engineering*, vol. 2, n° 3, 1970, p. 419–451, Wiley Online Library.
- [AIM 08] AIMENE Y., HAGEGE B., SIDOROFF F., VIDAL-SALLÉ E., BOISSE P., DRIDI S.  
Hyperelastic approach for composite reinforcement forming simulations. *International Journal of Material Forming*, vol. 1, n° 1, 2008, p. 811–814, Springer.
- [BAD 07a] BADAWI S. S.  
Development of the weaving machine and 3D woven spacer fabric structures for lightweight composites materials. PhD thesis, Technischen Universität Dresden , Germany, 2007.
- [BAD 07b] BADEL P., VIDAL-SALLÉ E., BOISSE P.  
Computational determination of in-plane shear mechanical behaviour of textile composite reinforcements. *Computational materials science*, vol. 40, n° 4, 2007, p. 439–448, Elsevier.
- [BAD 08] BADEL P., VIDAL-SALLE E., MAIRE E., BOISSE P.  
Simulation and tomography analysis of textile composite reinforcement deformation at the mesoscopic scale. *Composites Science and Technology*, vol. 68, n° 12, 2008, p. 2433-2440.
- [BAL 13] BALASUBRAMANIAN M.  
*Composite Materials and Processing*. CRC press, 2013.
- [BAT 81] BATHE K.-J., HO L.-W.  
A simple and effective element for analysis of general shell structures. *Computers & Structures*, vol. 13, n° 5-6, 1981, p. 673–681, Elsevier.

- [BAT 85] BATHE K.-J., DVORKIN E. N.  
A four-node plate bending element based on Mindlin/Reissner plate theory and a mixed interpolation. *International Journal for Numerical Methods in Engineering*, vol. 21, n° 2, 1985, p. 367–383, Wiley Online Library.
- [BAT 86] BATHE K.-J., DVORKIN E. N.  
A formulation of general shell elements: the use of mixed interpolation of tensorial components. *International Journal for Numerical Methods in Engineering*, vol. 22, n° 3, 1986, p. 697–722, Wiley Online Library.
- [BAT 08] BATTINI J.-M.  
A rotation-free corotational plane beam element for non-linear analyses. *International Journal for numerical methods in engineering*, vol. 75, n° 6, 2008, p. 672–689, Wiley Online Library.
- [BEL 13] BELYTSCHKO T., LIU W. K., MORAN B., ELKHODARY K.  
*Nonlinear finite elements for continua and structures*. John Wiley & Sons, 2013.
- [BER 01] BERNET N., MICHAUD V., BOURBAN P.-E., MÅNSON J.-A.  
Commingled yarn composites for rapid processing of complex shapes. *Composites Part A: Applied Science and Manufacturing*, vol. 32, n° 11, 2001, p. 1613–1626, Elsevier.
- [BIS 04] BISCHOFF M., BLETZINGER K.-U., WALL W., RAMM E.  
Models and Finite Elements for Thin-Walled Structures. *Encyclopedia of computational mechanics*, , 2004, Wiley Online Library.
- [BOE 13] BOEING  
. « Resource: 787 Aircraft Rescue & Firefighting Composite Structure », 2013.
- [BOI 92] BOISSE P., DANIEL J., GELIN J.  
A simple isoparametric three-node shell finite element. *Computers & structures*, vol. 44, n° 6, 1992, p. 1263–1273, Elsevier.
- [BOI 95] BOISSE P., CHEROUAT A., GELIN J., SABHI H.  
Experimental study and finite element simulation of a glass fiber fabric shaping process. *Polymer composites*, vol. 16, n° 1, 1995, p. 83–95, Wiley Online Library.
- [BOI 04] BOISSE P.  
*Mise en forme des renforts fibreux de composites*. Ed. Techniques Ingénieur, 2004.
- [BOI 11] BOISSE P., HAMILA N., VIDAL-SALLÉ E., DUMONT F.  
Simulation of wrinkling during textile composite reinforcement forming. Influence of tensile, in-plane shear and bending stiffnesses. *Composites Science and Technology*, vol. 71, n° 5, 2011, p. 683–692, Elsevier.

- 
- [BOL 79] BOLOURCHI S.  
On finite element nonlinear analysis of general shell structures. PhD thesis, Massachusetts Institute of Technology, 1979.
- [BOR 99] BORGEFORS G., NYSTROM I., SANNITI DI BAJA G.  
Computing skeletons in three dimensions. *Pattern Recognition*, vol. 32(7), 1999, p. 1225–1236.
- [BUE 01] BUET-GAUTIER K., BOISSE P.  
Experimental analysis and modeling of biaxial mechanical behavior of woven composite reinforcements. *Experimental mechanics*, vol. 41, n° 3, 2001, p. 260–269, Springer.
- [BUL 00] BULUSU A., CHEN J.  
Modeling the Unit Cell Geometry of Twill Weave Fabrics during Shear Deformation. *PROCEEDINGS-AMERICAN SOCIETY FOR COMPOSITES*, 2000, p. 66–75.
- [CAM 03] CAMPBELL JR F. C.  
*Manufacturing processes for advanced composites*. Elsevier, 2003.
- [CEL 91] CELNIKER G., GOSSARD D.  
Deformable curve and surface finite-elements for free-form shape design. *ACM SIGGRAPH computer graphics*, vol. 25 ACM, 1991, p. 257–266.
- [CHA 12] CHARMETANT A., ORLIAC J.-G., VIDAL-SALLÉ E., BOISSE P.  
Hyperelastic model for large deformation analyses of 3D interlock composite preforms. *Composites Science and Technology*, vol. 72, n° 12, 2012, p. 1352–1360, Elsevier.
- [CON 88] CONGRESS U.  
Advanced Materials by Design (OTA-E-351). *Washington, DC: Office of Technology Assessment*, , 1988.
- [COR 09] CORNELISSEN B., AKKERMAN R.  
Analysis of yarn bending behaviour. , 2009, The British Composites Society.
- [CRE 06] CREECH G., PICKETT A.  
Meso-modelling of non-crimp fabric composites for coupled drape and failure analysis. *Journal of materials science*, vol. 41, n° 20, 2006, p. 6725–6736, Springer.
- [DAH 76] DAHL P. R.  
Solid friction damping of mechanical vibrations. *AIAA Journal*, vol. 14, n° 12, 1976, p. 1675–1682.
- [DEB 10] DEBILBAO E., SOULAT D., HIVET G., GASSER A.  
Experimental study of bending behaviour of reinforcements. *Experimental Mechanics*, vol. 50, 2010, p. 333-351.
-

- [DEL 09] DE LUYCKER E., MORESTIN F., BOISSE P., MARSAL D.  
Simulation of 3D interlock composite preforming. *Composite Structures*, vol. 88, n° 4, 2009, p. 615–623, Elsevier.
- [DOU 06] DOUTHE C., BAVEREL O., CARON J.-F.  
Form-finding of a grid shell in composite materials. *Journal-International association for shell and Spatial Structures*, vol. 150, 2006, Page 53.
- [DUM 03] DUMONT F. et al.  
Contribution à l'expérimentation et à la modélisation du comportement mécanique de renforts de composites tissés. PhD thesis, Paris 6, 2003.
- [DUR 10] DURVILLE D.  
Simulation of the mechanical behaviour of woven fabrics at the scale of fibers. *International journal of material forming*, vol. 3, n° 2, 2010, p. 1241–1251, Springer.
- [FAN 95] FANG L., GOSSARD D. C.  
Multidimensional curve fitting to unorganized data points by nonlinear minimization. *Computer-Aided Design*, vol. 27, n° 1, 1995, p. 48–58, Elsevier.
- [FAR 89] FARIN G., SAPIDIS N.  
Curvature and the fairness of curves and surfaces. *IEEE Computer Graphics and Applications*, vol. 9, n° 2, 1989, p. 52–57, IEEE.
- [FET 13] FETFATSIDIS K. A., JAUFFRÈS D., SHERWOOD J. A., CHEN J.  
Characterization of the tool/fabric and fabric/fabric friction for woven-fabric composites during the thermostamping process. *International journal of material forming*, vol. 6, n° 2, 2013, p. 209–221, Springer.
- [FLO 13] FLORIMOND C.  
Contribution à la modélisation mécanique du comportement de mèches de renforts tissés à l'aide d'un schéma éléments finis implicite. PhD thesis, INSA de Lyon, 2013.
- [GAO 15] GAO S., LIANG B., VIDAL-SALLE E.  
Development of a new 3D beam element with section changes: The first step for large scale textile modelling. *Finite Elements in Analysis and Design*, vol. 104, 2015, p. 80–88, Elsevier.
- [GAS 00] GASSER A., BOISSE P., HANKLAR S.  
Mechanical behaviour of dry fabric reinforcements. 3D simulations versus biaxial tests. *Computational materials science*, vol. 17, n° 1, 2000, p. 7–20, Elsevier.
- [GRI 96] GRIESSER M., TAYLOR P.  
The bending behaviour of fabrics: An energy approach. *Mathematics and Computers in Simulation*, vol. 41, n° 5, 1996, p. 579–586, Elsevier.

- [GRI 05] GRIFFITHS B.  
Boeing sets pace for composite usage in large civil aircraft. *High Performance Composites*, vol. 5, n° 1, 2005.
- [GRO 66] GROSBERG P.  
The mechanical properties of woven fabrics part ii: the bending of woven fabrics. *Textile Research Journal*, vol. 36, n° 3, 1966, p. 205–211, Sage Publications.
- [GRO 80] GROSBERG P., HEARLE J., THWAITES J., AMIRBAYAT J.  
Mechanics of flexible fiber assemblies. *NATO ASI Series, The Netherlands*, , 1980, Page 197.
- [GUO 02] GUO Y., GATI W., NACEUR H., BATOZ J.  
An efficient DKT rotation free shell element for springback simulation in sheet metal forming. *Computers & structures*, vol. 80, n° 27, 2002, p. 2299–2312, Elsevier.
- [GUZ 15] GUZMAN-MALDONADO E., HAMILA N., BOISSE P., BIKARD J.  
Thermomechanical analysis, modelling and simulation of the forming of pre-impregnated thermoplastics composites. *Composites Part A: Applied Science and Manufacturing*, vol. 78, 2015, p. 211–222, Elsevier.
- [HAA 14a] HAANAPPEL S., AKKERMAN R.  
Shear characterisation of uni-directional fibre reinforced thermoplastic melts by means of torsion. *Composites Part A: Applied Science and Manufacturing*, vol. 56, 2014, p. 8–26, Elsevier.
- [HAA 14b] HAANAPPEL S., TEN THIJE R., SACHS U., RIETMAN B., AKKERMAN R.  
Formability analyses of uni-directional and textile reinforced thermoplastics. *Composites Part A: Applied Science and Manufacturing*, vol. 56, 2014, p. 80–92, Elsevier.
- [HAM 07] HAMILA N.  
Simulation de la mise en forme des renforts composites mono et multi plis. PhD thesis, Villeurbanne, INSA, 2007.
- [HAM 08] HAMILA N., BOISSE P.  
Simulations of textile composite reinforcement draping using a new semi-discrete three node finite element. *Composites Part B: Engineering*, vol. 39, n° 6, 2008, p. 999–1010.
- [HAM 09] HAMILA N., BOISSE P., SABOURIN F., BRUNET M.  
A semi-discrete shell finite element for textile composite reinforcement forming simulation. *International journal for numerical methods in engineering*, vol. 79, n° 12, 2009, p. 1443–1466, Wiley Online Library.
- [HAR 04] HARRISON P., CLIFFORD M., LONG A.  
Shear characterisation of viscous woven textile composites: a comparison between

- picture frame and bias extension experiments. *Composites Science and Technology*, vol. 64, n° 10, 2004, p. 1453–1465, Elsevier.
- [HAR 05] HARRISON P., CLIFFORD M.  
*Design and manufacture of textile composites, chapter Rheological Behaviour of Pre-impregnated Textile Composites*. Woodhead Publishing, Cambridge, UK, 2005.
- [HIG 90] ON HIGH MODULUS FIBERS A. C. D.-., COMPOSITES T.  
*ASTM Standards and Literature References for Composite Materials*. ASTM International, 1990.
- [HIV 05] HIVET G., BOISSE P.  
Consistent 3D geometrical model of fabric elementary cell. Application to a meshing preprocessor for 3D finite element analysis. *Finite Elements in Analysis and Design*, vol. 42, n° 1, 2005, p. 25–49, Elsevier.
- [HOL 00] HOLZAPFEL G. A.  
*Nonlinear Solid Mechanics*. Wiley, 2000.
- [HTT 14] [HTTP://WWW.CUSTOMPARTNET.COM](http://www.custompartnet.com)  
. « The introduction of thermal stamping process », 2014.
- [HUS 06] HUSSAIN F., HOJJATI M., OKAMOTO M., GORGA R. E.  
Review article: polymer-matrix nanocomposites, processing, manufacturing, and application: an overview. *Journal of composite materials*, vol. 40, n° 17, 2006, p. 1511–1575, Sage Publications.
- [KAN 13] KANT M., PENUMADU D.  
Fracture behavior of individual carbon fibers in tension using nano-fabricated notches. *Composites Science and Technology*, vol. 89, 2013, p. 83-88.
- [KAW 73] KAWABATTA S., MASAKO N., KAWAI H.  
The finite deformation theory of plain weave fabrics, Part I, Part II, Part III. *Z of the Textile Institute*, vol. 64, 1973, p. 21–83.
- [KAW 80] KAWABATA S.  
*The Standardization and Analysis of Hand Evaluation*. Textile Machinery Society of Japan, 1980.
- [LEU 16] LEUTZ D., VERMILYEA M., BEL S., HINTERHÖLZL R.  
Forming Simulation of Thick AFP Laminates and Comparison with Live CT Imaging. *Applied Composite Materials*, , 2016, p. 1–18, Springer.
- [LIA 14] LIANG B., HAMILA N., PEILLON M., BOISSE P.  
Analysis of thermoplastic prepreg bending stiffness during manufacturing and of its influence on wrinkling simulations. *Composites Part A: Applied Science and Manufacturing*, vol. 67, 2014, p. 111–122, Elsevier.

- [LIA 15] LIANG B., HAMILA N., BOISSE P.  
The bending behaviour characterisation of thermoplastic prepregs and its influence on the wrinkling. *Key Engineering Materials*, , 2015.
- [LOM 00] LOMOV S. V., GUSAKOV A., HUYSMANS G., PRODROMOU A., VERPOEST I.  
Textile geometry preprocessor for meso-mechanical models of woven composites. *Composites Science and Technology*, vol. 60, n° 11, 2000, p. 2083–2095, Elsevier.
- [LOM 07] LOMOV S. V., IVANOV D. S., VERPOEST I., ZAKO M., KURASHIKI T., NAKAI H., HIROSAWA S.  
Meso-FE modelling of textile composites: Road map, data flow and algorithms. *Composites Science and Technology*, vol. 67, n° 9, 2007, p. 1870–1891, Elsevier.
- [LOM 08] LOMOV S. V., IVANOV D. S., VERPOEST I., ZAKO M., KURASHIKI T., NAKAI H., MOLIMARD J., VAUTRIN A.  
Full-field strain measurements for validation of meso-FE analysis of textile composites. *Composites Part A: Applied Science and Manufacturing*, vol. 39, n° 8, 2008, p. 1218–1231, Elsevier.
- [LON 14] LONG A. C.  
*Composites forming technologies*. Elsevier, 2014.
- [LUY 09] LUYCKER E.  
Simulation et expérimentation en mise en forme de renforts composites 3D interlocks. PhD thesis, INSA de Lyon, 2009.
- [MAD 15] MADEO A., FERRETTI M., DELL ISOLA F., BOISSE P.  
Thick fibrous composite reinforcements behave as special second-gradient materials: three-point bending of 3D interlocks. *Zeitschrift für angewandte Mathematik und Physik*, vol. 66, n° 4, 2015, p. 2041–2060, Springer.
- [MAR 15] MARGOSSIAN A., BEL S., HINTERHOELZL R.  
Bending characterisation of a molten unidirectional carbon fibre reinforced thermoplastic composite using a Dynamic Mechanical Analysis system. *Composites Part A: Applied Science and Manufacturing*, vol. 77, 2015, p. 154–163, Elsevier.
- [MAT 14] MATHIEU S.  
Modélisation du comportement mécanique lors du procédé de mise en forme et pyrolyse des interlocks CMC. PhD thesis, INSA de Lyon, france, 2014.
- [MAT 15] MATHIEU S., HAMILA N., BOUILLON F., BOISSE P.  
Enhanced modeling of 3D composite preform deformations taking into account local fiber bending stiffness. *Composites Science and Technology*, vol. 117, 2015, p. 322–333, Elsevier.

- [NAO 14] NAOUAR N., VIDAL-SALLÉ E., SCHNEIDER J., MAIRE E., BOISSE P.  
Meso-scale FE analyses of textile composite reinforcement deformation based on X-ray computed tomography. *Composite Structures*, vol. 116, 2014, p. 165–176, Elsevier.
- [NGU 13] NGUYEN Q., VIDAL-SALLÉ E., BOISSE P., PARK C., SAOUAB A., BRÉARD J., HIVET G.  
Mesoscopic scale analyses of textile composite reinforcement compaction. *Composites Part B: Engineering*, vol. 44, n° 1, 2013, p. 231–241, Elsevier.
- [ORL 12] ORLIAC J.-G.  
Analyse et simulation du comportement anisotrope lors de la mise en forme de renforts tissés interlock. PhD thesis, INSA de Lyon, 2012.
- [PAR 96a] PARK H.  
Surface modeling for 3D shape reconstruction from measurement data. PhD thesis, POSTECH, Korea, 1996.
- [PAR 96b] PARK H., KIM K.  
Smooth surface approximation to serial cross-sections. *Computer-Aided Design*, vol. 28, n° 12, 1996, p. 995–1005, Elsevier.
- [PAR 00] PARK H., KIM K., LEE S.-C.  
A method for approximate NURBS curve compatibility based on multiple curve refitting. *Computer-Aided Design*, vol. 32, n° 4, 2000, p. 237–252, Elsevier.
- [PEI 30] PEIRCE F.  
The handle of cloth as a measurable quantity. *The Journal of the Textile Institute*, vol. 21, 1930, p. 377-416.
- [PEN 05] PENG X. Q., CAO J.  
A continuum mechanics-based non-orthogonal constitutive model for woven composite fabrics. *Composites Part A: Applied Science and Manufacturing*, vol. 36, n° 6, 2005, p. 859-874.
- [PEN 13] PENG X., GUO Z., DU T., YU W.-R.  
A simple anisotropic hyperelastic constitutive model for textile fabrics with application to forming simulation. *Composites Part B: Engineering*, vol. 52, 2013, p. 275-281, Elsevier.
- [PIE 96] PIEGL L., TILLER W.  
Algorithm for approximate NURBS skinning. *Computer-Aided Design*, vol. 28, n° 9, 1996, p. 699–706, Elsevier.
- [POP 66] POPPER P. G.  
Mechanics of bending of fiber assemblies. PhD thesis, Massachusetts Institute of Technology, 1966.

- [POR 01] PORA J.  
Composite materials in the airbus A380—from history to future. *Proceedings of ICCM13, Plenary lecture, CD-ROM*, , 2001.
- [ROB 98] ROBITAILLE F., GAUVIN R.  
Compaction of textile reinforcements for composites manufacturing. I: Review of experimental results. *Polymer composites*, vol. 19, n° 2, 1998, p. 198–216, Wiley Online Library.
- [ROG 89] ROGERS D. F., FOG N.  
Constrained B-spline curve and surface fitting. *Computer-Aided Design*, vol. 21, n° 10, 1989, p. 641–648, Elsevier.
- [SAB 06] SABOURIN F., BRUNET M.  
Detailed formulation of the rotation-free triangular element S3 for general purpose shell analysis. *Engineering Computations*, vol. 23, 2006, p. 469-502.
- [SAC 14] SACHS U.  
Friction and bending in thermoplastic composites forming processes. PhD thesis, University of Twente, 2014.
- [SHE 07] SHERBURN M.  
Geometric and mechanical modelling of textiles. PhD thesis, Nottingham university, 2007.
- [SOT 11] SOTEROPOULOS D., FETFATSIDIS K., SHERWOOD J. A., LANGWORTHY J.  
Digital Method of Analyzing the Bending Stiffness of Non-Crimp Fabrics. *THE 14TH INTERNATIONAL ESAFORM CONFERENCE ON MATERIAL FORMING: ESAFORM 2011*, vol. 1353 AIP Publishing, 2011, p. 913-917.
- [STA 04] STANDARD A.  
Standard Test Method for Stiffness of Fabrics. ASTM International, West Conshohocken, PA, 2004.
- [STI 12] STIG F.  
3D Woven Reinforcement in Composites. PhD thesis, KTH, Sweden, 2012.
- [SYE 12] SYERKO E., COMAS-CARDONA S., BINETRUY C.  
Models of mechanical properties/behavior of dry fibrous materials at various scales in bending and tension: a review. *Composites Part A: Applied Science and Manufacturing*, vol. 43, n° 8, 2012, p. 1365–1388, Elsevier.
- [TON 02] TONG L., MOURITZ A. P., BANNISTER M.  
*3D fibre reinforced polymer composites*. Elsevier, 2002.

- [VAN 91] VAN WEST B., PIPES R. B., ADVANI S.  
The consolidation of commingled thermoplastic fabrics. *Polymer Composites*, vol. 12, n° 6, 1991, p. 417–427, Wiley Online Library.
- [VAS 96] VASSILEV T. I.  
Fair interpolation and approximation of B-splines by energy minimization and points insertion. *Computer-Aided Design*, vol. 28, n° 9, 1996, p. 753–760, Elsevier.
- [WAN 08] WANG J.  
Predictive modelling and experimental measurement of composite forming behaviour. PhD thesis, University of Nottingham, 2008.
- [WAN 13] WANG P., HAMILA N., BOISSE P.  
Thermoforming simulation of multilayer composites with continuous fibres and thermoplastic matrix. *Composites Part B: Engineering*, vol. 52, 2013, p. 127–136, Elsevier.
- [WAN 14] WANG P., HAMILA N., PINEAU P., BOISSE P.  
Thermomechanical analysis of thermoplastic composite prepregs using bias-extension test. *Journal of Thermoplastic Composite Materials*, vol. 27, 2014, p. 679–698, SAGE Publications.
- [WIL 99] WILKS C.  
Processing technologies for woven glass/polypropylene composites. PhD thesis, University of Nottingham, UK, 1999.
- [YU 02] YU W. R., POURBOGHRAT F., CHUNG K., ZAMPALONI M., KANG T. J.  
Non-orthogonal constitutive equation for woven fabric reinforced thermoplastic composites. *Composites Part A: Applied Science and Manufacturing*, vol. 33, n° 8, 2002, p. 1095–1105.
- [YU 05] YU W. R., ZAMPALONI M., POURBOGHRAT F., CHUNG K., KANG T. J.  
Analysis of flexible bending behavior of woven preform using non-orthogonal constitutive equation. *Composites Part A: Applied Science and Manufacturing*, vol. 36, n° 6, 2005, p. 839–850, Elsevier.
- [ZIE 05] ZIENKIEWICZ O. C., TAYLOR R. L.  
*The finite element method for solid and structural mechanics*. Butterworth-heinemann, 2005.
- [ZOU 06] ZOUARI B., DANIEL J.-L., BOISSE P.  
A woven reinforcement forming simulation method. Influence of the shear stiffness. *Computers & structures*, vol. 84, n° 5, 2006, p. 351–363, Elsevier.





